UC Berkeley
UC Berkeley Electronic Theses and Dissertations

Title

Modeling Vapor-fed Electrolyzers for CO2 Reduction

Permalink

https://escholarship.org/uc/item/2kd602wp

Author

Weng, Lien-Chun

Publication Date

2020

Peer reviewed|Thesis/dissertation

eScholarship.org Powered by the California Digital Library
University of California

Modeling Vapor-fed Electrolyzers for CO_2 Reduction

By
Lien-Chun Weng

A dissertation submitted in partial satisfaction of the
requirements for the degree of
Doctor of Philosophy
in
Chemical Engineering
in the
Graduate Division
of the
University of California, Berkeley

Committee in charge:

Professor Alexis T. Bell, Co-chair
Dr. Adam Z. Weber, Co-chair
Professor Bryan D. McCloskey
Professor Simo A. Mäkiharju

Spring 2020

Copyright © 2020
Lien-Chun Weng

Abstract

Modeling Vapor-fed Electrolyzers for CO_2 Reduction
by
Lien-Chun Weng
Doctor of Philosophy in Chemical Engineering
University of California, Berkeley
Prof. Alexis T. Bell, Co-chair
Dr. Adam Z. Weber, Co-chair

The electrochemical reduction of CO_2 (CO_2R) to value-added products is an attractive route for tackling the rising atmospheric CO_2 levels and storing intermittent renewable energy. Fundamental understanding of CO_2R has progressed significantly in recent years and is critical in the development of industrial-scale CO_2 electrolyzers. However, most of our understanding has been drawn from experiments optimized for aqueous-phase CO_2R systems. These systems are limited by mass transfer at low current densities (in the order of 10 mA/cm^2) due to unfavorable CO_2 solubility and transport in aqueous media, whereas technoeconomic analysis emphasizes the need to operate CO_2R at current densities above 100 mA/cm^2 for industrial viability.

To achieve commercially-relevant CO_2R rates, gas-diffusion electrodes (GDEs) play a critical role as they can decrease the diffusion length of CO_2 from 100 μm seen in aqueous systems to as small as 10 nm, and increase the local concentration of CO_2. These architectures enable current densities that are almost two orders of magnitude greater than what is achievable with planar electrodes in an aqueous electrolyte at the same applied cathode overpotential. The thin diffusion layer in GDEs allows access to higher CO_2R current densities, as well as environments with higher OH^- concentrations. The addition of porous cathode layers, however, introduces several parameters that require tuning in order to optimize GDE cell performance. Because the structure of GDEs is complex and CO_2R in such systems involves the simultaneous occurrence of many physical processes, it is very hard, if not impossible, to assess the impact of a particular change in the composition and structure of the GDE without a detailed model that accounts for the convoluted chemistry and physics interrelationships. An overview of such model is presented in Chapter 2, and the complex interplays are probed through the model in Chapter 3 and used to shed light on the optimization of GDEs.

With the order-of-magnitude increase in current density obtained by GDEs, conventional cell designs for planar electrodes become severely limited by the ohmic drop across the cell, making membrane-electrode assemblies (MEAs) an attractive alternative. MEAs have smaller cell resistances as they do not have aqueous electrolyte compartments and can greatly reduce the distance between the two electrodes. These MEA designs are investigated through a complete electrochemical cell model in Chapter 4 and Chapter 5; cell design considerations such as the distribution of the applied voltage, water management, and CO_2 utilization efficiencies are explored.

Chapter 4 uses silver-based MEAs (Ag-MEAs) as a model system and studies the performance and limitations of two MEA designs: one with gaseous feeds at both the anode and cathode, and the other with an aqueous anode feed ($KHCO_3$ or KOH exchange solution, or liquid H_2O) and a gaseous cathode feed. Copper-based MEAs (Cu-MEAs) are examined in Chapter 5. Copper has been shown to be the most effective CO_2R catalyst to yield high selectivity towards hydrocarbons and alcohols; Cu-MEAs hold promise for increasing the energy efficiency for electrochemical reduction of CO_2 to C_{2+} products while maintaining high current densities. However, fundamental understanding of Cu-MEAs is still limited compared to the wealth of knowledge available for aqueous electrolyte Cu systems. Sensitivity analysis shows that catalyst layer properties can be optimized to increase the energy efficiencies of C_{2+} products. Issues associated with water management and tradeoffs associated with elevated operating temperatures are also discussed to guide the optimization of Cu-MEAs.

Finally, Chapter 6 summarizes the finding in relation to the field and proposes future directions to progress the development of practical CO_2 electrolyzers. Overall, this dissertation demonstrates how physics-based modeling can assist in the transfer of knowledge from aqueous to vapor-fed systems by deconvoluting the impacts of the multiple physical processes occurring in the device.

Table of Contents

Acknowledgments

First and foremost, I would like to thank my advisors, Dr. Adam Weber and Prof. Alex Bell, for their guidance and mentorship throughout my PhD. Their scientific rigor and intellectual curiosity have been a constant source of inspiration during my graduate studies and will follow me throughout my scientific career.

I feel incredibly privileged to have worked among many excellent researchers in the Energy Conversion Group and at the Joint Center for Artificial Photosynthesis. I would like to thank Andrew Crothers and Prof. Rohini Bala Chandran for their help and encouragement, especially during my initial years in the field of electrochemical modeling. Their diligence and enthusiasm for science have impressed and motivated me since day one. I would also like to acknowledge Dr. Lalit Pant and Dr. Michael Gerhardt for the many helpful discussions on numerous modeling issues; David Larson for his mentorship during my brief excursion into the realm of experimental work; Dr. Marielle Soniat and Dr. Christianna Lininger for their career advice and many insightful discussions; Julie Fornaciari and Oyinkansola Romiluyi for their companionship sharing the same co-advisorship experience.

I am indebted to all my friends who have helped me during various stages of my PhD. Special thanks to Dr. Chang-Ming Jiang, Dr. Meron Tesfaye, and Dr. Li-Hao Yeh for their encouragement and support when I struggled to adapt to PhD life; and to Zephy Leung, Steven Dela Cruz, Samuel Leung, Jeffery Li, Qinlei Liu, Frederick Twigg, and Ruijie Zhong for their unwavering friendship over the last few years.

Lastly, I am forever grateful to my family for providing me the opportunity to be where I am today; and to my partner, David Chen, for his constant support and unconditional love. I could not have done it without them.

Funding Acknowledgements

This material is based upon work performed by the Joint Center for Artificial Photosynthesis, a DOE Energy Innovation Hub, supported through the Office of Science of the U.S. Department of Energy under Award Number DE-SC0004993.

List of Figures

List of Tables

List of Symbols

Roman

a_s	specific surface area, m^{-1}
a_j	activity of species j
c_j	concentration of species j, mol m^{-3}
D_i	diffusivity of species i, m^{2} s^{-1}
F	Faraday’s constant, C mol^{-1}
H_i	Henry’s constant of species i, M atm^{-1}
i	electrolyte current density, mA cm^{-2}
i_o	exchange current density, mA cm^{-2}
i_S	electrode current density, mA cm^{-2}
j_i	diffusive mass flux of species i, g m^{-2} s^{-1}
k_MT	mass transfer coefficient, m s^{-1}
k_n	rate constant for homogeneous reaction n, s^{-1}
K_n	equilibrium constant for homogeneous reaction n
M_i	molar mass of species i, g mol^{-1}
n_i	mass flux of species i, g m^{-2} s^{-1}
n_k	number of electrons transferred in reaction k
N_j	molar flux of species j, mol m^{-2} s^{-1}
p	pressure, atm
Q	volumetric mass source, g m^{-3}
$r_{p,m}$	pore radius in medium m,
R	gas constant, J mol^{-1} K^{-1}
R_i	volumetric molar source terms for species i, mol m^{-3} s^{-1}
$s_{i,k}$	stoichiometric coefficient of species i in reaction k
S_m	saturation of medium m
ΔS_n	change of entropy for reaction n, J mol^{-1} K^{-1}
T	temperature, K

u	mass-averaged fluid velocity, m s^{-1}
U_k^o	reference potential of reaction k, V
$v_{\mathrm{p},i}$	diffusion volume of species i
V_i	molar volume of species i, ml mol^{-1}
x_j	mole fraction of aqueous species j
y_i	mole fraction of gaseous species i
z_i	charge of species i

Greek

$\alpha_{\mathrm{a/c},k}$	anodic/cathodic transfer coefficient of reaction k
α_0	water transport coefficient, mol^2 J^{-1} cm^{-1} s^{-1}
$\gamma_{j,k}$	reaction order with respect to species j for reaction k
$\epsilon_{p,m}$	volume fraction of phase p in medium m
ϵ_m^o	intrinsic porosity of medium m
η_k	surface overpotential for reaction k, V
κ	electrolyte conductivity, S m^{-1}
λ	water content
μ_0	water chemical potential, J mol^{-1}
ξ	electro-osmotic coefficient
ρ	mass density, g cm^{-3}
σ_{S}	electronic conductivity, S m^{-1}
ϕ_{L}	electrolyte potential, V
ϕ_{S}	electronic potential, V
ψ	permeability, m^2
ω_i	mass fraction of species i
$\mathit{\Omega}$	volumetric heat source, W/m^3

Subscripts

a	anodic
c	cathodic
i	gaseous species
j	species in the ionomer
k	charge transfer reaction
m	medium: DM, CL, Mem, Ion,
n	homogeneous reaction
p	phase
A	average
B	bulk homogeneous
CT	charge transfer
G	gas phase
L	liquid phase
M	membrane
MT	mass transfer
PT	phase transfer
S	solid phase
V	water vapor
α	transfer coefficient
0	water

Superscript

eff	effective property
eq	equilibrium
o	standard condition
ref	reference state
SM	Stefan-Maxwell

Chapter 1 Introduction‡

A great deal of interest has arisen in the design and development of energy conversion devices that carry out electrochemical CO_2 reduction (CO_2R). This process uses electrical energy to convert CO_2 to value-added products, offering a potential route to recycle CO_2 and tackle intermittency issues associated with renewable energy sources.[1-4] Most of what is known about CO_2R is based on experiments conducted with planar electrodes immersed in an aqueous electrolyte saturated with CO_2.[5-9] However, the current density of such systems is limited significantly by poor mass-transport to the cathode due to the low diffusivity and solubility of CO_2 in water and the thickness of the mass-transfer boundary layer near the electrode (~60 to 160 µm).[10-12] As a consequence, the mass-transfer limited current density based on the geometric area of the cathode is on the order of 10 mA/cm^2. Additionally, acid/base reactions of CO_2 with hydroxide anions (OH^-) further limits CO_2 availability in alkaline aqueous systems.[13-15]

Gas-Diffusion Electrodes

For the electrochemical reduction of CO_2 to be commercially viable, current densities above 100 mA/cm^2 at relatively low power inputs in needed.[16-18] One of the promising approaches for achieving this target is to use vapor-fed cells with gas-diffusion electrodes (GDEs), where current densities up to 360 mA/cm^2 for CO_2R have been demonstrated.[19-25]

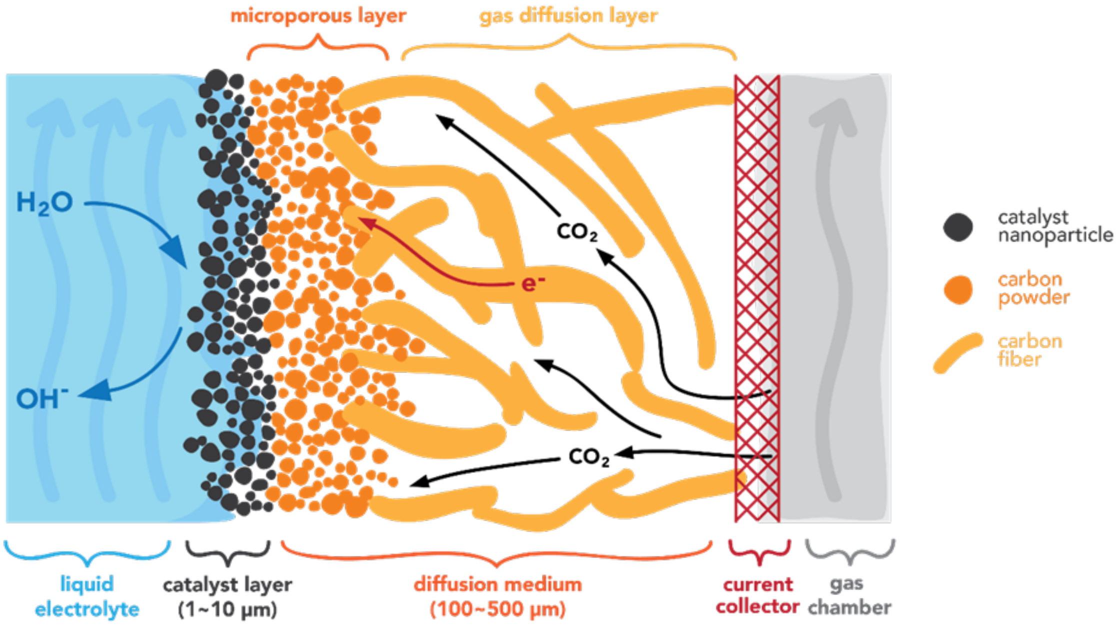

Figure 1.1 Schematic of a gas-diffusion electrode

---

‡ This chapter uses figures originally published in L. C. Weng, A. T. Bell and A. Z. Weber, *Phys. Chem. Chem. Phys.*, 2018, **20**, 16973-16984 and L. C. Weng, A. T. Bell and A. Z. Weber, *Energy Environ. Sci.*, 2019, **12**, 1950-1968

The GDE is comprised of a porous catalyst layer (CL) and a diffusion medium (DM), as shown in **Figure 1.1**. The DM is typically a hydrophobic carbon layer (water contact angle ~93°-112°)[26] that consists of a macroporous gas-diffusion layer (GDL) and a microporous layer (MPL). The DM serves several purposes. First, it provides a porous medium through which reactants/products can diffuse in to/out of the CL; second, it mechanically supports the CL and provides compression resistance upon the cell assembly; and third, it provides electronic conductivity for electrons to flow to/from the current collector and external circuit to the CL. Most commercial DMs are PTFE treated to be hydrophobic; ideally, the DM remains dry throughout its use (no electrolyte leakage or condensation). Catalyst particles mixed with a (ionic) binder are deposited onto the MPL to form the CL. The binder holds the catalyst particles together and may provide ionic conductivity within the CL.

The exact microstructure of the CL is not well known. Cook *et al.* first proposed a schematic illustrating a "triple-phase interface" region where the CO_2R reaction occurs, and many have argued that the high current densities achievable with GDEs is attributable to a high concentration of CO_2 at the gas/catalyst interface, thereby overcoming the low solubility of CO_2 in water.[27] However, the hypothesis that a triple-phase interface is essential for the high performance of a GDE is likely incorrect for two reasons: (1) At NTP (20 ˚C and 1 atm), the gas-phase concentration of CO_2 is 42 mM. This level is only 30% higher than that of dissolved CO_2 (33 mM) and cannot account for the order of magnitude increase in CO_2R current density observed experimentally. (2) The surface area of true triple-phase regions is likely to be too small. (3) Recent experimental and theoretical work have demonstrated the importance of water and hydrated cations on the elementary processes involved in CO_2R.[28, 29] Therefore, we propose that the most active regions are those where the catalyst is in intimate contact with electrolyte. This means that although CO_2 is supplied to the GDE from the gas phase, the reactant at the catalyst site is still dissolved CO_2.

Attempts to optimize GDE performance experimentally have been devoted, for the most part, to Sn electrodes used to produce formic acid. Wu *et al.* found that increasing the CL thickness beyond 9 µm had no effect on the overall activity; however, the reason for this behavior was not given.[30] Both Wu *et al.* and Wang *et al.* demonstrated that changing the CL composition can affect the total current density and faradaic efficiency (FE) of a Sn GDE.[30, 31] Other parameters such as catalyst morphology, fabrication methods, *etc.* have also been studied experimentally and a detailed survey of different GDE systems has been reported by Endrodi *et al.*[32] While there have been numerous experimental designs of GDEs, there have been only a limited number of efforts on the modeling of vapor-fed CO2R systems. The impact of different GDE structures and CL conditions on CO_2R performance is investigated through modeling and discussed further in Chapter 3.

Membrane-Electrode Assemblies (MEAs)

An order-of-magnitude improvement in the CO_2R current density occurs in moving from a planar cathode to a GDE cathode configuration due to the increased active surface area for a given geometric area and decreased mass-transfer resistances associated with the GDE configuration.[25, 33] Simply substituting the planar cathode with a GDE cathode (aqueous GDE cell shown in **Figure 1.2**) results in an order-of-magnitude increase in the ohmic overpotential when the total current density is increased from 10 to 100 mA/cm^2, rendering such cell designs impractical for industrial application.

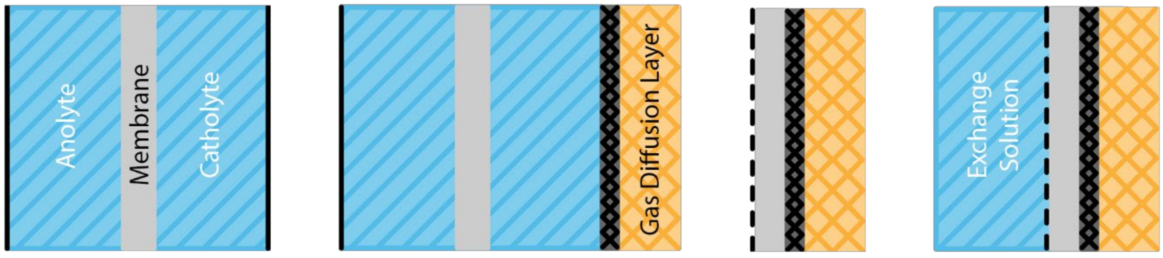

Planar Cell Aqueous GDE Full-MEA Exchange-MEA

Potential distribution	Planar (10 mA/cm^2)	Aqueous GDE (100 mA/cm^2)	Full-MEA & Exchange-MEA (100 mA/cm^2)
Thermodynamic potential under normal conditions (V) (OER + COER)	1.34		
Cathode overpotential (V)	1.1[5]	0.7[33]	0.7[33]
Anode overpotential (V)	0.3*	0.4*	0.4*
Electrolyte ohmic potential (V) (0.5 M $KHCO_3$, 60 mS/cm)	0.2**	2**	0
Membrane ohmic potential (V) (50 µm, 5 mS/cm)	0.01	0.1	0.1
Total cell potential (V)	**2.95**	**4.54**	**2.54**

**assuming OER on IrO_2, approximated from Butler-Volmer equation fitted to experimental data from ref.*[34]
***assuming 1 cm distance between anode and cathode*

Figure 1.2 Graphical illustration for various cell designs and a breakdown of the applied voltage. There is a 44% reduction in applied voltage for MEA compared to the aqueous GDE cell at the same total current density.

By comparison, both the full-MEA and exchange-MEA eliminate the large ohmic drop by removing the aqueous electrolyte compartments and significantly decreasing the anode-cathode distance, allowing the cell to maintain the 100 mA/cm^2 current density with a 44% reduction in the applied cell voltage. The values in **Figure 1.2** are first-order approximations and do not include effects such as concentration polarization, temperature changes, membrane dehydration, *etc.* A mesh-like structure or GDE is required for the anode in the full-MEA and exchange-MEA designs where OER occurs to prevent layer delamination caused by the evolution of oxygen bubbles and ensure good electrical contact with the current collector.

While the full-MEA and exchange-MEA minimize the ohmic loss across the cell, reactant and product crossover becomes a concern due to the small distance between the two electrodes. For a Ag cathode, since almost no liquid product is produced and CO solubility is low, CO crossover current density is limited to approximately 1 mA/cm^2 at room temperature (estimated using Fick's law and the solubility and diffusivity of CO in water). It should be noted though that the aqueous GDE cells can serve diagnostic purposes due to their isolation of a single electrode and easier implementations of a reference electrode.[35]

There have been numerous reports demonstrating the feasibility of MEA-like cells attaining CO_2R current densities upwards of 100 mA/cm^2, an order of magnitude higher than can be achieved using typical aqueous architectures.[23, 24, 27, 36-40] Various configurations and materials have been presented, with much debate as to which design is the most effective for scale-up and commercialization, as reviewed[35] and discussed[25] recently. Cook *et al.* first illustrated the electrochemical reduction of CO_2 to hydrocarbons in an MEA design, showing an approximately 0.5 V reduction in the cell potential at 10 mA/cm^2 when removing the anolyte compartment.[41] Hori *et al.* found that an anion-exchange membrane (AEM) is more suitable for CO_2R than a cation-exchange membrane (CEM), as the CEM not only prevents transport of HCO_3^- and $CO_3^=$ anions, but also allows high proton concentrations that promote the competing hydrogen evolution reaction (HER).[42] In agreement with Hori *et al.*, Delacourt *et al.* noted the importance of minimizing proton concentration near the cathode to suppress HER. They did not observe CO_2R products over Ag using a CEM but obtained an 80% CO_2R faradaic efficiency (FE) after adding a $KHCO_3$ buffer layer between the cathode and CEM. They measured a FE of only 3 % for CO_2R with an AEM but did not fully explain why the efficiency was so low.[43] It is notable that Salvatore *et al.* also explored adding a buffer layer between the cathode and membrane to improve the CO_2R current efficiency for an MEA-like cell (aqueous anode feed and gaseous cathode feed, with no anolyte or catholyte compartments). These authors found that the buffer layer provided better hydration, since adding a water layer in place of the buffer layer also achieved a higher CO_2R FE than could be reached in the absence of such a layer.[44] While it is tempting to draw general conclusions from the above studies, it is important to note that each one was performed using cell designs that differed from each other. Hori *et al.* retained the aqueous anolyte compartment but removed the aqueous catholyte compartment;[42] Narayanan, Li, and Salvatore removed the aqueous electrolyte compartments and used an aqueous feed instead;[44-46] and Delacourt, Kriescher, and Wang utilized pure gaseous feeds with no aqueous electrolyte.[43, 47, 48] Without a quantitative understanding of the limitations of each design, it is difficult to compare the results reported in different studies and to draw general conclusions from them.

Recent work has also demonstrated promising progress towards achieving high activity and stability for both CO_2R and CO reduction (COR) using Cu-MEAs. Ripatti *et al.* reported a current density greater than 100 mA/cm^2 at 2.4 V maintained for over 24 h, with a 24% EE for COR to ethylene and acetate.[49] Sullivan *et al.* achieved up to 70% FE towards C_{2+} products from CO reduction.[50] For CO_2R, Garbardo *et al.* demonstrated stable operation for 100 h at over 100 mA/cm^2 with 40% C_2H_4 FE and 23% EE towards C_{2+} products.[51] While these numbers are encouraging, a large design space for Cu-MEAs remains to be explored. Optimization of the various design and operating parameters, such as cell geometry, operating temperature *etc.*, can be guided by physics-based simulation. To date, there has been limited effort on the modeling of vapor-fed CO_2R systems, even more so for MEAs performing CO_2R in the absence of aqueous electrolyte compartments.

Multiphysics modeling is ideal for studying the nonlinear interactions endemic to CO_2 electrolyzers, as witnessed by its applicability in similar energy-conversion devices.[52-58] Delacourt *et al*. presented a model for a vapor-fed cell with an aqueous buffer layer between the cathode and the membrane.[59] They assumed that dissolved CO_2 is in equilibrium with bicarbonate and carbonate ions and these are the main reactants, assumptions that have later been shown not to be valid in regions near the catalyst.[13] They concluded that a fully solid-state MEA could enhance performance of a CO_2 electrolyzer, but did not go into details to describe MEA operation and limitations. They also considered the CL as an interface rather than a domain of finite thickness. More recently, Wu *et al*. developed a comprehensive model for a microfluidic flow cell with GDEs.[60] While they considered a finite thickness for the CL, they neglected bicarbonate acid/base reactions occurring within this region and focused on the overall cell performance rather than the influence of the composition and structure of the CL and how these factors govern the overall cell performance. Gabardo *et al*. calculated the distribution of voltage losses in their experimental device with a multiphysics model,[51] and Sullivan *et al*. presented a water transport model to analyze the level of hydration in their experimental Cu-MEA setup.[50] Both studies included portions of relevant physics – the first focused on electrochemistry, the second, on water management – but a comprehensive model that includes the effects of electrode kinetics, mass and energy transport is still lacking. Furthermore, neither of the previous studies investigated the impact of changes in cell properties or operating conditions on cell performance expressed in terms of product distribution and voltage utilization.

Dissertation Outline

The overall objective of this dissertation is to develop a comprehensive model for vapor-fed CO_2 electrolyzers that incorporates the critical physical phenomena, including electrochemistry, reaction kinetics, multiphase flow, and heat transfer. The model is used to reveal intrinsic tradeoffs and limitations of these devices, and establish design and operating criteria. Chapter 2 presents the modeling approach and governing equations commonly used to tackle complex multiphysics problems for vapor-fed electrochemical energy devices. Model assumptions and determination of key parameter values are discussed. Chapter 3 focuses on the GDE component, detailing the differences in the local environment between aqueous and vapor systems, and how these differences affect CO_2 reduction performance. Analysis of the electrochemical cell is presented in Chapter 4 and Chapter 5. Chapter 4 uses a Ag cathode producing only H_2 and CO as the model system and focuses on describing the operation of MEAs and observed limitations. The effects of multiple CO_2R products on GDEs are investigated in Chapter 5, which analyzes how changes in the cell architecture can affect cell performance and product distribution using a Cu cathode. Water management issues and tradeoffs associated with elevated temperature operations are also discussed in Chapter 5. Finally, Chapter 6 presents a summary and future directions for CO_2 electrolyzers.

Chapter 2 Modeling Methodology

This chapter presents a modeling framework which describes the mass transport, electrochemical and chemical reaction kinetics, and heat transfer physics occurring in CO_2 reduction electrolyzers. The governing equations presented here are used to obtain results discussed in Chapter 3 to Chapter 5; slight modifications and specific boundary conditions for the configuration studied in each chapter are detailed in the *Model Description* section.

Governing Equations

Electrochemical reactions

Oxygen evolution reaction (OER) is catalyzed by IrO_2 at the anode under both acidic and alkaline conditions:

$$2\mathrm{H_2O} \rightarrow \mathrm{O_2} + 4\mathrm{H^+} + 4\mathrm{e^-} \qquad U^o = 1.23\ \mathrm{V} \qquad (2\text{-}1)$$

$$4\mathrm{OH^-} \rightarrow \mathrm{O_2} + 2\mathrm{H_2O} + 4\mathrm{e^-} \qquad U^o = 1.23\ \mathrm{V} \qquad (2\text{-}2)$$

HER and CO_2R reactions occur at the cathode. The product of CO_2R depends on the catalyst of choice. The following cathodic reactions are considered for a Cu catalyst,

$$2\mathrm{H_2O} + 2\mathrm{e^-} \rightarrow \mathrm{H_2} + 2\mathrm{OH^-} \qquad U^o = 0\ \mathrm{V} \qquad (2\text{-}3)$$

$$\mathrm{CO_2} + \mathrm{H_2O} + 2\mathrm{e^-} \rightarrow \mathrm{CO} + 2\mathrm{OH^-} \qquad U^o = -0.11\ \mathrm{V} \qquad (2\text{-}4)$$

$$\mathrm{CO_2} + \mathrm{H_2O} + 2\mathrm{e^-} \rightarrow \mathrm{HCOO^-} + 2\mathrm{OH^-} \qquad U^o = -0.02\ \mathrm{V} \qquad (2\text{-}5)$$

$$\mathrm{CO_2} + 6\mathrm{H_2O} + 8\mathrm{e^-} \rightarrow \mathrm{CH_4} + 2\mathrm{OH^-} \qquad U^o = 0.17\ \mathrm{V} \qquad (2\text{-}6)$$

$$2\mathrm{CO_2} + 8\mathrm{H_2O} + 12\mathrm{e^-} \rightarrow \mathrm{C_2H_4} + 12\mathrm{OH^-} \qquad U^o = 0.07\ \mathrm{V} \qquad (2\text{-}7)$$

$$2\mathrm{CO_2} + 9\mathrm{H_2O} + 12\mathrm{e^-} \rightarrow \mathrm{C_2H_5OH} + 12\mathrm{OH^-} \qquad U^o = 0.08\ \mathrm{V} \qquad (2\text{-}8)$$

$$3\mathrm{CO_2} + 13\mathrm{H_2O} + 18\mathrm{e^-} \rightarrow \mathrm{C_3H_7OH} + 18\mathrm{OH^-} \qquad U^o = 0.09\ \mathrm{V} \qquad (2\text{-}9)$$

The partial current density for product k is described by the Tafel equation,[61]

$$i_k = i_{o,k} \prod_j \left(\frac{c_j}{c_j^{\mathrm{ref}}}\right)^{\gamma_{j,k}} \cdot \exp\left(-\frac{\alpha_{\mathrm{c},k} F}{RT}\eta_k\right) \qquad (2\text{-}10)$$

where R is the gas constant, F is the Faraday's constant, and η_k is the overpotential, defined as the deviation of the electrode potential (the difference between the electric potential, ϕ_{S}, and the electrolyte potential, ϕ_{L}) from the equilibrium potential after Nernstian correction,

$$\eta_k = (\phi_{\mathrm{S}} - \phi_{\mathrm{L}}) - \left(U_k^o - \frac{2.303RT}{F}\, p\mathrm{H}\right) \qquad (2\text{-}11)$$

The kinetic parameters were extracted from experimental measurements after correcting for concentration polarization effects with an 80-µm boundary layer model (discussed further in

Appendix A Boundary Layer Model).[13] The exchange current density, $i_{o,k}$, anodic/cathodic transfer coefficient, $\alpha_{a/c,k}$, activity dependence, $\prod_j a_j^{\gamma_{j,k}}$, and standard electrode potential, U_k^o, are summarized in **Table 2.1**. The activity of water, a_w, is defined in Equation (2-22), and the activity of all other species is defined as $a_{j\neq\mathrm{w}} = \frac{c_j}{c^\mathrm{ref}}$, referenced to $c^\mathrm{ref} = 1\ \mathrm{M}$.

Table 2.1 Rate parameters for charge transfer reactions

	U_k^o (V)	$i_{o,k}$ (mA cm^{-2})	$\alpha_{\mathrm{a/c},k}$	$\prod_j a_j^{\gamma_{j,k}}$	**Ref.**
OER on IrO$_2$					62-65
O_2 (acid)	1.23	1.2 x 10^{-8} $\exp\left(-\frac{0.01[\mathrm{eV}]\mathrm{pH}}{k_BT}\right)$	1.5	$a_\mathrm{w}^{1.6}$	
O_2 (base)		1.6 x 10^{-6} $\exp\left(-\frac{0.01[\mathrm{eV}]\mathrm{pH}}{k_BT}\right)$		a_{OH^-}	
HER & CO$_2$R on roughened Cu					66, 67
H_2	0	1.0 x 10^{-2} $\exp\left(-\frac{0.01[\mathrm{eV}]\mathrm{pH}}{k_BT}\right)$	0.28	a_w^2	
CO	-0.11	2.6	0.17	$a_\mathrm{w}\left(\frac{[\mathrm{CO_2}]}{1\ \mathrm{M}}\right)^{1.50}$	
HCOO□	-0.02	2.2 x 10^{-1}	0.37	$a_\mathrm{w}\left(\frac{[\mathrm{CO_2}]}{1\ \mathrm{M}}\right)^{2.00}$	
C_2H_4	0.07	1.9 x 10^{-6}	0.67	$a_\mathrm{w}^3\left(\frac{[\mathrm{CO_2}]}{1\ \mathrm{M}}\right)^{1.36}$	
C_2H_5OH	0.08	1.2 x 10^{-8}	0.74	$a_\mathrm{w}^3\left(\frac{[\mathrm{CO_2}]}{1\ \mathrm{M}}\right)^{0.96}$	
C_3H_7OH	0.09	4.9 x 10^{-9}	0.75	$a_\mathrm{w}^4\left(\frac{[\mathrm{CO_2}]}{1\ \mathrm{M}}\right)^{0.96}$	

The solid-phase electric potential, ϕ_S, is determined by solving charge conservation,

$$\boldsymbol{\nabla}\cdot\mathbf{i}_\mathrm{S} = -\sum_k a_{\mathrm{s},k} i_k \tag{2-12}$$

and Ohm's law,

$$\mathbf{i}_\mathrm{S} = -\sigma_\mathrm{S}^\mathrm{eff}\boldsymbol{\nabla}\phi_\mathrm{S} \tag{2-13}$$

where $\mathbf{i}_\mathrm{S}$ is the current density in the solid phase, $\sigma_\mathrm{S}^\mathrm{eff}$ is the effective electronic conductivity, and $a_{s,k}$ is the specific active surface area (surface area per unit volume) for reaction k. For reactions with gas-phase reactants, such as CO$_2$R, accumulation of liquid water in the CL can block access to active sites. This is accounted for by including a correction to the intrinsic active surface area, a_S^o, as follows,

$$a_{\mathrm{s},k} = (1 - S_{\mathrm{CL}})a_{\mathrm{s}}^{o} \tag{2-14}$$

where S_{CL} is the saturation level of the CL, describing the fraction of pores in the GDE filled with liquid water. S_{CL} is determined from the capillary pressure, defined as $p_{\mathrm{C}} = p_{\mathrm{L}} - p_{\mathrm{G}}$, and its relationship shown in **Figure B.1a**.

Gas and liquid water transport in the DM and CL

The gas and liquid flow in the porous media (DM and CL) are calculated via mass conservation,

$$\nabla \cdot \rho_p \mathbf{u}_p = Q_p \tag{2-15}$$

and Darcy's law,

$$\mathbf{u}_p = -\frac{\psi_{m,p}^{\mathrm{eff}}}{\mu_p} \nabla p_p \tag{2-16}$$

where $\mathbf{u}_p$ is the mass-averaged velocity field of phase p; ψ_m^{eff} is the effective permeability of medium m; ρ and μ is the fluid density and viscosity; Q is the volumetric mass source term, discussed in a later section.

The gas phase contains CO_2, H_2O, H_2, CO, CH_4, C_2H_4, O_2, and N_2; the mole fractions are calculated from mole balance,

$$\nabla \cdot \mathbf{N}_i = R_{\mathrm{B},i} + R_{\mathrm{CT},i} + R_{\mathrm{PT},i} \tag{2-17}$$

where $R_{\mathrm{B},i}$, $R_{\mathrm{CT},i}$, and $R_{\mathrm{PT},i}$, describe the molar source terms of species i due to charge transfer reactions, bulk homogeneous reactions, and phase-transfer reactions, respectively. The molar flux, $\mathbf{N}_i$, is determined from the mass flux,

$$\mathbf{N}_i = \frac{1}{M_i}\left(-\rho_{\mathrm{G}} D_i^{\mathrm{eff}} \nabla \omega_i - \rho_{\mathrm{G}} D_i^{\mathrm{eff}} \omega_i \frac{\nabla M_{\mathrm{A}}}{M_{\mathrm{A}}} + \rho_i \mathbf{u}_{\mathrm{G}}\right) \tag{2-18}$$

where ρ_{G} is the gaseous mixture density; ω_i, M_i, D_i^{eff}, is the mass fraction, molecular weight, and effective diffusion coefficient of species i, respectively; $M_{\mathrm{A}} = \left(\sum_i \frac{\omega_i}{M_i}\right)^{-1}$ is the average molecular weight of the mixture. Additionally,

$$\sum_i x_i = 1 \tag{2-19}$$

where the mole fraction $x_i = \frac{\omega_i M_{\mathrm{A}}}{M_i}$.

Species transport in the ionomer

Concentrations profiles for five charged species (OH^-, HCO_3^-, $CO_3^=$, H^+, $HCOO^-$) and three neutral species (H_2O, CO_2, HCOOH) in the membrane and the ionomer are determined by simulation. Gaseous species N_2, O_2, H_2, CO, CH_4, C_2H_4 are neglected due to their low solubilities in the ionomer.[68-70] C_2H_5OH (EtOH) and C_3H_7OH (PrOH) can leave the system in both liquid and vapor phases; products in liquid phase can be collected in the cathode outlet, or transport across the membrane and collected in the anode outlet.[51] Although the presence of these alcohols can affect ionomer properties,[71-73] there is limited data on their interactions with AEMs. Consequently, we do not account for these effects in this study. For simplicity, we assume that EtOH and PrOH leave the system rapidly and, therefore, we do not include their transport in the model. Finally, formic acid is included in the model as it participates in the acid-base reaction with $HCOO^-$, but it is also assumed to transport out of the system rapidly.

The molar flux of water, $\mathbf{N}_\mathrm{w}$, occurs via diffusion and electro-osmosis,

$$\mathbf{N}_\mathrm{w} = -\alpha_\mathrm{w}^\mathrm{eff,M} \boldsymbol{\nabla}\mu_\mathrm{w} + \sum_j \xi_j^\mathrm{eff,M} \mathbf{N}_j \tag{2-20}$$

where $\alpha_\mathrm{w}^\mathrm{eff,M}$ is the effective water transport coefficient and $\xi_j^\mathrm{eff,M}$ is the effective electro-osmotic coefficient (EOC) of species j. However, there is a paucity of measured data for $\xi_j^\mathrm{eff,M}$ for the various ionic species present in the system;[74] therefore, we use an overall EOC, $\xi_\mathrm{A}^\mathrm{eff,M}$, determined as

$$\sum_j \xi_j^\mathrm{eff,M} \mathbf{N}_j = -\xi_\mathrm{A}^\mathrm{eff,M} \frac{\mathbf{i}_\mathrm{L}}{F} \tag{2-21}$$

Since anions carry the net charge in an AEM, the electro-osmotic flux is in opposite direction to the current density in the membrane/ionomer phase by convention, $\mathbf{i}$, hence the negative sign.

The chemical potential of water, μ_w, is defined as

$$\mu_0 = RT \ln a_0 + \overline{V_{0,\mathrm{L}}}\left(p_\mathrm{L,M} - p^\mathrm{ref}\right) \tag{2-22}$$

where $a_\mathrm{w} = p_\mathrm{V}/p_\mathrm{w}^\mathrm{vap}$ is the activity of water vapor referenced to its vapor pressure, $\overline{V_\mathrm{w,L}}$ is the molar volume of liquid water, $p_\mathrm{L,M}$ is the pressure of liquid water in the membrane, and p^ref is a reference pressure of 1 atm.

The molar flux of all other species, $\mathbf{N}_{j\neq\mathrm{w}}$, is described by the Nernst-Planck equation,

$$\mathbf{N}_{j\neq\mathrm{w}} = -D_j^\mathrm{eff}\, \boldsymbol{\nabla} c_j + \frac{z_j F}{RT} D_j^\mathrm{eff} c_j \boldsymbol{\nabla}\phi_\mathrm{L} \tag{2-23}$$

where D_j^eff, c_j, z_j are the effective diffusivity, concentration, and charge of species j, respectively. The second term describes the migration flux of charged species, and does not apply to CO_2. Additionally, electroneutrality is needed to solve for the electrolyte ionic potential,

$$\sum_j z_j c_j = 0 \tag{2-24}$$

It should be noted that the Nernst-Planck equation assumes dilute-solution theory and our system is not necessarily dilute under all conditions. However, there is insufficient data available to completely describe all the frictional interactions that would need to be accounted for in our model. Recently, Crothers *et al.* have introduced a novel method based on thermodynamic[75] and transport[76] theories to predict these frictional forces in a CEM environment. However, these methodologies have not been generalized for AEMs and rely on certain data that has yet to be obtained; hence, it remains an active area of research and is not incorporated in this model.

Buffer reactions and phase-transfer reactions

The source terms in conservation equations (2-15) and (2-17) arise from buffer reactions and phase-transfer reactions. The volumetric molar source term due to homogeneous reactions, $R_{\mathrm{B},j}$, occurs in the ionomer and the membrane, and accounts for the following reactions:

$$\mathrm{CO_2(aq) + H_2O} \xleftrightarrow{k_1,k_{-1}} \mathrm{H^+ + HCO_3^-} \qquad K_1 \qquad (2\text{-}25)$$

$$\mathrm{HCO_3^-} \xleftrightarrow{k_2,k_{-2}} \mathrm{H^+ + CO_3^{2-}} \qquad K_2 \qquad (2\text{-}26)$$

$$\mathrm{CO_2(aq) + OH^-} \xleftrightarrow{k_3,k_{-3}} \mathrm{HCO_3^-} \qquad K_3 \qquad (2\text{-}27)$$

$$\mathrm{HCO_3^- + OH^-} \xleftrightarrow{k_4,k_{-4}} \mathrm{H_2O + CO_3^{2-}} \qquad K_4 \qquad (2\text{-}28)$$

$$\mathrm{H_2O} \xleftrightarrow{k_w,k_{-w}} \mathrm{H^+ + OH^-} \qquad K_w \qquad (2\text{-}29)$$

$$\mathrm{HCOOH} \xleftrightarrow{k_5,k_{-5}} \mathrm{H^+ + HCOO^-} \qquad K_5 \qquad (2\text{-}30)$$

where k_n and k_{-n} are the rate coefficients for the forward and reverse directions of homogeneous reaction n and K_n is the equilibrium constant. $R_{\mathrm{B},j}$ can then be calculated as follows,

$$R_{\mathrm{B},j} = \sum_n s_{j,n} c^{\mathrm{ref}} \left(k_n \prod_{s_{j,n}<0} a_j^{-s_{j,n}} - \frac{k_n}{K_n} \prod_{s_{j,n}>0} a_j^{s_{j,n}} \right) \qquad (2\text{-}31)$$

where $s_{j,n}$ is the stoichiometric coefficient (negative for reactants and positive for products) for species j in reaction n.

The source terms due to charge transfer reactions, $R_{\mathrm{CT},j}$, occur only in the CL domains, and is a function of the partial current densities for reactions (2-1)-(2-9),

$$R_{\mathrm{CT},j} = -\sum_k \frac{s_{j,k} a_{\mathrm{s},k} i_k}{n_k F} \qquad (2\text{-}32)$$

where n_k is the number of electrons transferred in reaction k, i_k and $a_{\mathrm{s},k}$ is described in Equations (2-10) and (2-14), respectively.

$R_{\mathrm{PT},j}$ describes the rate of mass transfer of species CO_2, HCOOH, and H_2O between gas|ionomer, liquid|ionomer, and gas|liquid phases. For CO_2 and HCOOH, $R_{\mathrm{PT},j}$ occurs only in the CL, and describes the rate of mass transfer from the gas/liquid phases to the ionomer

$$R_{\mathrm{PT},j} = a_{\mathrm{s}}^{o} k_{\mathrm{MT},j}\left(c_j^{\mathrm{eq}} - c_j\right) \tag{2-33}$$

where $k_{\mathrm{MT},j}$ is the mass transfer coefficient, c_j^{eq} is the concentration of species j in equilibrium with its concentration external to the ionomer. For CO_2, $c_{\mathrm{CO_2}}^{\mathrm{eq}} = p_{\mathrm{G}} y_{\mathrm{CO_2}} H_{\mathrm{CO_2}}$, the product of the gas phase pressure, the mole fraction of CO_2 in the gas phase, and its Henry's constant; for HCOOH, we assume $c_{\mathrm{HCOOH}}^{\mathrm{eq}} = 0$. For H_2O in the ionomer,

$$R_{\mathrm{PT,w,I}} = a_{\mathrm{s}} k_{\mathrm{MT,V}}\left(\frac{RH}{100} - a_{\mathrm{w}}\right) + \frac{a_{\mathrm{s}} k_{\mathrm{MT,L}}}{RT}\left(p_{\mathrm{L}} - p_{\mathrm{L,M}}\right) \tag{2-34}$$

which includes phase transfer of both vapor H_2O and liquid H_2O to the ionomer. Here, $k_{\mathrm{MT,V}}$ and $k_{\mathrm{MT,L}}$ are the mass transfer coefficients for vapor water set to 0.06 mol/m^2·s, and liquid water set to 1 m/s, respectivly.[77, 78] RH is the relative humidity of the gas phase, defined as $RH = \frac{p_{\mathrm{G}} y_0}{p_0^{\mathrm{sat}}} \times 100\%$. For H_2O in the gas phase,

$$\begin{aligned} R_{\mathrm{PT,w,G}} = {} & -a_{\mathrm{s}} k_{\mathrm{MT,V}}\left(\frac{RH}{100} - a_{\mathrm{w}}\right) \\ & - k'_{MT}(RH - 100\%)\left[\mathrm{H}_0\left(\frac{p_{\mathrm{L}}}{p^{\mathrm{ref}}}\right) + \mathrm{H}_0(RH - 100\%)\right] \end{aligned} \tag{2-35}$$

where the first term describes mass transfer between vapor water and the ionomer in the CL, and the second term describes water evaporation/condensation in both the CL and the DM. An arbitrarily large mass transfer coefficient, k'_{MT} = 10^7 mol/m^3·s, and a Heaviside step function, $\mathrm{H}_0(x)$, ensure that $RH = 100\%$ when liquid water is present ($p_L > 0$), and that RH does not exceed 100%. Similarly, for H_2O in the liquid phase,

$$\begin{aligned} R_{\mathrm{PT,w,L}} = {} & -a_{\mathrm{s}} \frac{k_{\mathrm{MT,L}}}{RT}\left(p_{\mathrm{L}} - p_{\mathrm{L,M}}\right) \\ & + k'_{MT}(RH - 100\%)\left[\mathrm{H}_0\left(\frac{p_{\mathrm{L}}}{p^{\mathrm{ref}}}\right) + \mathrm{H}_0(RH - 100\%)\right] \end{aligned} \tag{2-36}$$

where the first term describes mass transfer between liquid water and the ionomer in the CL, and the second term describes water evaporation/condensation.

Finally, the volumetric mass source term, Q, in the overall mass balance Equation (2-15) need to be treated separately for gas and liquid phases. Q_{G} includes the phase transfer of gaseous CO_2 and H_2O to the ionomer, as well as gaseous species produced from the charge transfer reactions, O_2, H_2, CO, CH_4, C_2H_4,

$$Q_{\mathrm{G}} = -M_{\mathrm{CO_2}} R_{\mathrm{PT,CO_2,I}} + M_{\mathrm{w}} R_{\mathrm{PT,w,G}} + \sum_{i \neq \mathrm{CO_2, H_2O, N_2}} M_i R_{\mathrm{CT},i} \tag{2-37}$$

Since only H_2O is modeled in the liquid phase, Q_{L} only includes one term,

$$Q_{\mathrm{L}} = M_0 R_{\mathrm{PT},0,\mathrm{L}} \tag{2-38}$$

Heat transfer

The temperature profile is obtained from solving the energy conservation equation,

$$\boldsymbol{\nabla} \cdot \left(-k_{\mathrm{T},m} \boldsymbol{\nabla} \mathbf{T}\right) = \Omega_{\mathrm{CT}} + \Omega_{\mathrm{B}} + \Omega_{\mathrm{J}} \tag{2-39}$$

where $k_{\mathrm{T},m}$ is the heat transfer coefficient of medium m; Ω_{CT}, Ω_{B}, Ω_{J} are the heat generation terms from charge transfer reactions, bulk buffer reactions, and joule heating, respectively.

Heat generation from charge transfer reactions include both irreversible and reversible terms,

$$\Omega_{\mathrm{CT}} = \sum_k \left(i_k \eta_k + i_k \Pi_k\right) \tag{2-40}$$

where Π_k is the Peltier coefficient for reaction k, listed in **Table A.1**. Heat generation from buffer reactions accounts for the enthalpy change of homogeneous reaction n, ΔH_n,

$$\Omega_{\mathrm{B}} = \sum_n \Delta H_n \left(k_n \prod_{s_{j,n}<0} c_j^{-s_{j,n}} - \frac{k_n}{K_n} \prod_{s_{j,n}>0} c_j^{s_{j,n}} \right) \tag{2-41}$$

and the heat of vaporization for water, ΔH_{vap}, is accounted for in Ω_{PT},

$$\Omega_{\mathrm{PT}} = -k'_{MT}(100\% - RH)\left[\mathrm{H}_0\left(\frac{p_{\mathrm{L}}}{p^{\mathrm{ref}}}\right) + \mathrm{H}_0(RH - 100\%)\right] \Delta H_{\mathrm{vap}} \tag{2-42}$$

Joule heating occurs due to both electronic and ionic resistivity

$$\Omega_{\mathrm{J}} = \frac{i_{\mathrm{S}}^2}{\sigma_{\mathrm{S},m}^{\mathrm{eff}}} + \frac{i_{\mathrm{L}}^2}{\kappa^{\mathrm{eff}}} \tag{2-43}$$

Model Parameters and Effective Properties

Intrinsic parameter values of the membrane/ionomer and GDE properties are summarized in **Table B.1** and **Table B.2**. The diffusion coefficient of gaseous species i is a parallel addition of the mass-averaged Stefan-Maxwell diffusivity,

$$D_i^{\mathrm{SM}} = \frac{1 - \omega_i}{\sum_{q \neq i} \frac{y_q}{D_{iq}}} \tag{2-44}$$

and the Knudsen diffusivity,

$$D_i^{\mathrm{K}} = \frac{2r_{\mathrm{pore},m}}{3}\sqrt{\frac{8RT}{\pi M_i}} \tag{2-45}$$

as,

$$D_i = \left(\frac{1}{D_i^{\mathrm{SM}}} + \frac{1}{D_i^{\mathrm{K}}}\right)^{-1} \tag{2-46}$$

The binary gas-phase diffusion coefficients are estimated following derivation by Fuller *et al.*,

$$D_{iq}[\mathrm{cm}^2\ \mathrm{s}^{-1}] = \frac{10^{-3}T[\mathrm{K}]^{1.75}\left(M_i[\mathrm{g\ mol}^{-1}]^{-1} + M_q[\mathrm{g\ mol}^{-1}]^{-1}\right)^{0.5}}{p_{\mathrm{G}}[\mathrm{atm}]\left(v_{\mathrm{p},i}^{0.33} + v_{\mathrm{p},q}^{0.33}\right)^2} \tag{2-47}$$

where $v_{\mathrm{p},i}$ is the diffusion volume of species i,[79] and $r_{\mathrm{pore},m}$ is the average pore radius of medium m. The diffusion coefficient of neutral species are taken from their values in water';[80] the diffusion coefficient of ionic species in the membrane are back-calculated from the membrane conductivity using Nernst-Einstein,

$$D_j = -\frac{\kappa_j^{\mathrm{eff,M}}RT}{z_i F^2} \tag{2-48}$$

The conductivity values in **Table B.1** are measured for the HCO_3-form AEM; we assume the same conductivity value for the CO_3-form and the HCOO-form AEM, a 10x smaller value for the H-form, and a 5x higher value for the OH-form AEMs.[11, 78, 81] The effective properties of the membrane/ionomer depend on the fraction of membrane pores equilibrated with liquid water, S_{M},

$$X^{\mathrm{eff,M}} = S_{\mathrm{M}}X_{\mathrm{L}} + (1 - S_{\mathrm{M}})X_{\mathrm{V}} \tag{2-49}$$

where X_{L} is the liquid-equilibrated value and X_{V} is the vapor-equilibrated value listed in **Table B.1**. S_{M} is determined from $p_{\mathrm{L,M}}$ as derived by Weber *et al.*; the relationship between S_{M} and $p_{\mathrm{L,M}}$ is shown in **Figure B.1b**.[82]

Finally, all properties in the CL and DM domains need to be further corrected for tortuosity and porosity using Bruggeman's correlation,

$$X_m^{\mathrm{eff}} = \epsilon_{p,m}^{3/2}X_m \tag{2-50}$$

where $\epsilon_{p,m}$ is the volume fraction of the phase of interest, p, in medium m. For example, diffusivity values of ionic species in the CL would be corrected with the volume fraction of ionomer in the CL, $\epsilon_{\mathrm{I,CL}}$, whereas diffusivity values of gaseous species in the CL need to be corrected with $\epsilon_{\mathrm{G,CL}}$. The volume fractions, $\epsilon_{p,m}$, are calculated from the intrinsic porosity of medium m, ϵ_m^o, the ionomer volume fraction in the pore space, $f_{\mathrm{I},m}$, and the saturation level of medium m, S_m, as

$$\epsilon_{\mathrm{S},m} = 1 - \epsilon_m^o \tag{2-51}$$

$$\epsilon_{\mathrm{I},m} = \epsilon_m^o f_{\mathrm{I},m} \tag{2-52}$$

$$\epsilon_{\mathrm{L},m} = \epsilon_m^o \left(1 - f_{\mathrm{I},m}\right) S_m \tag{2-53}$$

$$\epsilon_{\mathrm{G},m} = \epsilon_m^o \left(1 - f_{\mathrm{I},m}\right)(1 - S_m) \tag{2-54}$$

Numerical Solver

The above governing equations are implemented in a 1D model in COMSOL Multiphysics and solved for the MUMPS solver with a relative tolerance of 0.001. The modelling domain has a maximum element size of 0.1 µm, with element sizes decreased to 10^{-3} µm near each domain boundary to capture sharp concentration gradients.

Chapter 3 Understanding Gas-Diffusion Electrodes for CO_2 Reduction‡

Introduction

As discussed in Chapter 1, CO_2 reduction conducted in electrochemical cells with planar electrodes immersed in an aqueous electrolyte is severely limited by mass transport across the hydrodynamic boundary layer. This limitation can be minimized by use of vapor-fed, gas-diffusion electrodes (GDEs), enabling current densities that are almost two orders of magnitude greater at the same applied cathode overpotential than what is achievable with planar electrodes in an aqueous electrolyte.[19-24]

The performance of a GDE greatly depends on the local environment within the CL and the balance between transport phenomena and reaction kinetics. Based on the capillary pressure and CL pore-size distribution and wettability, the pores can be either flooded (**Figure 3.1a**) or dry (**Figure 3.1c**). The partially wetted CL case depicted in **Figure 3.1b** occurs when there is a mixture of flooded and dry pores. Flooded pores completely eliminate gas channels within the CL, resulting in high mass-transport resistances for gaseous reactants (similar to that in aqueous systems). Dry pores will be inactive due to the lack of water from the aqueous electrolyte and an ionic pathway. The film of electrolyte in the wetted pores needs to be thin to minimize CO_2 transport resistance to the catalyst, but thick enough to maintain good ionic conductivity within the CL. The fraction of flooded pores is defined as the saturation, S , and is a function of the capillary-pressure, which is the difference between the liquid- and gas-phase pressures.[83] At low capillary pressures, only small hydrophilic pores will be flooded. As the capillary pressure increases, other pores become flooded in the following order: large hydrophilic pores, large

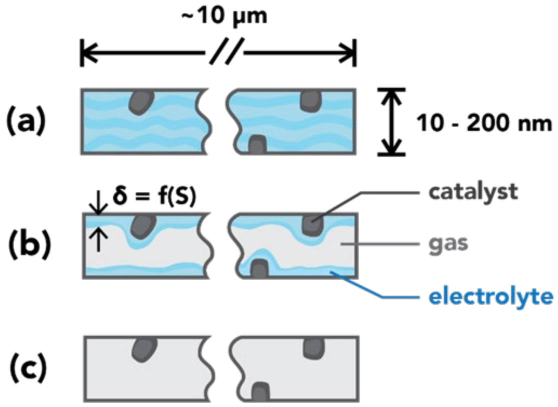

Figure 3.1 Schematic of pore conditions in the catalyst layer. (a) Flooded pore: pore volume filled with electrolyte. (b) Wetted pore: a thin layer of electrolyte covers the pore walls. (c) Dry pore: catalyst inactive due to lack of an ionic pathway.

---

‡ This chapter was adapted from L. C. Weng, A. T. Bell and A. Z. Weber, *Phys. Chem. Chem. Phys.*, 2018, **20**, 16973-16984.

hydrophobic pores, and eventually small hydrophobic pores. Therefore, to control CL wetting, one needs to adjust the pore-size distribution or the wettability of the CL pores.

This chapter studies the GDE design most commonly used for CO_2R that has been implemented in a cell with continuous electrolyte supply.[21-24] We chose Ag as the catalyst because it produces only two gaseous products, H_2 and CO, with > 90% FE to CO.[5, 24] Our model focuses on the CL region and investigates how the local environments in the CL, such as the distributions of CO_2, OH^-, and water change with varying operating conditions and CL properties. We describe quantitatively the advantages of GDEs over planar electrodes and compare the three CL cases: a flooded CL (flooded case), a uniformly wetted CL (ideally wetted case), and a CL described by the saturation curve (saturation curve case). Finally, we explore the effects of varying GDE design parameters (hydrophilicity, loading, and porosity) and operating conditions (electrode potential and electrolyte flowrate).

Model Description

The modeling domain includes the CL and DM, shown in **Figure 3.2**. The CL is assumed to consist of spherical nanoparticles of Ag with radius r_{np} that are loosely packed and bound by a binder and have intrinsic porosity $\epsilon_{\mathrm{CL}}^{o}$. For the flooded case, only solid and liquid phases exist in the CL domain. For the ideally wetted and saturation curve cases, the amount of liquid in the CL is determined by the CL saturation (S is assumed constant for the ideally wetted case). Although empirical in this work, the saturation curve can be related theoretically to structural properties such as the pore-size distribution.[26] However, it is important to note that the saturation curve will change depending on the composition of the CL, and the method used to produce the CL. When describing CL wettability, the saturation curve was shifted up/down by 0.1-unit saturation for a more hydrophilic/hydrophobic CL. This assumes that the CL pore-size distribution remains unchanged, but the fraction of hydrophilic pores is increased (decreased) by 0.1 unit. An equivalent thin-film thickness, $\delta_{\mathrm{TF,eq}}$, is derived from geometric arguments based on the CL saturation by evenly distributing the electrolyte throughout the CL,

$$\delta_{\mathrm{TF,eq}} = r_{\mathrm{p,CL}}\left(1 - \sqrt{1 - S}\right) \tag{3-1}$$

where $r_{\mathrm{p,CL}}$ is the mean CL pore radius. For the ideally wetted CL case, a uniform 10 nm thick electrolyte thin film is assumed. This thickness corresponds to the CL saturation at zero capillary pressure ($S = 0.64$), and is representative of the electrolyte thin-film thickness observed in fuel-cell CLs.[84] While a distribution of the thin-film thickness δ_{TF} may be more accurate, it has been shown in fuel-cell models that the difference between using $\delta_{\mathrm{TF,eq}}$ and δ_{TF} is insignificant, especially within the kinetically controlled regime.[85] The DM is assumed to be completely dry ($S = 0$), with solid volume fraction, $1 - \epsilon_{\mathrm{DM}}^{o}$, and gas volume fraction, $\epsilon_{\mathrm{DM}}^{o}$.

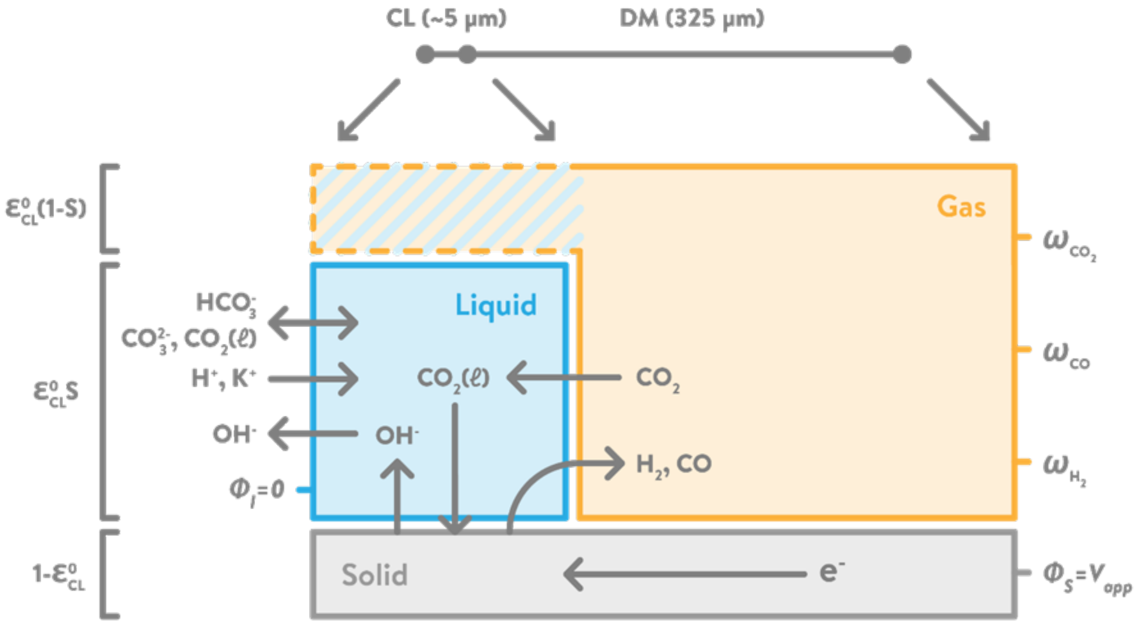

Figure 3.2 Graphical illustration (not to scale) of the 1-D model and different phases within the CL and DM. Hatched portion in the CL domain will be either liquid phase (L) for the flooded case, or gas phase (G) for the ideally wetted and saturation curve cases. Solid phase (S) consists of Ag nanoparticles in the CL and C substrate in the DM. The volume fractions for the three phases in the CL is labelled to the left of the graph.

Results and Discussion

Understanding the improved performance in GDEs

Figure 3.3 compares the results of simulations and experimental measurements by Hatsukade *et al.*[5] for planar electrodes and by Verma *et al.*[24] for GDEs. The model captures the order of magnitude increase in partial CO current density in the GDE compared to the planar electrode. Discrepancies between the simulations and experiments may be due to: (1) lack of information on CL properties used in the experiments; (2) inadequacy of the rate parameters extracted from the data on metal, planar foils for the nanoparticles used in GDEs;[86] (3) the need of additional dimension(s) to properly capture the true current-density distribution.

Figure 3.3a shows that for cathode potentials below –1.1 V vs RHE, the CO partial current density for the GDE is more than an order of magnitude higher than that for the case of planar electrodes, independent of whether the CL in the GDE is flooded or wetted. This difference can be attributed to two main factors. The first is because the GDE contains a higher concentration of catalytically active sites per unit geometric cathode area than does the planar catalyst. This is a consequence of the porous structure of the GDE. The specific interfacial area, a_v^o, for GDEs used in fuel cells have been measured to be in the range of 10^6 to 10^8 m^{-1}, depending on the structure, material, deposition method, *etc.* of the CL.[87-89] We have assumed a value of a_v^o = 3 x 10^7 m^{-1} for the CL, which corresponds to a roughness factor of 114, explaining the two orders of magnitude higher current density at low overpotentials. For cathode potentials more negative than –1.1 V vs RHE, the difference between the CO partial current densities for the GDE and planar electrode systems grows dramatically. This is because the mass-transfer resistance for the GDE is much lower than that for the planar-electrode system. At potentials more negative than –1.1 V vs RHE, the planar electrode becomes CO_2 mass-transfer limited, whereas the CO current densities for the GDE continue to increase exponentially with overpotential as expected if the electrode is kinetically controlled. CO_2 mass transfer to the catalyst of the GDE is much more effective than for the planar electrode because the distance over which mass transfer through the electrolyte occurs is much smaller. For the CL of the GDE, the diffusion layer is in the range of 0.01 to 10 µm, depending on the saturation of the CL, which is much smaller than the boundary-layer thickness for a planar electrode (60 to 160 µm).[12]

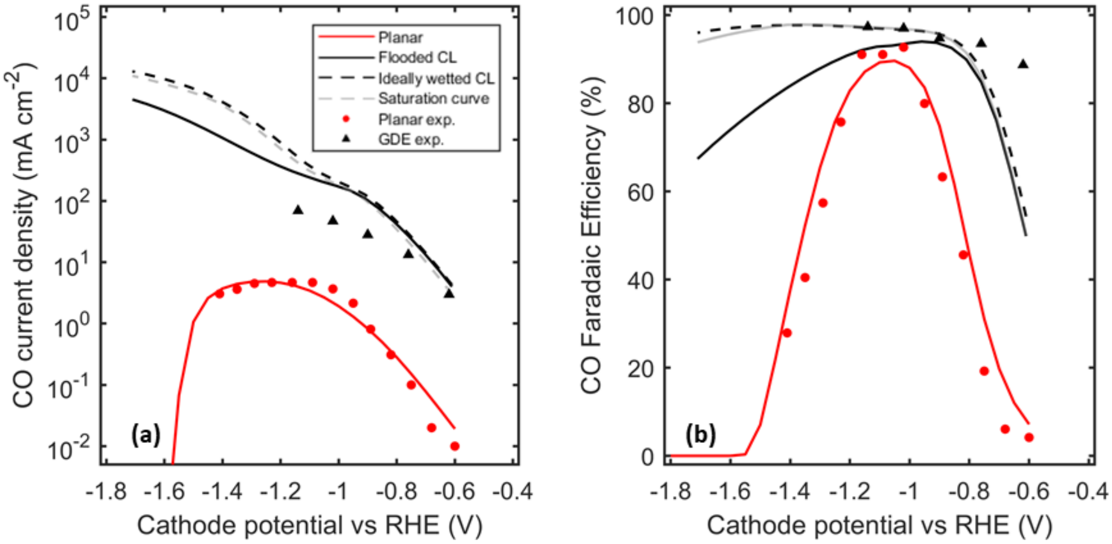

Figure 3.3 (a) CO partial current density and (b) CO Faradaic Efficiency (other product is hydrogen, plotted in S3) as a function of Cathode potential vs RHE for the planar case, flooded case, ideally wetted case, saturation curve case, compared to experimental data measured by Hatsukade *et al.*[5] and Verma *et al.*[24]

One interesting phenomena to note is how the CO current density and CO FE decrease after reaching a maximum. This is due to the reaction of CO_2 with OH^-. As the potential is made more cathodic, the HER current density continues to increase exponentially, producing more OH^- that reacts with the already limited CO_2 near the electrode. This consumption of CO_2 results in the drop in CO current density as well as the FE, while the rate of HER continues to increase. This effect is most noticeable for the planar-electrode system.

Results of flooding in the CL

While the current density is high for a flooded CL, the selectivity towards CO starts to decrease around –1 V vs RHE (**Figure 3.3a**). Even though fully flooded within the CL, the GDL is assumed to remain dry and consequently the catalyst at the CL/GDL interface can still promote CO_2R. As the electrode is driven to more cathodic potentials and the rate of CO_2R rises, the concentration of CO_2 in the electrolyte near the cathode decreases (**Figure 3.4a**). The local CO current density shifts towards the CL/DM boundary, where gas-phase CO_2 is supplied (**Figure 3.4b**). The local CO current density at the electrolyte/CL boundary does not drop as rapidly as it does at the center of the CL because bicarbonate anions from the bulk can decompose to produce CO_2. This

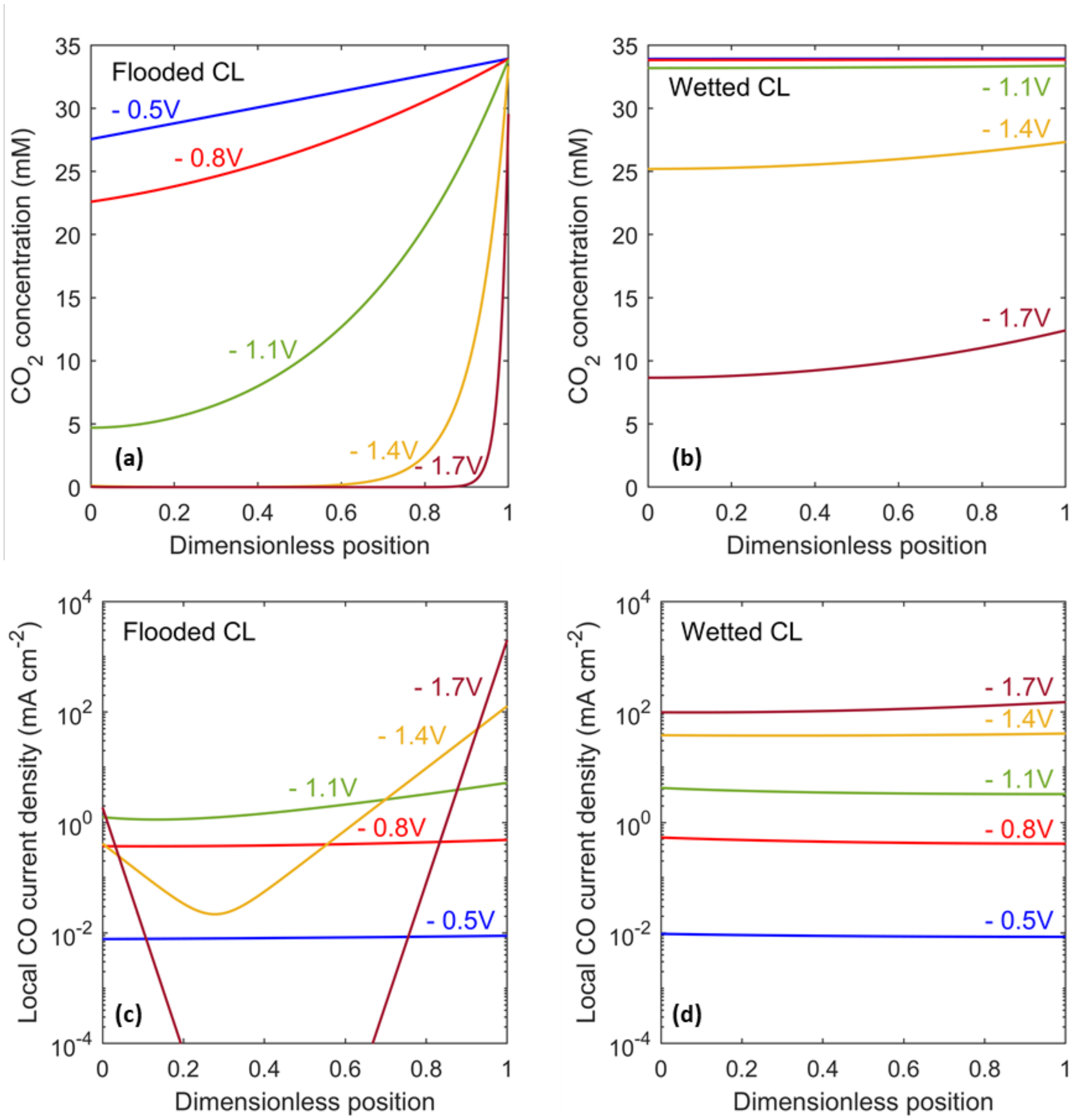

Figure 3.4 CO_2 concentration profile (a & c) and local CO current density (b & d) within the catalyst layer for the flooded case (a & b) and the ideally wetted case (c & d). The dimensionless position is scaled using the CL thickness, where 0 is the electrolyte/CL boundary, and 1 is the CL/GDL boundary.

phenomenon is also in agreement with recent publications showing HCO_3^- as a carbon source for CO_2R to CO.[7, 8] Because of the equilibrium relationships for $CO_2/HCO_3^-/CO_3^=$, a 0.5 M $KHCO_3$ solution not equilibrated with gaseous CO_2 will decompose and produce approximately 5 mM aqueous CO_2 to maintain equilibrium. Therefore CO_2R continues to occur near the electrolyte/CL boundary at high overpotentials. The uneven distribution of CO current density for a flooded CL results in poor utilization of the catalyst. At high cathodic potentials, the overpotential for both COER and HER are high. Catalyst sites that are CO_2 limited continue to perform HER, causing the drop in CO FE.

A partially wetted CL performs better than a flooded CL in terms of both the CO partial current density and the CO FE, especially at high current densities (high overpotentials). Wetted pores allow gas-phase CO_2 to penetrate throughout the CL, resulting in a more even distribution of dissolved CO_2 and local CO current density even at high overpotentials (**Figure 3.4**c-d). The high current densities in GDEs cause high alkalinity in electrolyte within the CL as one OH^- is produced for each electron consumed. This effect is more severe for the wetted CL because it operates at a higher current density than does the flooded CL (**Figure 3.5**). High pH leads to a high K^+ cation concentration, which is required to maintain electroneutrality in the electrolyte in the CL. The high concentrations in the CL also implies a sharp concentration gradient at the electrolyte/CL boundary. For CO current densities above 1.5 A/cm^2, K_2CO_3 may start precipitating from the solution.[80] However, the increased concentration of the counter-ion may also beneficially amplify cation effects, where cations near the electrode stabilizes CO_2R intermediates, when one considers non Ag CO_2R catalysts.[29]

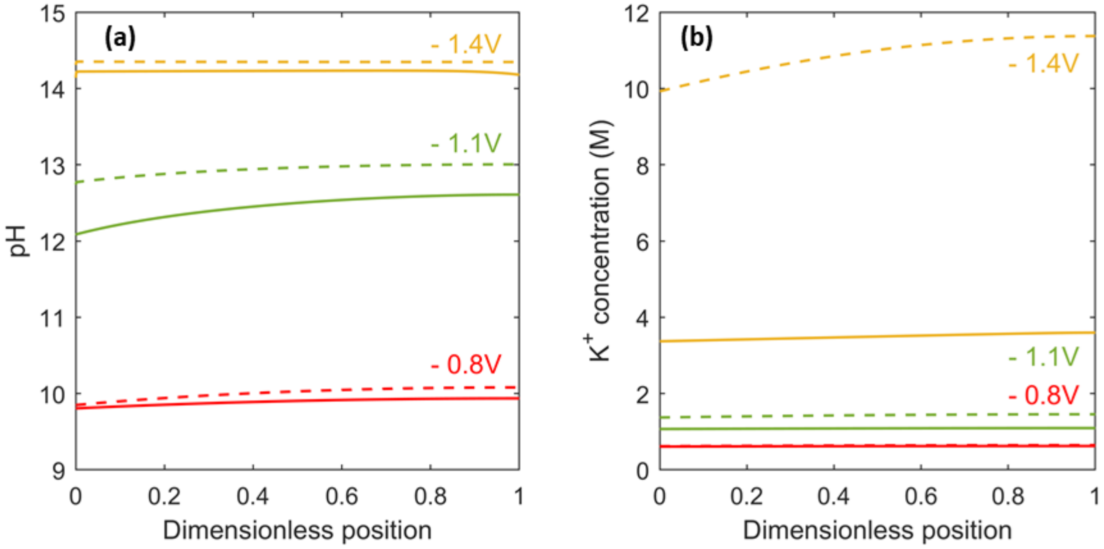

Figure 3.5 (a) pH profile and (b) potassium cation concentration profile within the catalyst layer for the flooded case (solid lines) and wetted case (dashed lines).

Describing saturation/hydrophilicity in the CL

The ideally wetted CL case assumes a constant uniform thin film of electrolyte throughout the CL. However, the CL local environment will change as the electrode consumes CO_2 and produces CO and H_2. Incorporating the saturation curve to describe liquid distribution in the CL results in a slightly lower CO current density and FE than the wetted CL case since only 64% of the total catalyst surface area is active. As the current density increases, the total pressure in the gas phase drops near the electrolyte/CL boundary and more of the CL pores become flooded (**Figure 3.6a**). The effective permeability of the CL decreases, resulting in a lower CO_2 concentration near the electrolyte/CL boundary and a decrease in local CO current density (**Figure 3.6b**). H_2 current density is unaffected since its rate does not depend on concentrations of dissolved gaseous species.

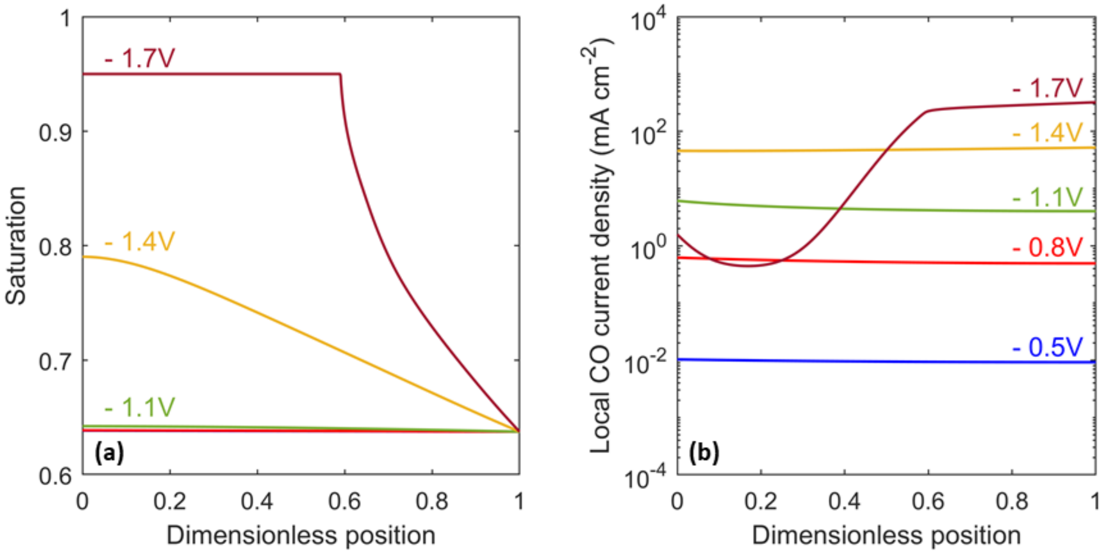

Figure 3.6 (a) Saturation and (b) Local CO current density as a function of position within the catalyst layer at different potentials for the saturation curve case.

The effect of changing the hydrophilicity/hydrophobicity of the CL is depicted in **Figure 3.7**. At low overpotentials, a more hydrophilic CL (higher saturation for a given capillary pressure) enhances performance because it improves pore wetting, giving a higher specific active interfacial area. However, a hydrophilic CL also becomes flooded more easily, leading to worse performance at more cathodic potentials. Thus, there is an optimum that is dependent on operating conditions and desired efficiency and rate (current density).

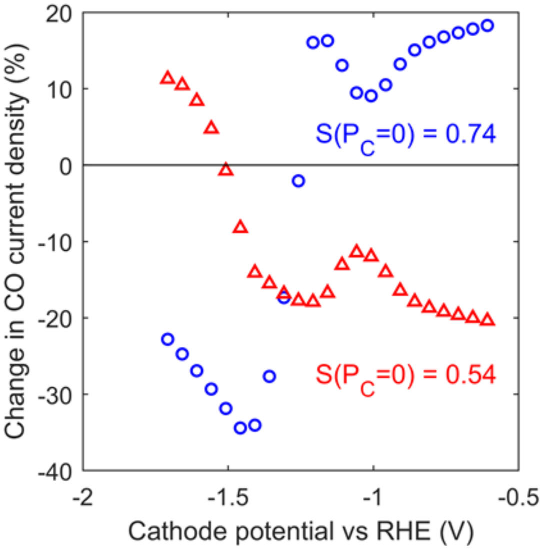

Figure 3.7 Change in CO current density as a function of cathode potential vs RHE for a more hydrophilic CL (blue) and a more hydrophobic CL (orange).

Effects of catalyst loading and CL porosity

The effect of reducing the catalyst loading and, hence, decreasing the CL thickness was examined. For a kinetically controlled system, reducing catalyst loading by 50% halves the current density, as can be seen in **Figure 3.8a** at low overpotentials. However, the change in CO partial current density for the case of 0.5x catalyst loading becomes less significant as the overpotential increases because of the lower mass-transfer resistances in a thinner CL. The trend reverses

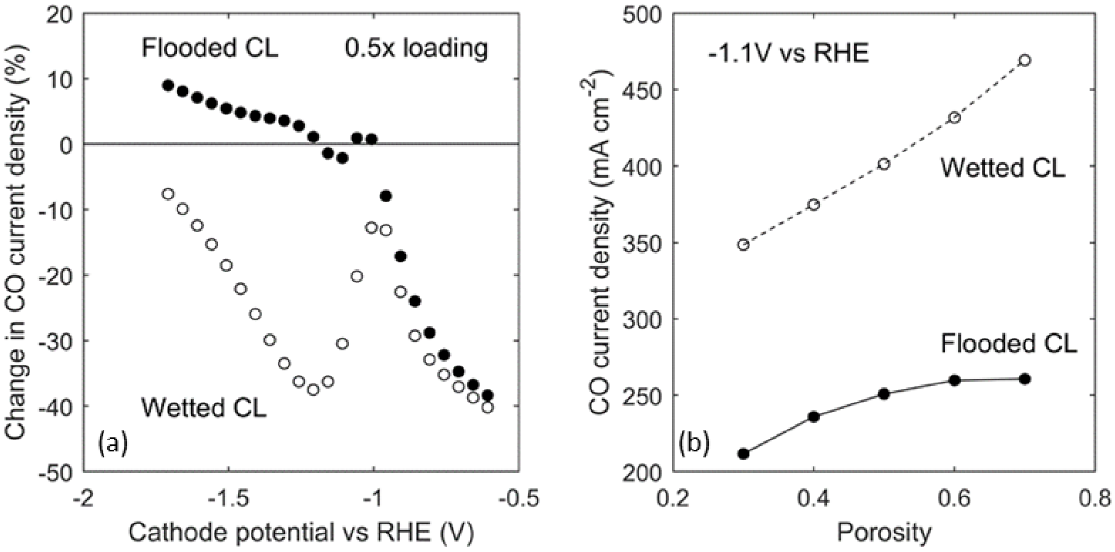

Figure 3.8 (a) Change in CO current density as a function of cathode potential vs RHE at 0.5x loading (0.5x CL length); (b) CO current density as a function of CL porosity. Filled circles represent the flooded case and hollow circles, the ideally wetted case.

around –1 V vs RHE, demonstrating the balance between current density and pH: high current density increases CL pH, which can suppress CO current density by the reaction of CO_2 and OH^-. The poor catalyst utilization in flooded GDEs eventually becomes detrimental at high current densities (i.e., electrode potentials lower than –1.2 V vs RHE), and a lower catalyst loading under such conditions can actually enhance the CO partial current density.

Another property that can be changed is the CL porosity. Increasing porosity enhances gas transport by increasing the gas permeability and effective diffusivity, but requires an increase in the CL thickness to maintain a constant catalyst loading. **Figure 3.8b** shows that it is more effective to increase porosity for a wetted CL than a flooded CL. This makes sense since the mass-transport limitation is more severe in a flooded CL, and increasing its thickness will aggravate the uneven local CO current-density distribution shown in **Figure 3.4b**. For a wetted CL, doubling the CL porosity can improve the current density by about 100 mA/cm^2 at –1.1 V vs RHE.

Effects of electrolyte flowrate

Increasing the electrolyte flowrate improves the mass transport of ionic species and helps to maintain the CL local environment near that of the bulk electrolyte. This is important for GDEs considering the high pH and cation concentration caused by the high current density. However, the model demonstrates that increasing electrolyte flowrate may not be the most effective method to improve electrode performance. As shown in **Figure 3.9**, to achieve a 100 mA/cm^2 increase in CO current density at –1.1 V vs RHE, it is necessary of increase the electrolyte flowrate by an order of magnitude.

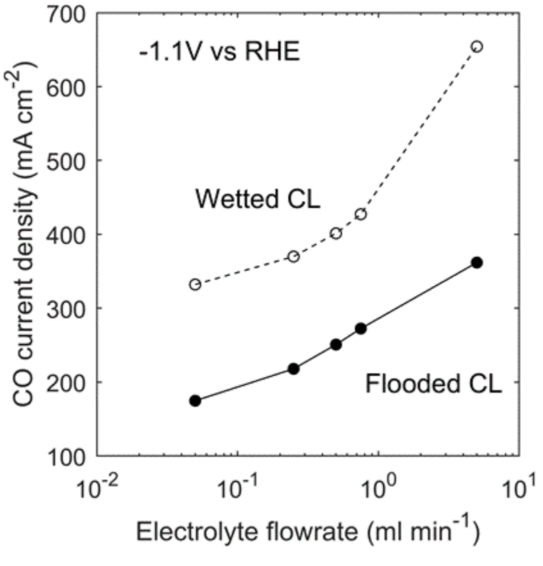

Figure 3.9 CO current density as a function of electrolyte flow rate for the flooded case (filled circles) and the ideally wetted case (hollow circles).

Summary

It was demonstrated and quantified how a GDE improves CO_2R performance by providing a higher active surface area and lower mass-transfer resistances. Electrode properties such as wettability, catalyst loading, and porosity impact the inherent local CO_2 concentration due to the balance between transport through the CL and the reaction of CO_2 with produced OH^-. This balance is sensitive to the operating conditions of the GDE and therefore the optimal property values depend on the desired current density. Our results show that tuning CL wettability can significantly affect the resulting CO current density and CO FE. At high current densities (>100 mA/cm^2), it is important to prevent flooding of the CL, as this may lead to an uneven distribution of CO_2 within the CL and poor utilization of the catalyst. In such a case (operating a flooded CL at high current densities), decreasing the catalyst layer loading may improve the CO partial current density and catalyst utilization. The amount of liquid in the CL can vary depending on position and the operating current density, which in turn affects local CO partial current density distribution within the CL. Manipulation of the porosity and electrolyte flowrate can also improve the CO partial current by as much as twice the amount. The insights gained from the model described in this study can be used to guide the design of GDEs for CO_2R. The integration of GDEs into the electrochemical cell is discussed in the subsequent two chapters.

Chapter 4 Silver-Based Membrane-Electrode Assemblies[‡]

Introduction

MEAs are an attractive cell design for the electrochemical reduction of CO_2 because they exhibit low ohmic loss and high energy efficiency, as outlined in Chapter 1. This chapter discusses the application of a multiphysics model to investigate the fundamental limitations of two Ag-based MEA designs: one with gaseous feeds at both the anode and cathode (full-MEA), and the other with an aqueous anode feed ($KHCO_3$ or KOH exchange solution) and a gaseous cathode feed (exchange-MEA). We outline the advantages and limitations of different MEA cell designs for performing CO_2R and examine potential methods for improving water management in the membrane and the overall cell efficiency.

Model Description

The MEA model comprises a 50-µm anion-exchange membrane (AEM), a 5-µm Ag cathode catalyst layer (CL), and a 100-µm cathode diffusion medium (DM), as shown in **Figure 4.1**. The anode, an IrO_2 mesh pressed against the membrane, is treated as an interface. N_2 with 100% relative humidity (RH) is fed to the anode chamber for the full-MEA, and an aqueous solution is fed for the exchange-MEA; humidified CO_2 (100% RH) is fed to the cathode chamber for both MEA configurations.

The fixed background charge of an ionomer membrane leads to an electric potential difference at the membrane|exchange solution interface, known as the Donnan potential: $\Delta\phi_{\mathrm{D}} = \phi_{\mathrm{L}}^{\mathrm{M}} - \phi_{\mathrm{L}}^{\mathrm{E}}$. At equilibrium, the electrochemical potential of each species in the two phases must be equal, resulting in the following relationship between species concentration in the membrane, c_i^{M}, and in the exchange solution, c_i^{E},

$$c_i^{\mathrm{M}} = c_i^{\mathrm{E}} \exp\left(-\frac{z_i F}{RT}\Delta\phi_{\mathrm{D}}\right) \tag{4-1}$$

The Donnan potential can then be determined by enforcing electroneutrality in the membrane, taking into consideration the background charge by the fixed cationic moieties ($\Delta\phi_{\mathrm{D}}$ is positive for an AEM, due to its fixed positive background charge). This creates an extra energy barrier for cations to enter the membrane ($z_i > 0$, so the exponential term is less than unity), but does not necessarily completely exclude cations from the membrane.

The boundary conditions for the model are summarized in **Figure 4.1**. The electronic potential is set to $\phi_{\mathrm{s}} = 0$ at the cathode boundary, and varied from 2 to 4 V (cell voltage) at the anode boundary. The flux for all species is set to zero at the CL/DM boundary at the cathode. At the anode boundary, CO_2 and H_2O are taken to be in equilibrium with the anode feed gas (inert gas N_2 with 100% RH). The flux for all ionic species is set to zero for the full-MEA case, and for the

---

[‡] This chapter was adapted from L. C. Weng, A. T. Bell and A. Z. Weber, *Energy Environ. Sci.*, 2019, **12**, 1950-1968.

exchange-MEA cases, all species are taken to be in equilibrium with the exchange solution, which is assumed to be at constant concentration. The anode boundary condition assumes fresh exchange solution being circulated at a high flowrate in the anode channel. The fluxes of all gaseous species are set to zero at the membrane|CL boundary, and their mass fractions set to the cathode feed gas composition at the GDL|gas channel boundary. A Robin boundary condition is set at the two boundaries using a heat transfer coefficient, h_T, to describe the heat flux, driven by the difference between the cell temperature at that boundary and ambient temperature, T_o.

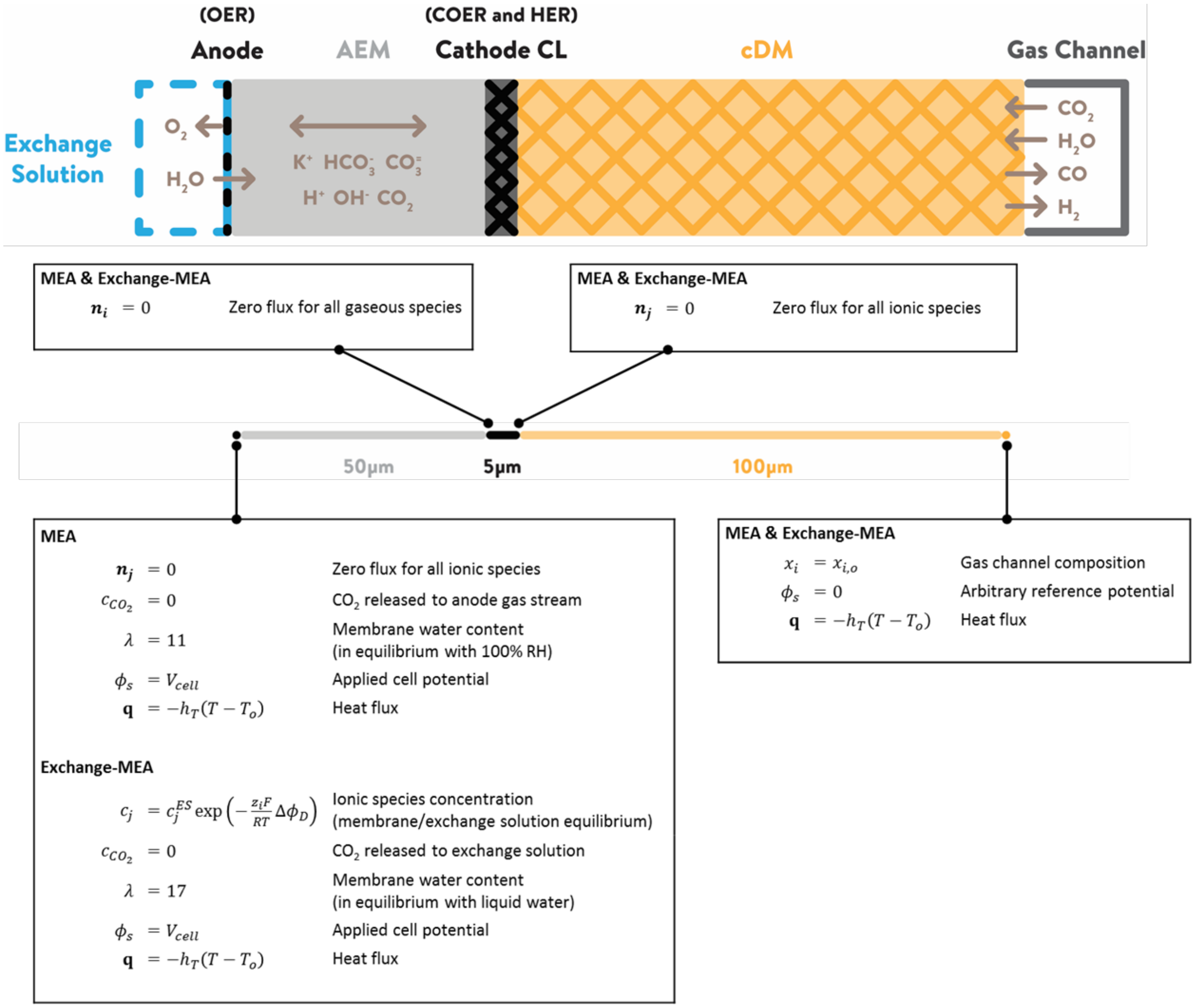

Figure 4.1 Schematic of the 1-D modeling framework and boundary conditions for the Ag-MEA.

Results and Discussion

Applied voltage breakdown and precipitation issues for a full-MEA and exchange-MEAs

Figure 4.2 shows the (a) total current density (TCD) and (b) CO FE for the three cases considered: full-MEA, 0.5 M $KHCO_3$ exchange-MEA, and 0.5 M KOH exchange-MEA. The exchange-MEA's produce a higher TCD and CO FE than the full-MEA at the same applied cell potential, with the KOH exchange-MEA achieving the highest performance. The variance in CO FE for the three cases can be explained by the cathode pH: the alkalinity at the cathode increases in the order MEA < $KHCO_3$ exchange-MEA < KOH exchange-MEA because of the exchange solution, as well as the higher TCD producing OH^- at a higher rate at the cathode.

To understand the trend observed for the TCD, we plot the applied voltage breakdown (AVB) for the three cases (**Figure 4.2c, e, f**). The applied voltage is comprised of the thermodynamic potential, the kinetic overpotential, and the transport overpotential (Nernstian plus ohmic components). The thermodynamic potential depends on the species concentrations near the two electrodes at open circuit. Assuming that all gaseous species are at normal conditions, the thermodynamic potential, η_{th}, for a cell performing OER at the anode and COER at the cathode can be calculated as

$$\eta_{\mathrm{th}} = (U^{o}_{\mathrm{OER}} - U^{o}_{\mathrm{COER}}) + \frac{RT}{F}\ln\left(\frac{c^{\mathrm{C}}_{\mathrm{OH^-}}}{c^{\mathrm{A}}_{\mathrm{OH^-}}}\right) \tag{4-2}$$

where $c^{\mathrm{C}}_{\mathrm{OH^-}}$ and $c^{\mathrm{A}}_{\mathrm{OH^-}}$ refers to the OH^- concentration at the cathode and anode, respectively. The Nernstian overpotential is defined as the potential developed due to the change in OH^- concentration at the electrode relative to that at open circuit,

$$\eta_{\mathrm{N}} = \pm\frac{RT}{F}\ln\left(\frac{c_{\mathrm{OH^-}}}{c^{o}_{\mathrm{OH^-}}}\right) \tag{4-3}$$

The sign on the right side is negative for the anode and positive for the cathode. Therefore, a higher OH^- concentration at the anode during operation would result in a negative (more favorable) Nernstian overpotential, while a higher OH^- concentration at the cathode leads to a positive (less favorable) Nernstian overpotential. The voltage contributions to the OER and HER can be calculated analogously.

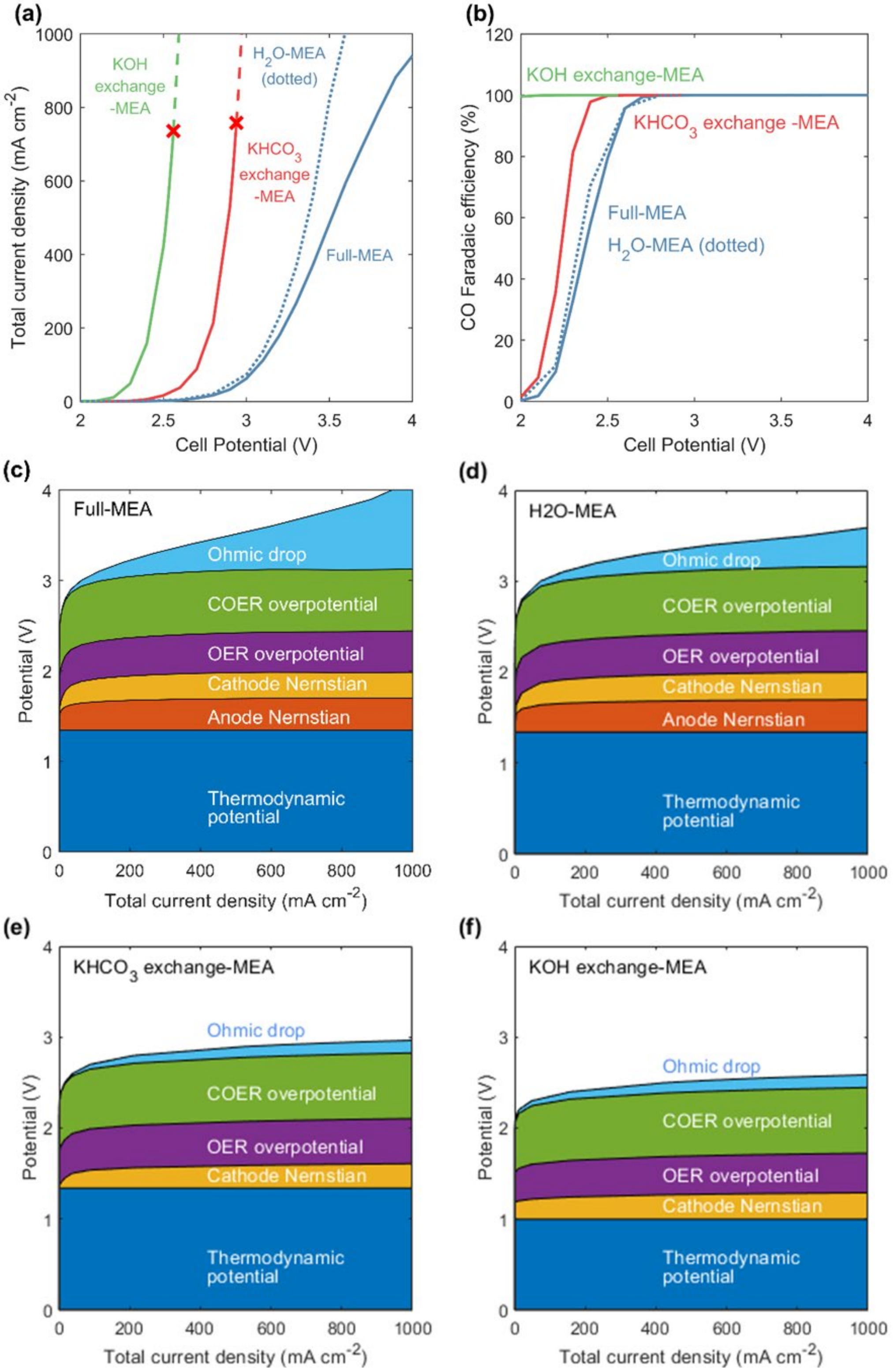

Figure 4.2 (a) The total current density and (b) the CO faradaic efficiency (FE) for the four cases considered and their applied voltage breakdown (AVB), (c) full-MEA, (d) H_2O-MEA, (e) $KHCO_3$ exchange-MEA, and (f) KOH exchange-MEA. Dashed line in (a) represent current densities at which salt precipitates.

Comparison of the AVBs clearly shows that the exchange-MEAs substantially minimize two overpotential sources observed in the full-MEA case: the anode Nernstian potential and the ohmic drop. The anode Nernstian potential is eliminated in the exchange-MEAs because the local environment at the anode is maintained by the circulating exchange solution. In contrast, sharp concentration gradients develop in the full-MEA and increase with increasing TCD, as shown in **Figure 4.3a**. The exchange solution also improves membrane hydration, and, consequently, its conductivity, thereby decreasing the ohmic drop across the cell. For a full-MEA, the membrane water content decreases with increasing current density (**Figure 4.4a**) because the water concentration in the gas channel is limited to its vapor pressure and water is transported and consumed in the HER and CO_2R reactions. Furthermore, as the temperature of the cell increases (**Figure 4.4d**), the gas-phase RH decreases (**Figure 4.4b**) even though the partial pressure of water increases (**Figure 4.4c**), causing water in the CL ionomer to evaporate. Finally, the KOH exchange solution reduces the thermodynamic potential of the system due to the OH^- concentration gradient that develops: the anode remains at the concentration of the circulating KOH solution, while the OH^- concentration is lower near the cathode as the CO_2 feed at the cathode gas channel neutralizes the OH^- (**Figure 4.3b**). The concentration profile where the anode OH^- concentration is higher than that at the cathode is opposite to the one established for the full-MEA and $KHCO_3$ exchange-MEA, resulting in a lower thermodynamic potential, or a negative (more favorable) Nernstian potential. A higher OH^- concentration at the anode compared to the cathode makes the second term on the right side of Eq. (4-2) negative, thereby decreasing the thermodynamic overpotential for the KOH exchange-MEA (**Figure 4.2f**).

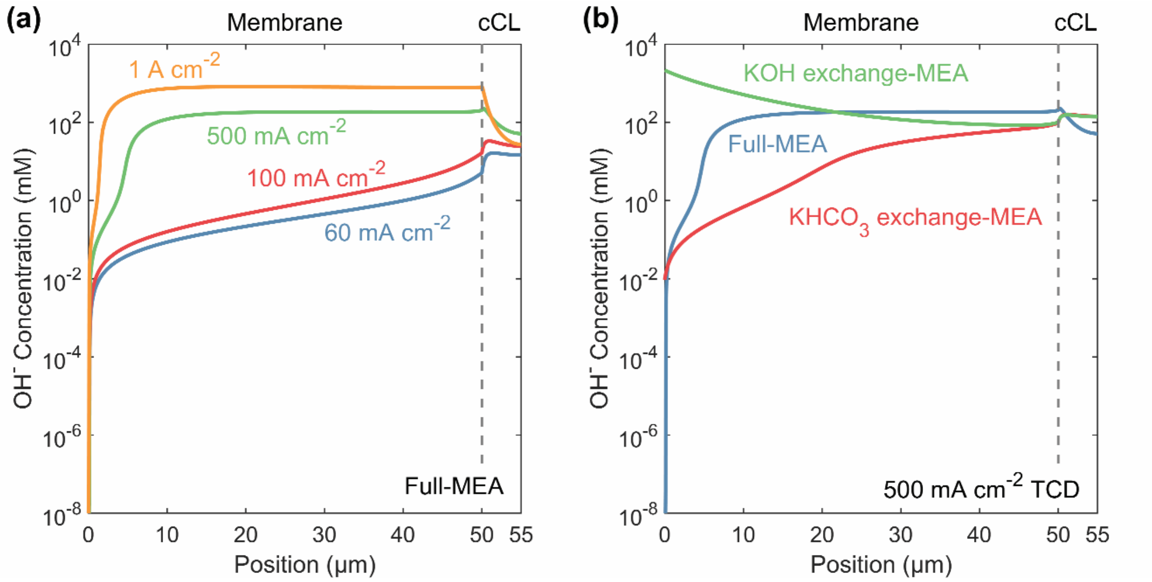

Figure 4.3 OH^- concentration across (a) a full-MEA at 60, 100, 500 and 1000 mA/cm2; and (b) at 500 mA/cm2 comparing full-MEA, $KHCO_3$ exchange-MEA, and KOH exchange-MEA. The hydroxide concentration across the full-MEA increases with increasing current density, creating significant concentration (Nernstian) overpotentials. In the case of KOH exchange-MEA, the hydroxide concentration is reversed due to the bicarbonate buffer reactions at the cathode side, resulting in a negative Nernstian overpotential.

The main limitation for the exchange-MEAs is the precipitation of K_2CO_3 at the cathode. Driven by both the chemical and electric potential gradients, K^+ exchanges with H^+ produced at the anode and moves to the cathode. Eventually, at ~750 mA/cm^2, the concentration of K_2CO_3 exceeds its solubility limit and it precipitates at the cathode (indicated by the red crosses in **Figure 4.2a**). Therefore, operation with salt removal is required to operate exchange-MEAs at current densities above that where precipitation can occur. It is possible to offset this precipitation limit

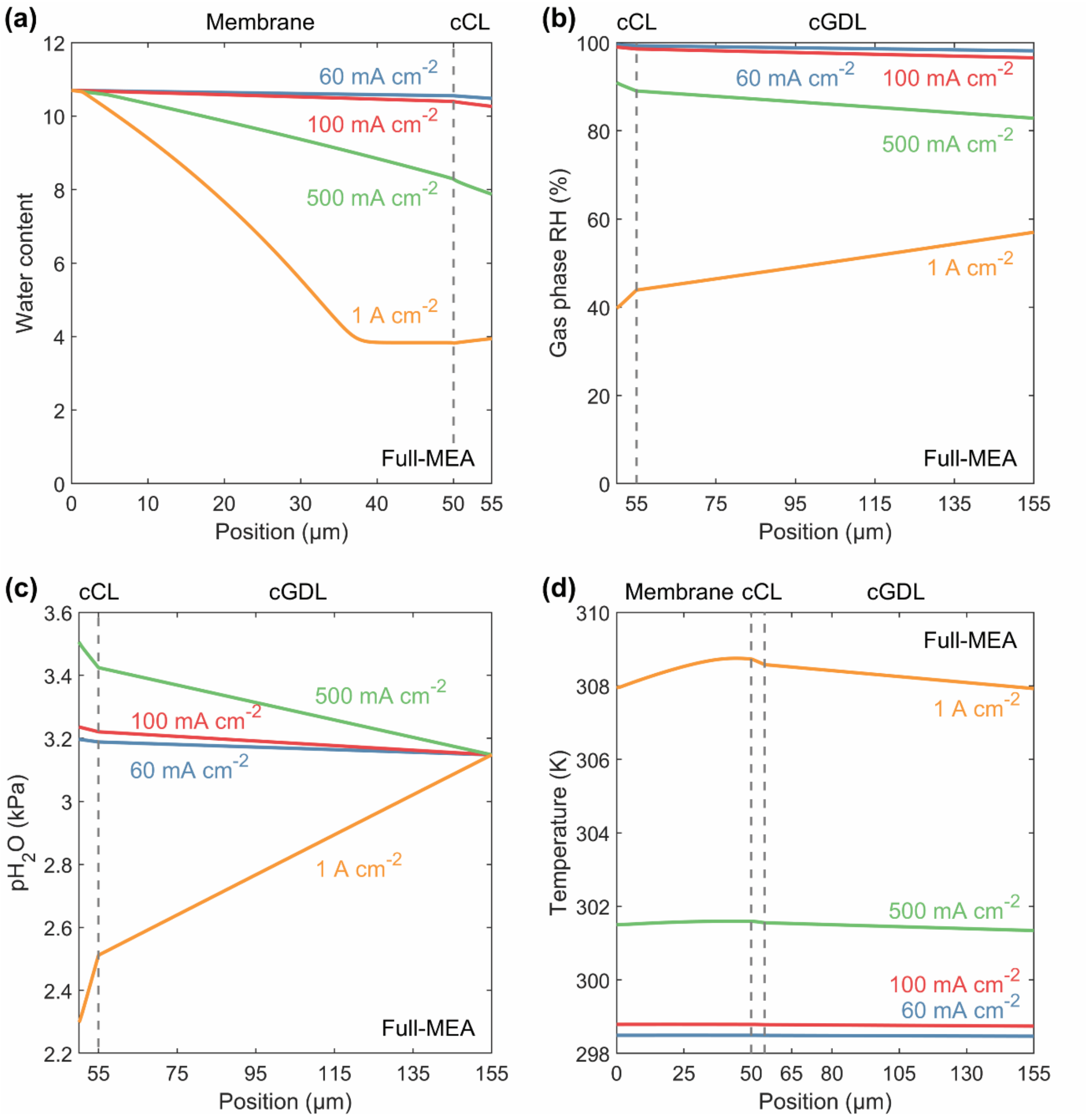

Figure 4.4 (a) Water content in the membrane, (b) gas phase RH, (c) water partial pressure in the gas phase, and (d) the temperature for a full-MEA at 60, 100, 500, and 1000 mA/cm^2. The gas phase RH decreases with increasing current density because of the increase in vapor pressure as the cell heats up. Cathode feed composition is 97 mol% CO_2 and 3 mol% H_2O (water vapor pressure at 25°C).

by feeding liquid water to the anode in order to provide better hydration. A H_2O-MEA improves the total current density (but not the CO FE) of the full-MEA due to better membrane hydration, but does not provide the same advantageous as an exchange-MEA with dissolved salt (**Figure 4.2d**) because of its inability to exchange ions. Thus, exchange-MEAs exhibit low voltage for a given current density but the full-MEA allows achievement of higher current densities without consideration of additional engineering controls.

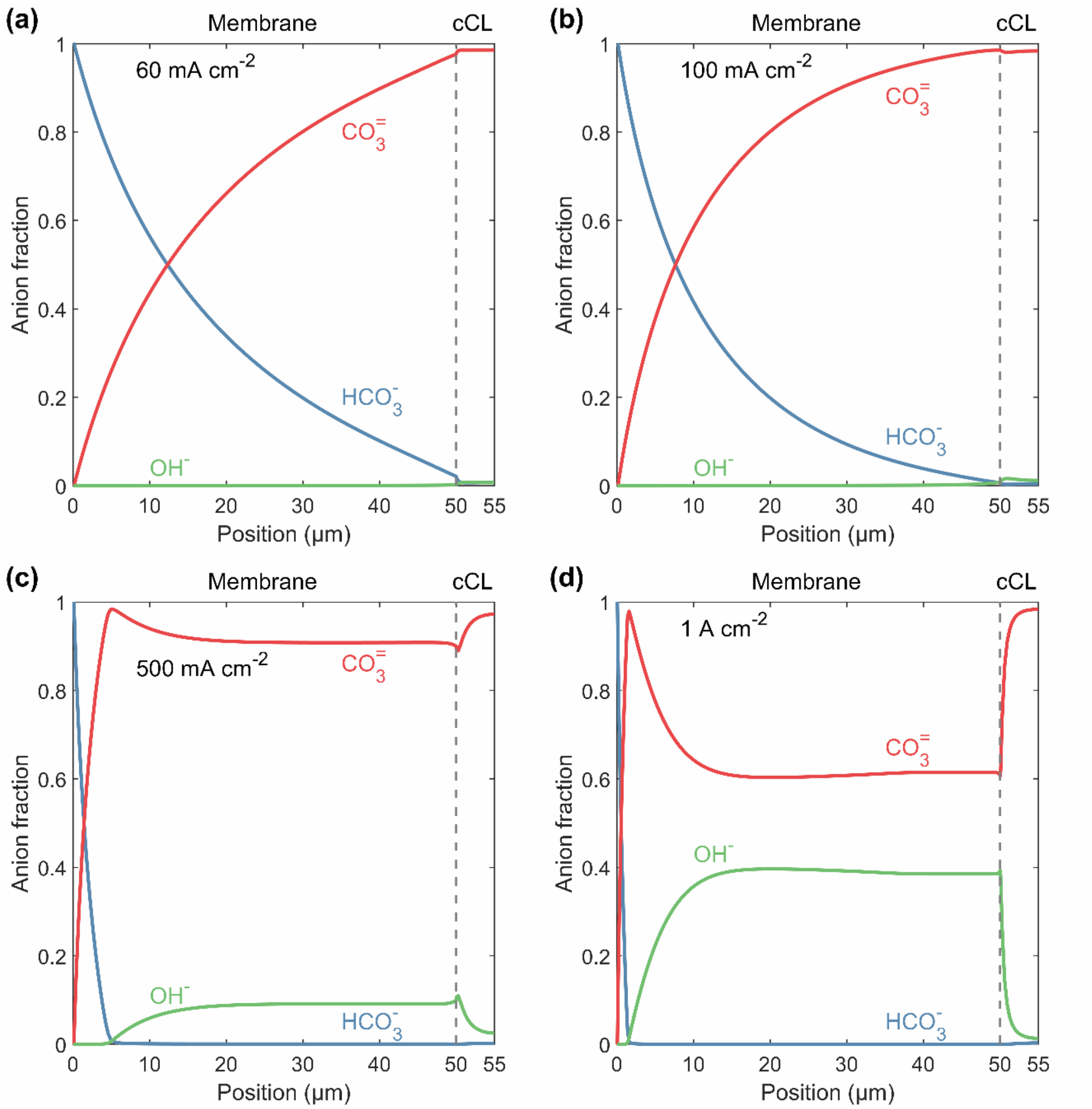

Figure 4.5 Anion distribution in the membrane and cathode CL across a full-MEA cell at (a) 60 mA/cm^2, (b) 100 mA/cm^2, (c) 500 mA/cm^2, and (d) 1 A/cm^2. CO_2 is converted to $CO_3^=$ at the cathode by the OH^- produced from COER, transported as $CO_3^=$ to the anode, and released by the H^+ produced from OER. Cathode feed composition is 97 mol% CO_2 and 3 mol% H_2O.

Ion transport and the charge-carrying species in a full-MEA

At equilibrium, an OH^- form AEM exposed to CO_2 will convert to $HCO_3^-/CO_3^=$ form due to bicarbonate buffer reactions. The ratio of $HCO_3^-/CO_3^=$ depends on the partial pressure of CO_2 in contact with the membrane and has been measured experimentally for an AEM exposed to 400 ppm CO_2.[90, 91] **Figure 4.5** shows the distribution of anion fraction ($|z_i c_i|/c_\mathrm{M}$) across the MEA for low, medium, and high current densities. As the current density increases, the membrane gradually converts to the $CO_3^=$ form, and eventually to the OH^- form starting from the cathode side. This occurs because OH^- is produced by the COER and HER at the cathode. OH^- reacts with the HCO_3^- initially in the membrane to form $CO_3^=$; OH^- also reacts with dissolved CO_2 to form HCO_3^- and eventually $CO_3^=$. The $CO_3^=$ then transports from the cathode to the anode, driven by its concentration gradient (diffusion), and the potential gradient (migration). At the anode, bicarbonate buffer reactions drive the conversion of $CO_3^=$ to HCO_3^- and eventually back to CO_2, which is released into the anode gas channel; thus, a CO_2 pump is realized. As the current density increases, the rate of OH^- production at the cathode also rises, eventually exceeding the homogeneous reaction rates, resulting in accumulation of OH^- at 500 mA/cm^2 and 1 A/cm^2, as shown in **Figure 4.5c** and **Figure 4.5d**.

Regarding the transport and distribution of species across the MEA: (1) $CO_3^=$ is the main charge carrying species for a full-MEA with an AEM performing CO2R, consistent with experimental observations reported by Liu *et al.*[92] The HCO_3^- diffusion flux from anode to cathode is larger than its migration flux from cathode to anode, which means HCO_3^- is moving against the flow of current. OH^- begins to accumulate at high current densities and the membrane will eventually return to the OH^- form as the charge-transfer rate exceeds the homogeneous reaction rates. (2) A portion of the CO_2 fed at the cathode is transported as $CO_3^=$ and eventually released as CO_2 at the anode for a full-MEA. CO_2 in the anode gas outlet has also been observed by Liu *et al.* and Pătru *et al.*[92, 93] For $KHCO_3$ exchange-MEA and KOH exchange-MEA, CO_2 can be flushed out as $HCO_3^-/CO_3^=$ by the exchange solution. While helpful in terms of performance, this becomes a source of inefficiency for the system in terms of CO_2 utilization as discussed below.

CO_2 utilization efficiency and observed limitations

The CO_2 losses need to be defined and quantified as a function of operating conditions because a portion of the CO_2 is consumed homogeneously at the cathode, transported to and released at the anode (i.e., electrochemically pumped in a similar fashion as that observed in AEM fuel cells[94]). Using the gaseous species fluxes obtained from the model and assuming a 50 sccm CO_2 feed at 100% RH (97 mol% CO_2), the CO_2 consumption (the percentage of CO_2 feed that is consumed either electrochemically or by homogeneous reactions) and the CO_2 conversion (the percentage of CO_2 feed that is converted to CO) as a function of the TCD (**Figure 4.6a**) is derived. More specifically,

$$\mathrm{CO_2\ consumption} = \frac{\text{Molar flowrate of } \mathrm{CO_2} \text{ into the DM from the gas channel}}{\text{Inlet molar flowrate into the cell}}$$

and

$$\mathrm{CO_2\ conversion} = \frac{\text{CO partial current density converted to molar flowrate}}{\text{Inlet molar flowrate into the cell}}.$$

The CO_2 conversion for the three cases deviates slightly from each other at low TCD due to differences in the CO FE (not visible in figure), and eventually converges as CO FE approaches 100% for all three cases. At 100% CO FE, the CO_2 conversion scales linearly with the TCD (which is equal to the partial CO current density), as expected. CO_2 consumption is higher for the KOH exchange-MEA case at low TCD because CO_2 constantly reacts with the OH^- from the exchange solution, resulting in a lower CO_2 utilization efficiency (defined as the ratio of CO_2 conversion to consumption), shown in **Figure 4.6b**. For the full-MEA and $KHCO_3$ exchange-MEA, since the membrane is in the HCO_3^- form (and does not consume CO_2 as the OH^- does) for TCD close to zero, the utilization efficiency starts at a higher value than that for a KOH exchange-MEA, and decreases with increasing TCD as more OH^- is produced. As the TCD increases, the OH^- concentration in the CL becomes comparable for a $KHCO_3$ exchange-MEA and a KOH exchange-

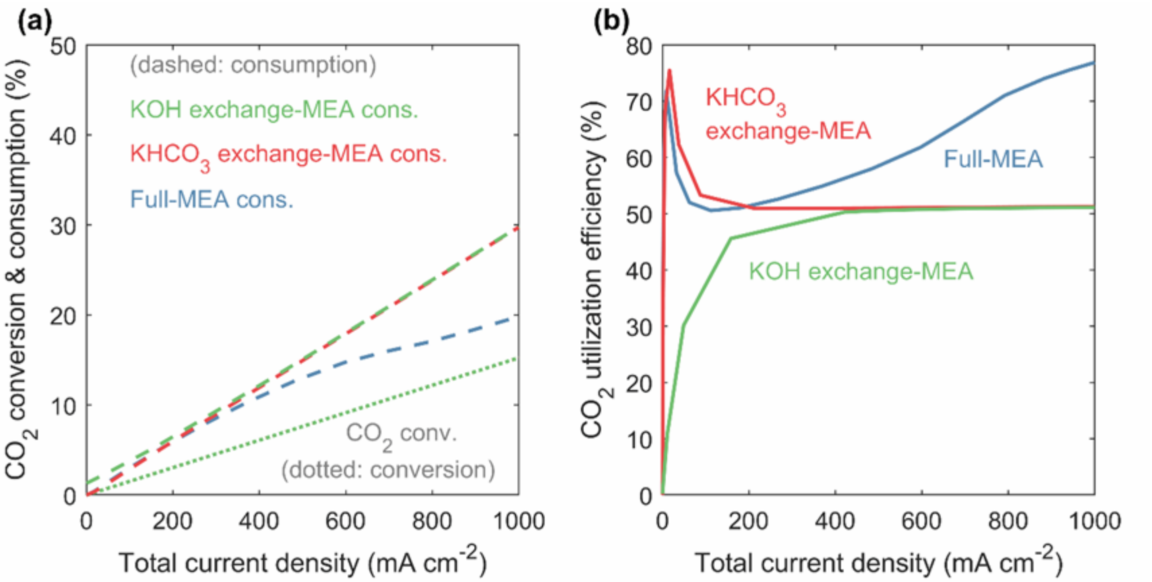

(c)

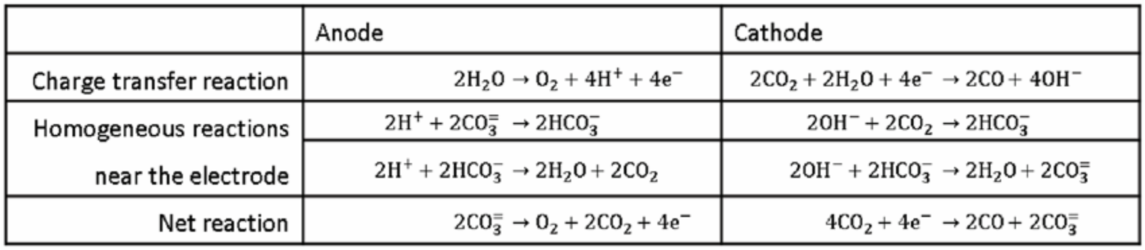

	Anode	Cathode
Charge transfer reaction	$2H_2O \rightarrow O_2 + 4H^+ + 4e^-$	$2CO_2 + 2H_2O + 4e^- \rightarrow 2CO + 4OH^-$
Homogeneous reactions near the electrode	$2H^+ + 2CO_3^= \rightarrow 2HCO_3^-$	$2OH^- + 2CO_2 \rightarrow 2HCO_3^-$
	$2H^+ + 2HCO_3^- \rightarrow 2H_2O + 2CO_2$	$2OH^- + 2HCO_3^- \rightarrow 2H_2O + 2CO_3^=$
Net reaction	$2CO_3^= \rightarrow O_2 + 2CO_2 + 4e^-$	$4CO_2 + 4e^- \rightarrow 2CO + 2CO_3^=$

Figure 4.6 (a) CO_2 consumption (dotted) and conversion (dashed) calculated for a 50 sccm CO_2 feed at 100% RH (97 mol% $CO_{2,}$ 3 mol% H_2O), room temperature. (b) CO_2 utilization efficiency defined as the fraction of CO_2 consumed that converts to CO. (c) Stoichiometric balance of the electrochemical and homogenous reactions across the cell showing only half of the CO_2 consumed is converted to CO.

MEA, but remains slightly lower for a full-MEA (**Figure 4.3b**). The lower OH^- concentration in the full-MEA CL means less CO_2 consumption by homogeneous reactions, as shown in **Figure 4.6a**, as well as a higher CO_2 utilization efficiency (**Figure 4.6b**). The utilization efficiency for $KHCO_3$ exchange-MEA and KOH exchange-MEA converges to 50% for TCD > 500 mA/cm^2, a result that can be explained by considering the stoichiometry of the electrochemical and homogeneous reactions, listed in **Figure 4.6c**. The reaction stoichiometry also suggests a 1:2 O_2 to CO_2 ratio at the anode gas outlet, consistent with measurements by Liu *et al.*[92] To increase the utilization efficiency for exchange-MEAs, the consumption of CO_2 by OH^- needs to be reduced, which could be achieved by a lower rate coefficient for the homogeneous reaction of CO_2 and OH^-. However, this would also result in a more rapid pH change near the cathode, and a larger Nernstian overpotential. Understanding such tradeoffs is crucial to fine-tuning the cell design and maximizing efficiency.

In the model, the gas-channel composition is assumed to remain constant at the feed composition, which is valid only under conditions of low feed consumption (e.g., high feed flowrate). Note that CO_2 concentration varies in the CL**.** In practice, however, CO_2 consumption can be as high 30% for a feed flowrate of 50 sccm and 1 A/cm^2, as shown above. This means that the gas composition in the cathode gas channel will vary based on the rate of consumption of CO_2 and H_2O, and the rate of production of CO and H_2. Assuming that the gas channel is well-mixed, its composition can be calculated from a simple mass balance:

$$y_{\mathrm{GC},i} = \frac{N_{\mathrm{F},i} - N_{\mathrm{R},i}}{N_{\mathrm{F}} - N_{\mathrm{R}}} \tag{4-4}$$

where $y_{\mathrm{GC},i}$ is the mol fraction of gaseous species i in the gas channel; N_{F} and N_{R} are the total molar flowrate of the feed gas going into and out of the gas chamber into the GDL, respectively; $N_{\mathrm{F},i}$ and $N_{\mathrm{R},i}$ are the molar flowrate of species i in the feed gas going into and out of the gas channel, respectively. **Figure 4.7** shows the resulting gas channel composition for the full-MEA (**Figure 4.7a**) and the KOH exchange-MEA (**Figure 4.7b**). At zero TCD, the gas composition in the cathode gas channel for the full-MEA is close to its feed composition since there are minimal reactions and crossover occurring. For the KOH exchange-MEA case, however, the CO_2 mole fraction is much lower than that in the feed (0.97) because CO_2 will be consumed by OH^- anions in the CL ionomer; the H_2O mole fraction is higher due to diffusion of H_2O from the anode chamber. The CO mole fraction increases steadily and the H_2 mole fraction is close to zero, as expected from the partial current densities. However, two issues become apparent regarding water management. For the full-MEA, the H_2O mole fraction first increases slightly due to the temperature increase in the CL, as sesen in **Figure 4.4**, and then drops to zero at approximately 750 mA/cm^2, indicating that the full-MEA becomes limited by the supply of water before it is limited by the supply of CO_2. On the other hand, the partial pressure for H_2O in the gas channel of the KOH exchange-MEA is significantly above its vapor pressure at ambient temperature (~0.03 atm), suggesting that flooding is likely to occur at the cathode GDE as water diffuses from the anode. Flooding in the cathode GDE will increase CO_2 mass-transport resistances significantly and decrease catalyst utilization.[33] **Figure 4.7** suggests a need for a higher-dimensional, integrated multiphase model to capture changes in the gas-channel composition, as well as additional physics to capture water condensation and multiphase flow in the GDE, some of which are discussed in Chapter 5.

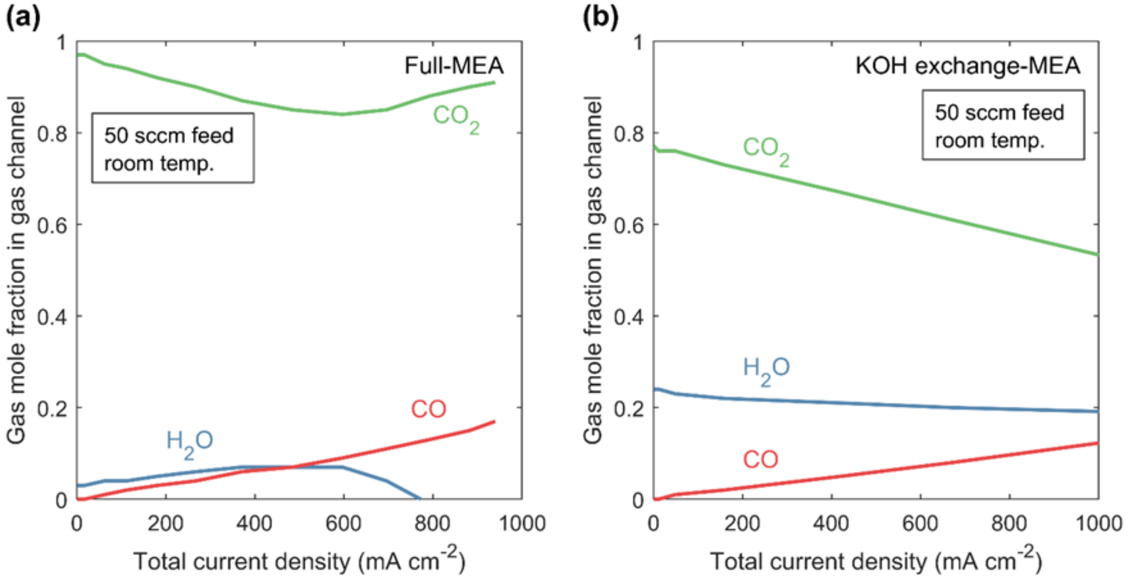

Figure 4.7 Gas mol fraction in the cathode gas channel calculated assuming 50 sccm CO_2 feed with 100% RH (97 mol% CO_2, 3 mol% H_2O) at room temperature for (a) full-MEA and (b) KOH exchange-MEA. The vapor pressure at 298 K is 0.03 atm. Full-MEA becomes water-limited at approximately 750 mA/cm^2, and KOH-MEA is likely to be flooded.

Effects of the operating temperature and membrane thickness on water management

One way to address issues concerning full-MEA dehydration and exchange-MEA flooding is to increase the capacity or mole fraction of water vapor in the feed by increasing the operating temperature or manipulating water transport across the membrane by changing the membrane thickness. In terms of the operating temperature, the water vapor pressure is ~0.46 atm at 350 K, compared to ~0.03 atm at 298 K. Thus, operating at 350 K, a higher TCD can be achieved with more rapid kinetics, but the CO FE decreases below a cell potential of 3 V due to the lower solubility of CO_2 at elevated temperatures (**Figure 4.8a** and **Figure 4.8b**). The gas-channel composition shown in **Figure 4.8c** also indicates that a current density of 1 A/cm^2 lies below the CO_2- or H_2O-limited current densities for a full-MEA. It should be noted that to obtain the same molar flowrate of CO_2 at 350 K as at 298 K for a feed flowrate of 50 sccm, the feed flowrate needs to be raised to 105 sccm in order to compensate for the higher vapor pressure of water. However, **Figure 4.8c** shows that the full-MEA can operate up to 1 A/cm^2 even at a third of the CO_2 molar flowrate provided at 350 K. This observation reinforces our finding that the cell is operating in a low CO_2 utilization regime up to 1 A/cm^2 at 50 sccm feed (**Figure 4.6**).

The operating temperature can also affect CO_2 utilization, as it changes the rates of electrochemical and homogeneous reactions, as well as the equilibrium constants of the bicarbonate and water reactions. Since limited data is available for the buffer reaction rate constants in an ionomer, we show results assuming the same forward rate constants at 80°C as at 25°C for the bicarbonate reactions. The equilibrium constant will vary, as well as the reverse rate constant ($k_{-n} = k_n/K_n$). As shown in **Figure 4.8d**, better CO_2 utilization can be achieved at higher temperatures when operating below approximately 600 mA/cm^2 TCD, but the reverse is true when operating at higher TCDs. This effect is a consequence of increased diffusivity of ionic and neutral species, the shifted equilibria for the bicarbonate/carbonate buffer reactions, and the relative rates of the homogeneous consumption of CO_2 and its electrochemical conversion at

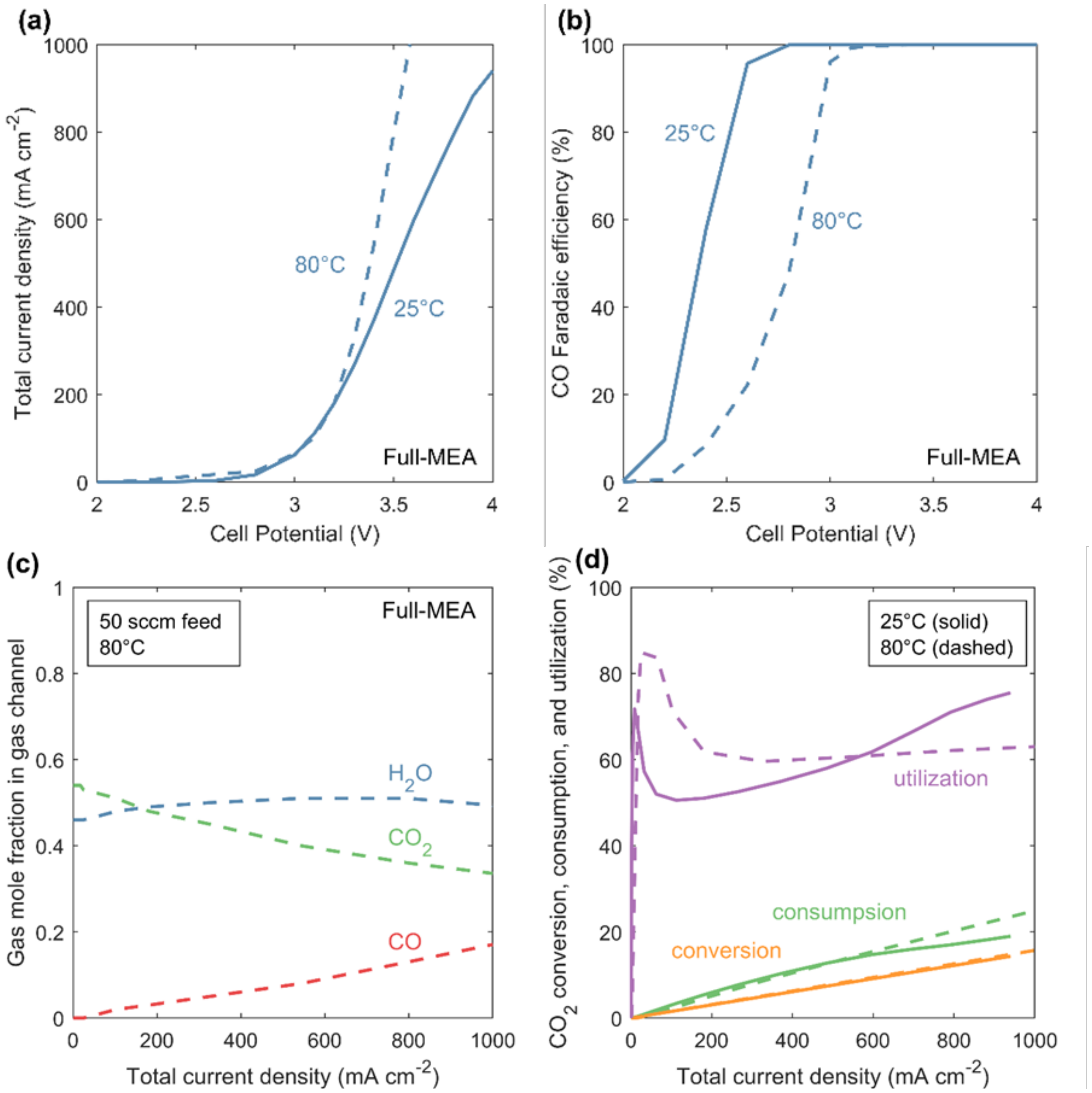

Figure 4.8 (a) Total current density, (b) CO faradaic efficiency, and (c) gas channel composition for a full-MEA at 350 K with CO_2 feed at 100% RH (54 mol% CO_2, 46 mol% H_2O). Operating the cell at higher temperature increases the exchange current density, as well as water feed to the system. However, CO_2 solubility is compromised, resulting in lower CO faradaic efficiencies.

80°C. We note that the results shown here are based on the assumed temperature dependence of the various rate constants, which will vary based on the ionomer used. These results demonstrate the importance of studying homogenous reaction rates of the bicarbonate buffer system in different ionomer environments under various temperatures; manipulation of the bicarbonate buffer reaction rates is a potential route to increase CO_2 utilization of CO_2R systems.

Finally, as noted, one can also decrease the membrane thickness to help alleviate the dehydration issue in full-MEAs (although perhaps not the flooding issue in exchange-MEAs). **Figure 4.9** shows the effects of membrane thickness on the full-MEA performance. As expected, the TCD increases with a thinner membrane, with the difference becoming more significant with higher cell potentials due to both enhanced water transport as well as less ohmic losses, thereby reinforcing the finding that the full-MEA is ohmic-limited. Unlike changing temperature, the CO FE is not strongly impacted. Of course, decreasing the membrane thickness will result in increased crossover and worse CO_2 utilization. This is another tradeoff to consider and is more prominent when producing aqueous products that have high solubility in the membrane.

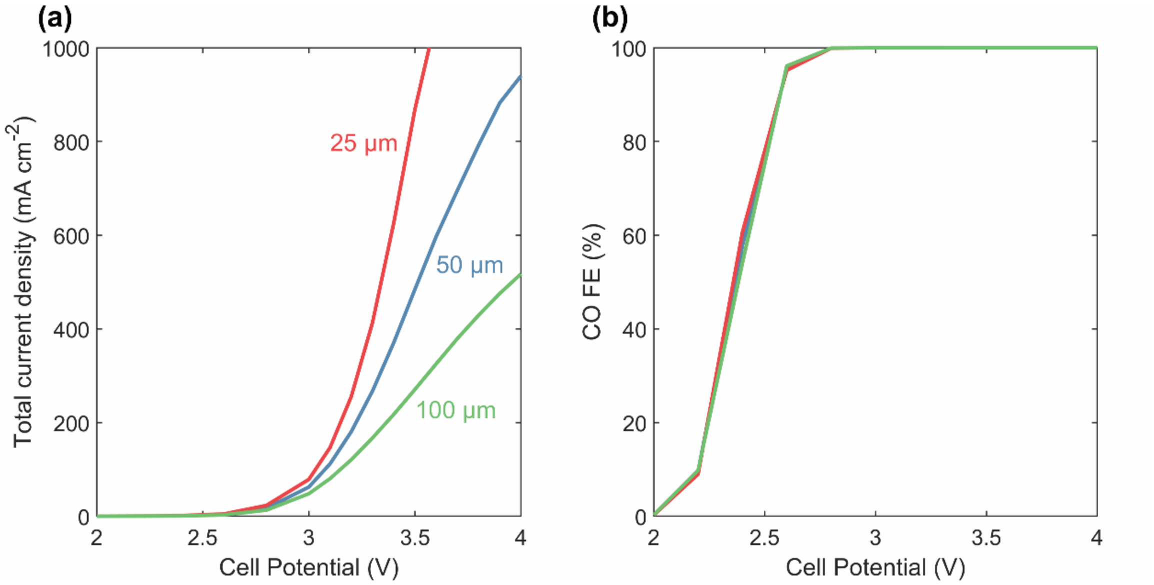

Figure 4.9 (a) Total current density, (b) CO faradaic efficiency for the full-MEA case simulated with a 25 µm membrane (red), 50 µm membrane (base case, blue), and 100 µm membrane (green).

Summary

This chapter discusses the performance and limitations of the electrochemical reduction of CO_2 to CO over Ag in an MEA configuration. As the current density rises above 100 mA/cm^2, MEAs become advantageous relative to planar cells containing an aqueous electrolyte or an aqueous GDL cell because they minimize the ohmic drop across the cell. However, such cells suffer from concentration polarization and membrane dehydration. Circulating an exchange solution through the anode channel enables an exchange-MEA to better maintain the local environment at the anode and hydrate the membrane. With a KOH-exchange-solution feed, a reverse OH^- concentration gradient develops across the cell, lowering the thermodynamic potential that needs to be overcome. The alkaline environment created by KOH also suppresses the HER. For exchange-MEAs, cation transport down the potential gradient limits the current density due to precipitation of the salt used in the exchange solution. It should also be noted that flooding is likely to occur in the cathode GDE of an exchange-MEA, as water diffuses from anode to cathode; this is explored in more detail in Chapter 5. High-temperature operation of a full-MEA allows introduction of more water vapor into the system, thereby overcoming the water limitations observed at room temperature. This also improves the charge transfer kinetics, although the reduction in CO_2 solubility and the changes in the homogeneous reaction rates and reaction equilibria can affect the CO FE and the CO_2 utilization efficiency of the cell. It is also possible to minimize flooding in an exchange-MEA by increasing the temperature at the cathode GDE in order to evaporate condensed water.

Chapter 5 Copper-Based Membrane-Electrode Assemblies

Introduction

By decreasing CO_2 diffusion length to the catalyst, GDEs minimize not only CO_2 mass-transfer resistances, but also the unfavorable CO_2/OH^- interactions, allowing CO_2R to occur in much more alkaline environments, suppressing the unfavorable HER.[24, 33, 39] The operation of Cu-based GDEs under alkaline conditions has also been shown to attain higher faradaic efficiencies (FEs) for C_{2+} products, which are desirable because of their high energy densities and market value.[39, 49, 50, 95] Finally, MEAs have proven to be effective in minimizing cell ohmic losses and circumventing issues associated with having the GDE in direct contact with an aqueous electrolyte, such as electrode flooding and salt precipitation, as discussed in Chapter 4.[39, 41, 96] Therefore, Cu-MEAs provide an opportunity to achieve high energy efficiencies (EEs) for the desired products while maintaining a high production rate.

This chapter discusses the performance and limitations of Cu-MEAs deduced from multiphysics simulations. We break down the overpotentials required to drive various processes and explore ways to minimize them. Our analysis shows how catalyst layer properties, membrane properties, and operating conditions impact cell performance and product distribution through the complex interplay and tradeoffs of various physical processes.

Model Description

Figure 5.1 shows the schematic and dimensions of the base case model in this study. It is a one-dimensional model with five domains: anode/cathode diffusion medium (aDM/cDM), anode/cathode catalyst layer (aCL/cCL), and an anion-exchange membrane (AEM).

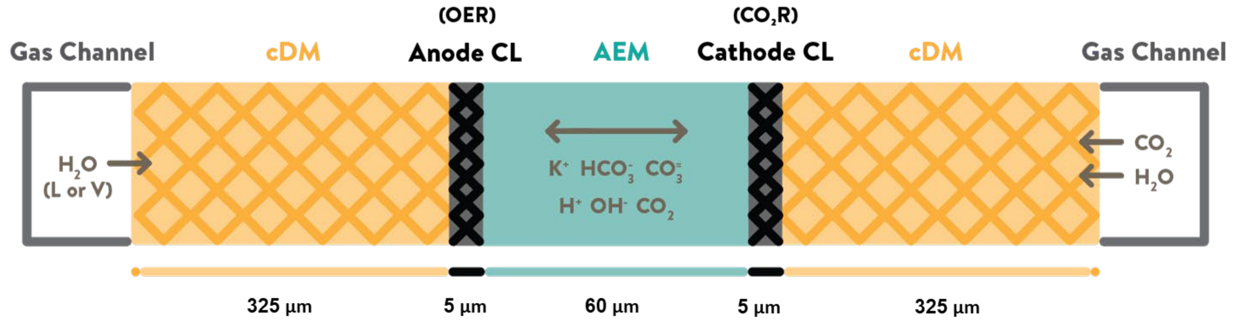

Figure 5.1 Schematic of the Cu-MEA system.

The boundary conditions are summarized in **Table 5.1**. ϕ_S is referenced to the potential at the cathode CH|DM boundary, and set to the applied cell potential at the anode CH|DM boundary. p_G is set to 1 atm at the two gas channels. The boundary condition for p_L at the anode depends on whether the anode feed is humidified gas or liquid water. If it is a liquid feed, $p_L = p_G$ must be satisfied at the CH|DM boundary. If it is a gas feed and $p_L \leq p_G$ at the CH|DM boundary, then a no-flux condition is applied. Pressure inequality is maintained by surface tension in the GDE porous media. Once $p_{\mathrm{L}} > p_{\mathrm{G}}$, there will be an outward flux of liquid water with a mass-transfer coefficient $k'_{\mathrm{MT}} = 1\ \mathrm{kg/m^2s}$ set to an arbitrarily high value to maintain pressure balance of $p_{\mathrm{G}} = p_{\mathrm{L}}$ at the CH|DM boundary.[57] A fixed mass fraction is assumed at both the anode and cathode CH|DM boundaries, with feed compositions set to 100% RH N_2 and 100% RH CO_2, respectively. This corresponds to 3 mol% H_2O at 298 K and 43 mol% H_2O at 350 K. The temperature is set to the operating temperature, T_0, at the two CH|DM boundaries for gas feed conditions.

Table 5.1 Summary of boundary conditions

<table>
<tr><th></th><th>Anode CH|DM</th><th>Cathode CH|DM</th></tr>
<tr><td>ϕ_S</td><td>$\phi_{\mathrm{S}} = V_{\mathrm{cell}}$</td><td>$\phi_{\mathrm{S}} = 0\ \mathrm{V}$</td></tr>
<tr><td>p_G</td><td colspan="2">$p_{\mathrm{G}} = 1\ \mathrm{atm}$</td></tr>
<tr><td rowspan="2">p_L</td><td colspan="2">$\mathbf{n}\cdot\rho_{\mathrm{L}}\mathbf{u}_{\mathrm{L}} = k'_{\mathrm{MT}}\frac{p_{\mathrm{L}}-p_{\mathrm{G}}}{1\ \mathrm{Pa}}\mathrm{step}\left(\frac{p_{\mathrm{L}}-p_{\mathrm{G}}}{1\ \mathrm{Pa}}\right)$ (Gas feed)</td></tr>
<tr><td>$p_{\mathrm{L}} = p_{\mathrm{G}}$ (Liquid feed)</td><td>--</td></tr>
<tr><td>ω_i</td><td>$\omega_0 = \frac{p_0^{\mathrm{vap}}}{p_{\mathrm{G}}}\frac{M_0}{M_{\mathrm{A}}}$
$\omega_{\mathrm{N_2}} = 1 - \omega_0$
$\omega_{i\neq 0,\mathrm{N_2}} = 0$</td><td>$\omega_0 = \frac{p_0^{\mathrm{vap}}}{p_{\mathrm{G}}}\frac{M_0}{M_{\mathrm{A}}}$
$\omega_{\mathrm{CO_2}} = 1 - \omega_0$
$\omega_{i\neq 0,\mathrm{CO_2}} = 0$</td></tr>
<tr><td>T</td><td colspan="2">$T = T_0$</td></tr>
</table>

<table>
<tr><th></th><th>Anode DM|CL</th><th>Anode DM|CL</th></tr>
<tr><td>c_j</td><td>$\boldsymbol{\nabla}\cdot\mathbf{N}_j = 0$</td><td>$\boldsymbol{\nabla}\cdot\mathbf{N}_j = 0$</td></tr>
<tr><td>μ_0</td><td>$\boldsymbol{\nabla}\cdot\mathbf{N}_{\mathrm{w}} = 0$</td><td>$\boldsymbol{\nabla}\cdot\mathbf{N}_{\mathrm{w}} = 0$</td></tr>
</table>

Results and Discussion

The product distribution and the overall simulated polarization curve are shown in **Figure 5.2a** and **Figure 5.2b**, respectively. This distribution is what one would expect for a rough Cu surface[66] operated in an MEA system, assuming that the CO_2R kinetics in the CL are identical to those measured in an aqueous electrolyte (specifically $CsHCO_3$). We should note that the exact kinetics in the CL environment are not necessarily the same as that in the aqueous solution due to different ion concentrations, types, etc.;[29, 97] but devoid of any data, we use these kinetics to see how the MEA device operates. In the last section, an alternate set of self-consistent kinetics[6] is used to further show the generality of the trends observed. We choose to use the kinetics for CO_2R on a roughened Cu (rather than a polished one) for the balance of our analysis because we consider such a surface to be a better representation of Cu-MEAs. This choice is also supported by recent experimental studies of Cu-MEAs, which exhibit a low FE for CH_4, a characteristic of rough Cu surfaces.[49-51]

As seen in **Figure 5.2b**, the product distribution is a strong function of the cell potential. Below about 2.5 V, the principal products are H_2, CO, and HCOOH. CO_2R produces $HCOO^-$ but it cannot leave the AEM without converting to HCOOH since it is negatively charged. As the total current density (TCD) increases and OH^- anions are produced in the cCL, the equilibrium between HCOOH and $HCOO^-$ shifts towards $HCOO^-$ in the cCL. Diffusion and migration drive $HCOO^-$ to the aCL where the OH^- concentration is low due to the OER. Therefore, the fraction of HCOOH collected at the cathode side (depicted by the lighter shade of yellow in **Figure 5.2a**) decreases with cell potential and TCD. This conclusion is consistent with observations of Garbardo *et al*.[51] We note, however, that our simulation neglects formate oxidation at the anode, a process that has been reported and warrants further study.[51, 98] For cell potentials above 2.5 V, the distribution of products shifts progressively to form C_2H_4, EtOH, and PrOH owing to the high cathode overpotential and CO_2 concentration in the cCL.

Figure 5.2b shows both the total polarization curve as well as the applied voltage breakdown (AVB) of a fully vapor-fed Cu-MEA operated at feed temperature of 298 K. The AVB is calculated using the equations given in **Appendix C Applied Voltage Breakdown**. The components of the AVB are categorized as thermodynamic, kinetic, transport, and ohmic, and each of these components is discussed in detail below.

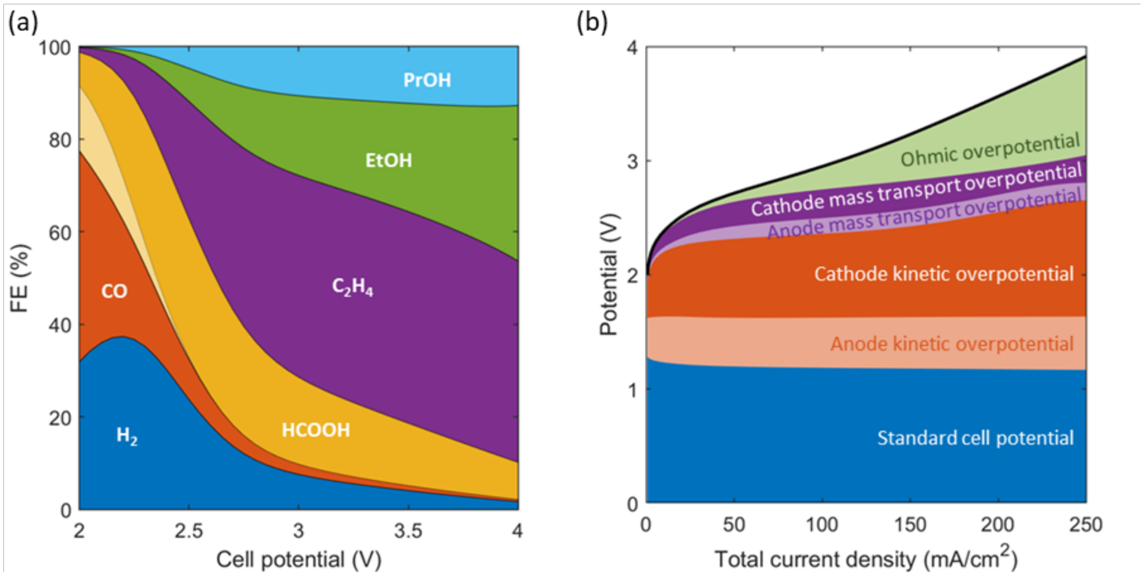

Figure 5.2 (a) The product distribution and (b) the applied-voltage breakdown (AVB) of the base-case Cu-MEA (100% RH N_2 anode feed and 100% RH CO_2 cathode feed at 298 K). The lighter shade of yellow in (a) represents formic acid collected in the cathode chamber.

Standard cell potential

The standard cell potential is the thermodynamic potential required to drive the reactions at the two electrodes. It varies with the TCD to reflect the changes in the distribution of products formed in the cCL. As the FEs for C_2H_4, EtOH, and PrOH increase, the standard cathode potential, U^o_{cathode}, increases because of the higher U^o values of these products, leading to a decrease in the standard cell potential.

Kinetic overpotential

The kinetic overpotential drives the charge transfer reactions at the two electrodes and depends on the catalytic activity of the electrode. Parameters that affect the cathode kinetic overpotential include the cCL thickness, L_{cCL}, and the specific electrocatalyst surface area, a^o_{s}. The simulation shows that increasing L_{cCL} or a^o_{s} has little effect on the cell potential for a given TCD (**Figure 5.3**), suggesting that the Cu-MEA is not limited by overall cathode kinetics.

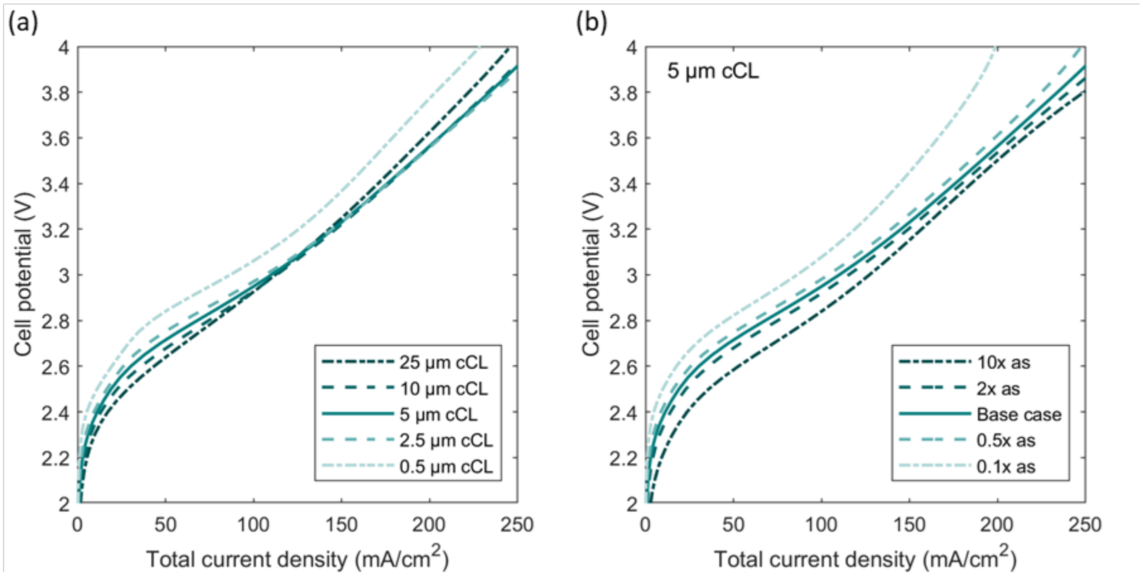

Figure 5.3 Polarization curves for Cu-MEAs simulated with different (a) cCL thicknesses and (b) specific surface areas. Feed composition: 100% RH N_2 anode feed and 100% RH CO_2 cathode feed at 298 K.

While the polarization curve is relatively insensitive to the properties of the cCL, the product distribution is not, as seen in **Figure 5.4** and **Figure 5.5**. Decreasing either the cCL thickness or the specific surface area of the cathode increases the selectivity to C_2H_4, EtOH, and PrOH. This is because a lower catalyst loading leads to a higher cathode kinetic overpotential, which disproportionately promotes the production rates of C_{2+} products over H_2, CO, and $HCOO^-$ due to differences in the transfer coefficients for the various products. C_2H_4, EtOH, and PrOH have larger transfer coefficients, so their reaction rates increase more with higher overpotentials. These relationships allow one to improve the EE for producing C_{2+} products without significant compromise in the total current density, as shown in **Figure 5.6**. We also note a tradeoff in the H_2 FE: at low cell potentials, where the system is more kinetically controlled, decreasing the cCL thickness decreases the TCD more significantly, leading to a lower OH^- concentration in the cCL, thereby increasing the H_2 FE; at high cell potentials, where the TCD change is smaller, a thinner cCL leads to a higher rate of OH^- production per cCL volume via the charge transfer reactions, resulting in a higher OH^- concentration in the cCL and lower HER rates. **Figure 5.4** demonstrates that the thickness of the cCL is a critical parameter for determining the product distribution. The highest FEs for C_{2+} products are achieved with a cCL thickness of 0.5 µm. In this case, the FEs for C_2H_4, EtOH, and PrOH are 48%, 26%, and 15%, respectively, which are reached for a cell potential of 3.2 V and a TCD of 126 mA/cm^2. Increasing the TCD from 130 mA/cm^2 to 230 mA/cm^2 leads to a modest reduction in the C_2H_4 and PrOH FEs, and a rise in EtOH FE. However, since the applied cell potential is also increased, the resulting EEs for C_{2+} products do not improve significantly (**Figure 5.6**).

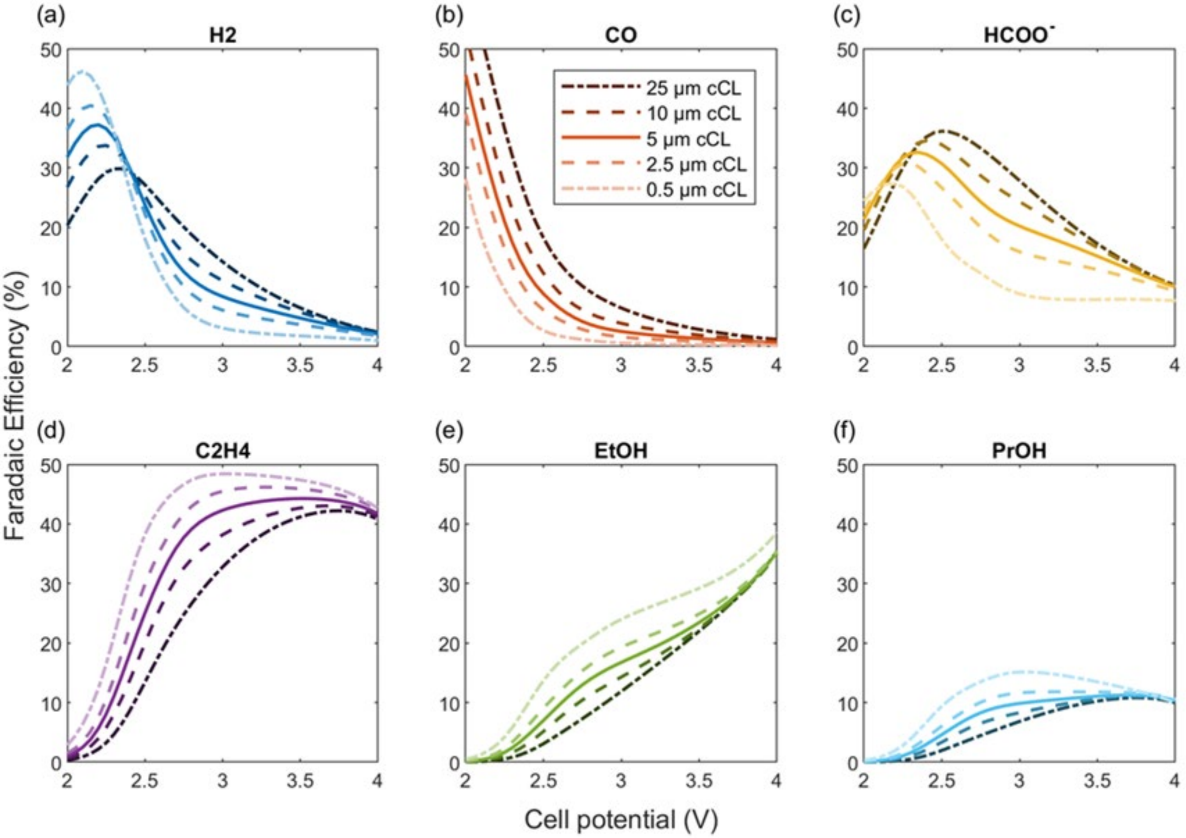

Figure 5.4 The faradaic efficiencies as a function of the cell potential for the six cathode products for Cu-MEAs with a 25 µm, 5 µm, 2.5 µm, and 0.5 µm cCL. Lighter shade represents a thinner cCL. Feed composition: 100% RH N_2 anode feed and 100% RH CO_2 cathode feed at 298 K.

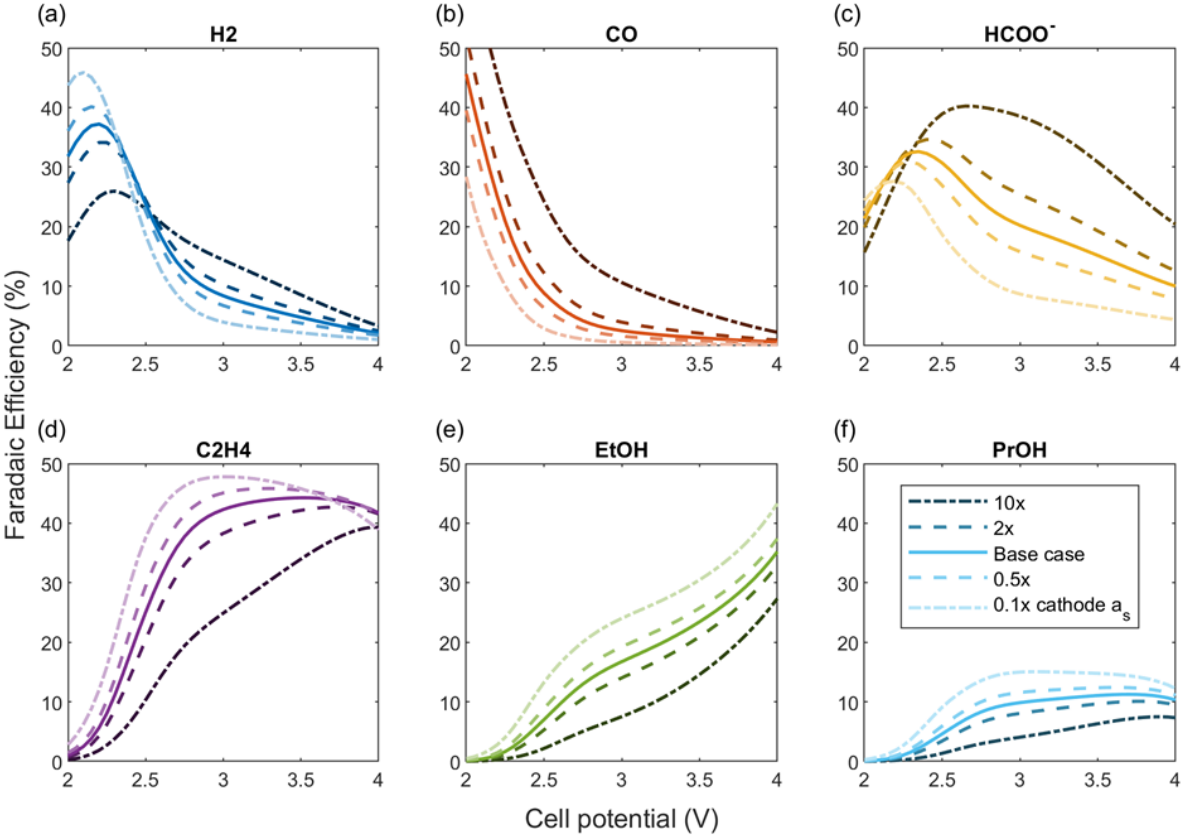

Figure 5.5 The faradaic efficiencies as a function of the cell potential for the six cathode products for Cu-MEAs with varying cCL specific surface areas. Lighter shade represents a lower specific surface area.

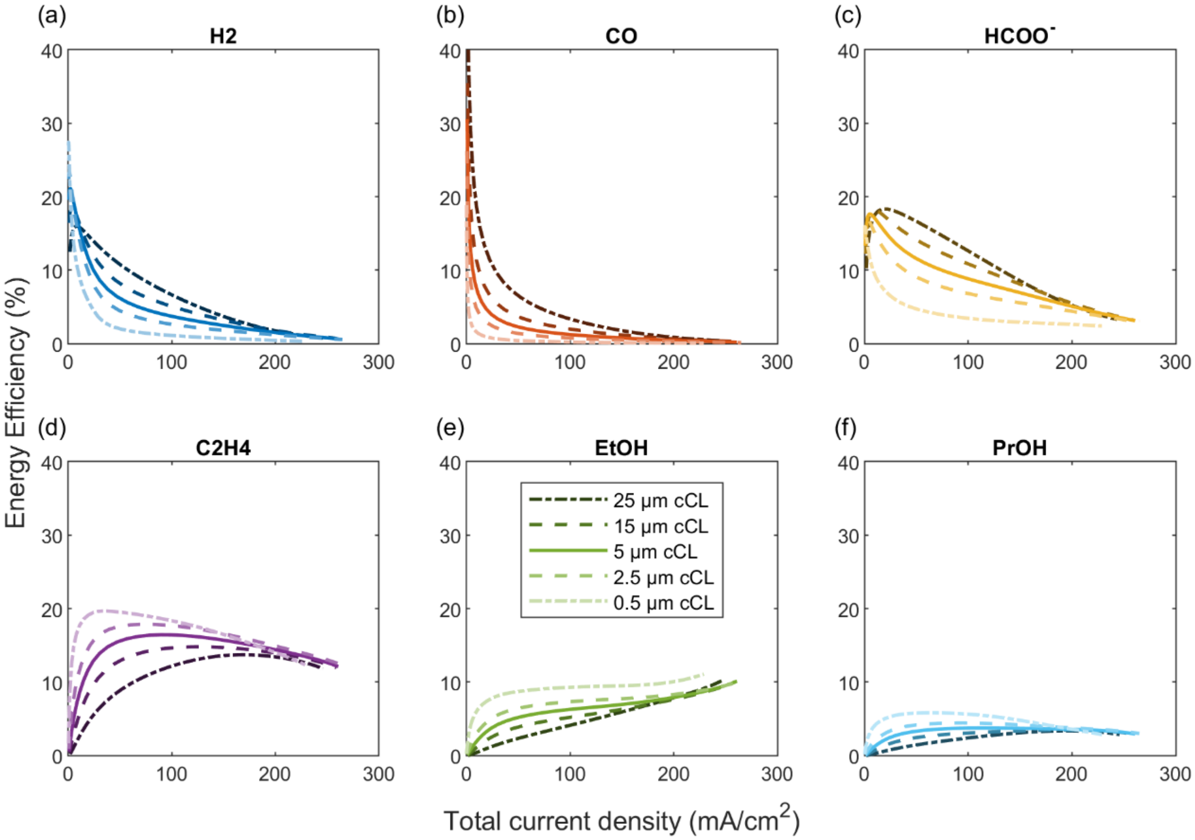

Figure 5.6 The energy efficiencies as a function of the total current density for the six cathode products for Cu-MEAs with a 25 µm, 5 µm, 2.5 µm, and 0.5 µm cCL. Lighter shade represents a thinner cCL.

Changes in the FEs with cCL thickness become less pronounced as the cell potential increases because of the potential gradient that develops in the cCL. **Figure 5.7a** clearly shows that the cathode potential becomes increasingly non-uniform as the applied cell potential increases, leading to sharp gradients in the local current density shown in **Figure 5.7b**. The CL region closer to the membrane is significantly more active – a thinner cCL merely removes the portion of the CL that is barely active, minimally affecting the product distribution and overall cell performance. The CL thickness results discussed here are consistent with experimental results by Dinh *et al.*, who observed little TCD dependence on CL thickness above 100 mA/cm^2, but higher C_2H_4 FE and lower H_2 FE between 200 and 300 mA/cm^2 with thinner cCLs.[39]

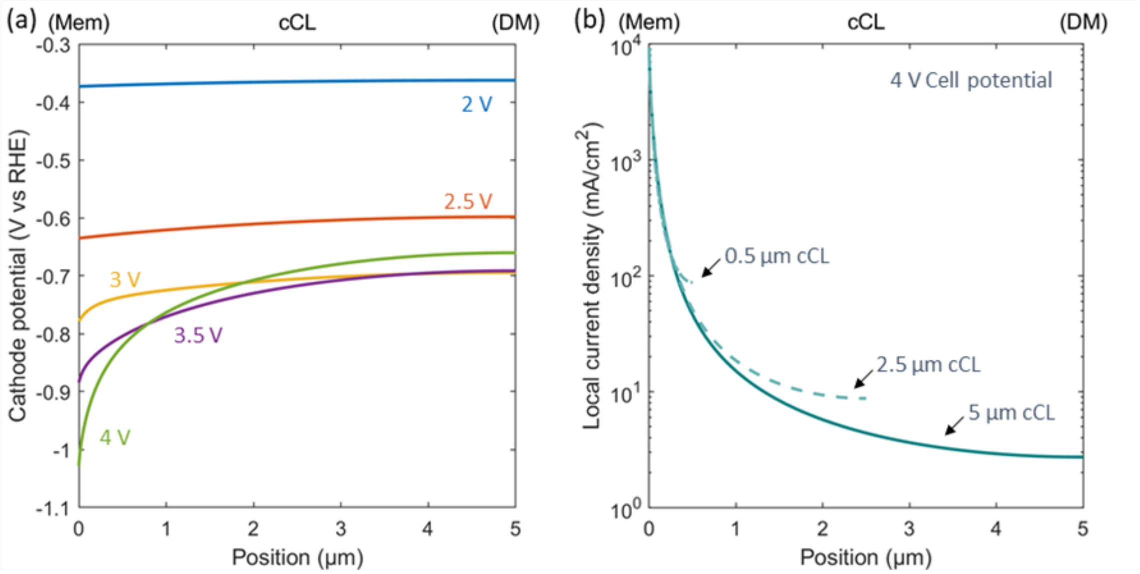

Figure 5.7 (a) The local cathode potential vs RHE in the 5 μm cCL at different cell potentials and (b) the local current-density distribution in the cCL at 4 V cell potential for different cCL thicknesses. The potential gradient developed in the cCL at high cell potentials leads to poor catalyst utilization, where parts of the catalyst close to the membrane (position 0) are much more active than the remaining parts of the cCL.

Mass transport and ohmic overpotential

The mass-transport overpotentials in **Figure 5.2b** mainly arise from deviations in the local OH^- and H_2O concentrations from their initial concentrations, whereas the local CO_2 concentration remains close to saturation in the MEA cCL, as shown in **Figure 5.8**. This behavior is radically different from what happens in aqueous electrolyte systems where H_2O is abundant (55 M) and the supply of CO_2 becomes mass-transfer limited for TCD > 10 mA/cm^2.[99, 100] This observation points to the importance of understanding the dependence of the CO_2R on the activity of water in order to predict and control the CO_2R selectivity in Cu-MEAs. The lower water activity in the cCL at high cell potentials is caused by the consumption of water by the cathode reactions, the electro-osmotic flux of water towards the anode, and the temperature increase in the membrane and CLs. **Figure 5.9** shows that for the case where the feed temperature is 298 K, the cell can heat up by up to 3 K at 250 mA/cm^2 TCD due to the ionic resistivity, heats associated with the reactions, etc. The temperature does not rise as rapidly when the feed temperature is raised to 350 K because of better membrane hydration and ionic conductivity, as discussed below. The higher temperature in the CLs lowers the gas phase RH and membrane hydration, resulting in a higher cell potential at the same TCD compared to an isothermal system (**Figure 5.10a**). These trends are consistent with water-management results under water-vapor electrolysis.[101] In addition to affecting cathode reactions, the low water activity also reduces membrane/ionomer conductivity, leading to an increase in the ohmic overpotential shown in **Figure 5.2b**.

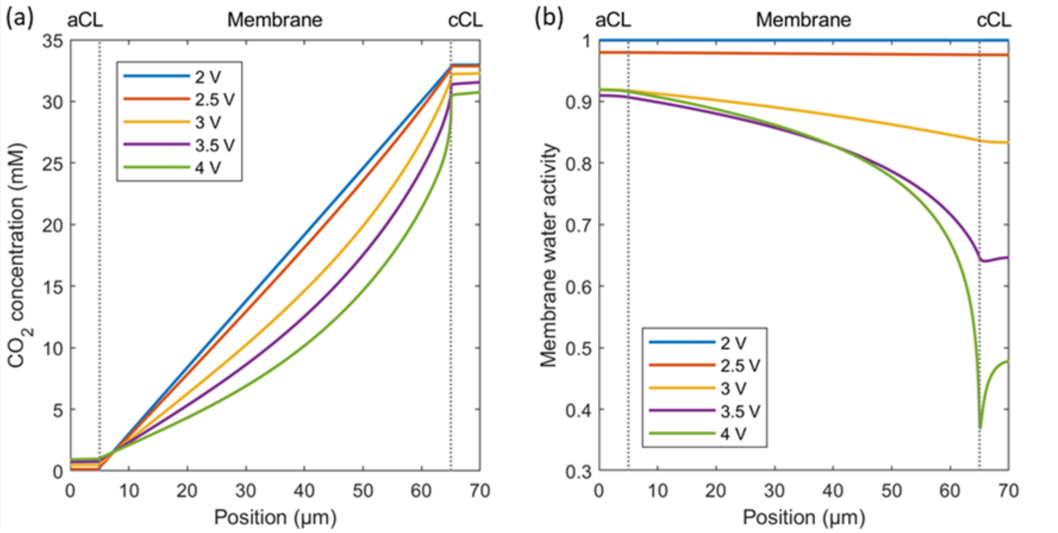

Figure 5.8 (a) CO_2 concentration and (b) water activity profiles in the ionomer electrolyte at different cell potentials. Unlike aqueous systems, CO_2 concentration remains high near the cathode, whereas H_2O becomes depleted at high current densities. Feed composition: 100% RH N_2 anode feed and 100% RH CO_2 cathode feed at 298 K.

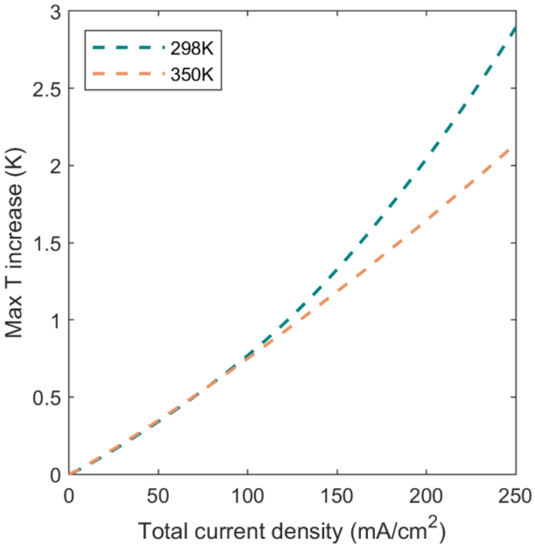

Figure 5.9 Maximum temperature increase in the Cu-MEA cell operated at 298 K (teal) and 350 K (orange). Feed composition: 100% RH N_2 anode feed and 100% RH CO_2 cathode feed.

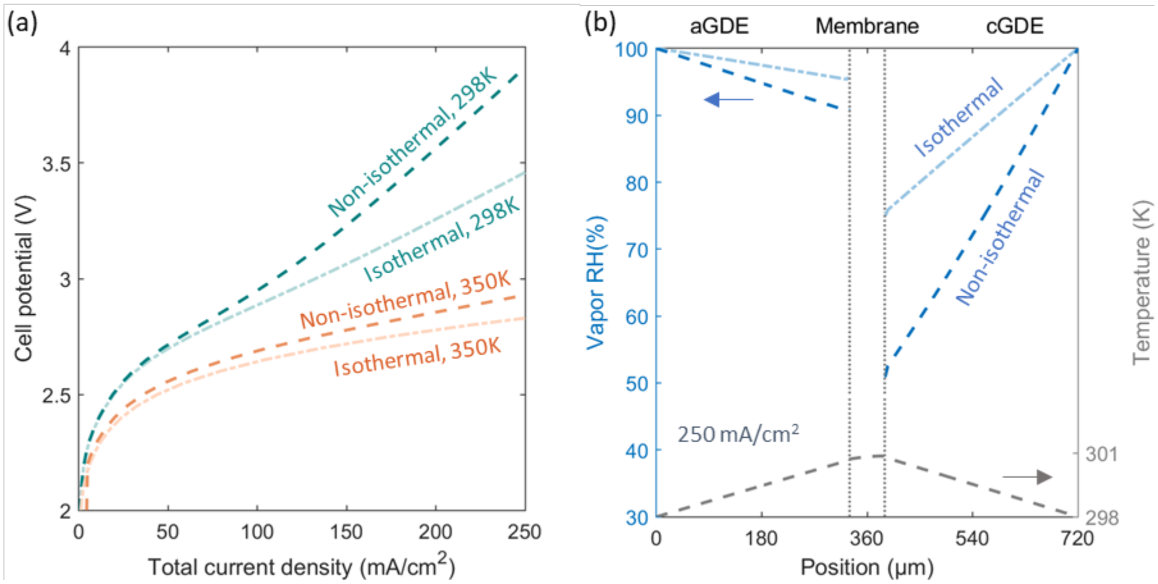

Figure 5.10 (a) Polarization curves at 298 K (teal) and 350 K (orange) simulated with an isothermal (lighter shade, dot-dash) and non-isothermal (dashed) model. (b) The vapor RH and temperature profile at 250 mA/cm^2. Heating due to inefficiencies raises the cell temperature and lowers the RH in the GDEs.

Since water supply and management are critical, we simulated the performance of a Cu-MEA with liquid-water fed to the anode at 298 K and with vapor-water fed to the anode at 350 K. We also studied the impact of a higher EOC. As expected, feeding liquid water instead of water vapor to the anode increases the attainable TCD at a given cell potential, as shown in **Figure 5.11a**. Comparing the AVBs for the liquid-fed (**Figure 5.11b**) and vapor-fed (**Figure 5.2b**) cases, it is clear that the main effect of the liquid-water feed to the anode is to decrease the ohmic overpotential, which is achieved by better hydration of the membrane (**Figure 5.12a**). Interestingly, the larger EOC has opposite effects on the polarization curve for the vapor-anode and liquid-anode cases. A larger EOC increases the electro-osmotic flux of water from the cathode to the anode at the same TCD, hydrating the aCL but dehydrating the cCL. As the membrane/ionomer conductivity exhibit an exponential dependence on water activity,[81] this redistribution of water due to the higher EOC improves the overall ionomer electrolyte conductivity for the vapor-anode case. However, since the aCL is already equilibrated with liquid water in the liquid-fed anode case, cCL dehydration has a larger impact on the overall conductivity.

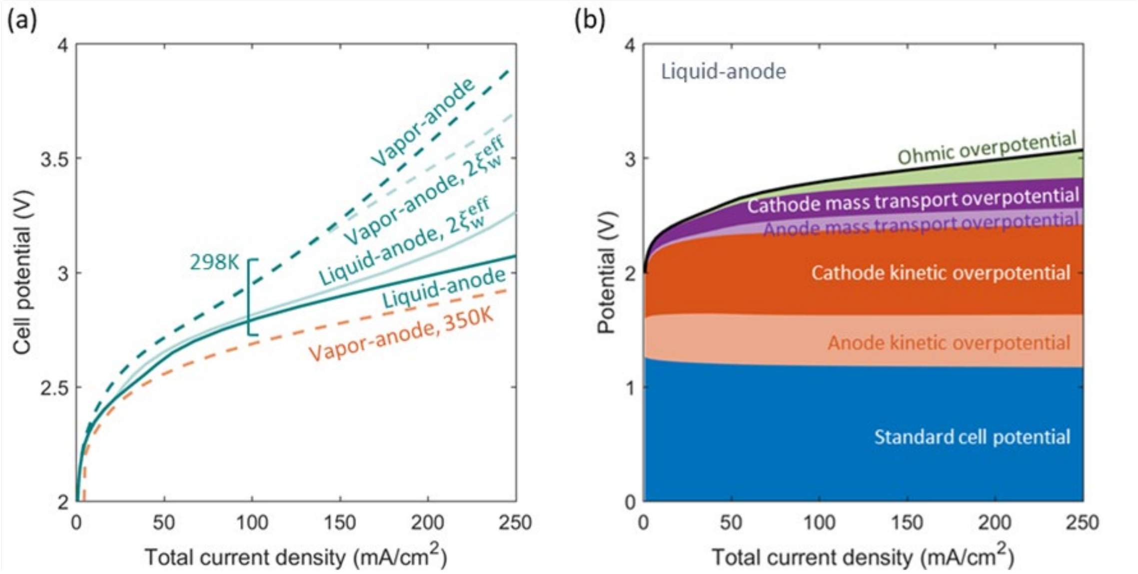

Figure 5.11 (a) Polarization curves for the vapor-water anode feed (dashed) and liquid-water anode feed (solid) Cu-MEAs at 298 K (teal) and 350 K (orange). Lighter shade represents simulation with 2x EOC. Feed composition: 100% RH CO_2 cathode feed for all cases. (b)The AVB for the liquid-anode case at 298 K.

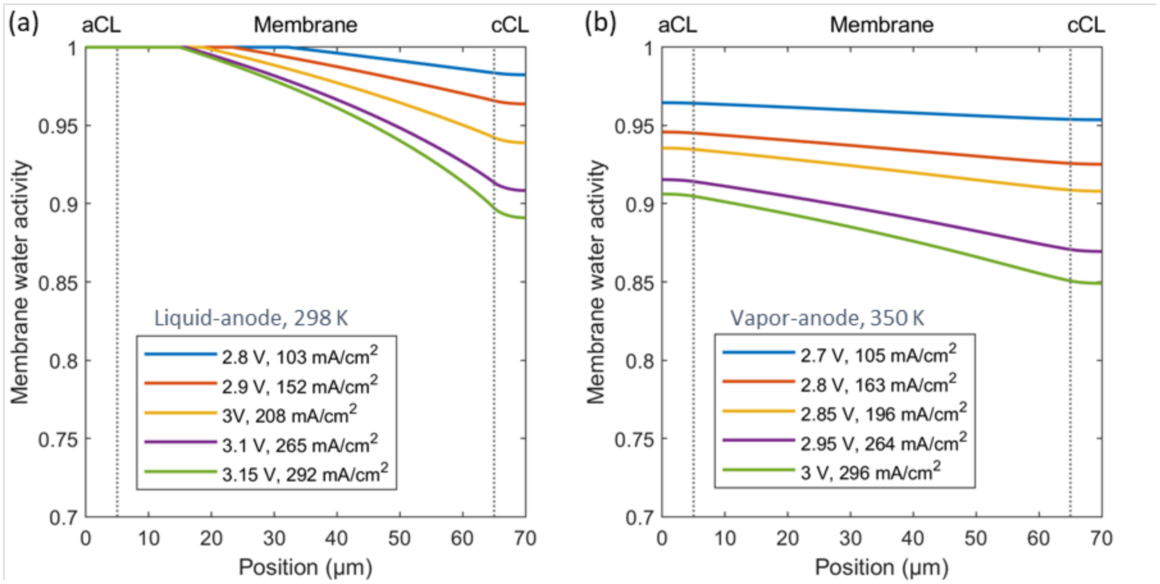

Figure 5.12 Membrane water activity profile for (a) liquid-fed anode at 298 K and (b) vapor-fed anode at 350 K.

One challenge with the liquid-fed anode arrangement is that liquid water can readily permeate the membrane and flood the cCL; this occurs at low TCDs (**Figure 5.13**), and has also been observed experimentally.[98] Cathode flooding blocks CO_2 access to the catalyst in the cCL, resulting in a higher H_2 FE (**Figure 5.14**).[33] As the TCD increases, both the rate of water consumption in the cCL and the electro-osmotic flux of water from cathode to anode increases, returning cCL saturation to its irreducible value. We also observe that liquid water is removed from the cCL more rapidly for the membrane with a higher EOC (**Figure 5.13**). These simulations demonstrate the complexities of water management within these systems and provide guidance for accurate design tradeoffs.

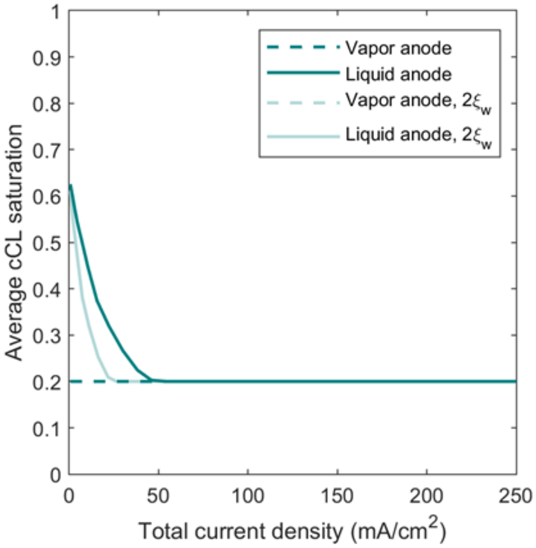

Figure 5.13 The average cCL saturation for vapor-water anode feed (dashed) and liquid-water anode feed (solid) Cu-MEAs at 298 K. Lighter shade represents simulation with 2x EOC.

Another way to increase the water supply to the system is to raise the operating temperature. A 100% RH gas stream contains 3 mol% H_2O at 298 K and 43 mol% H_2O at 350 K. A higher temperature also enhances reaction kinetics and improves various transport properties,[81] but lowers the CO_2 concentration in the supply and its solubility in the membrane.[102] We examined these tradeoffs by simulating the vapor-fed Cu-MEA at 350 K. An even lower cell potential is required to obtain the same TCD at 350 K than feeding liquid water at 298 K (**Figure 5.11a**). Increasing the temperature significantly decreases the ohmic and mass-transport overpotentials because of improved membrane hydration and transport properties. Even at a cell potential of 3 V, which corresponds to a TCD of 300 mA/cm^2, the water activity in the membrane is maintained above 0.85 for the vapor-fed Cu-MEA at 350 K (**Figure 5.12b**). As a result of both the increased temperature and hydration, the membrane maintains a higher conductivity, and therefore, a lower ohmic overpotential at 350 K. Higher membrane conductivity also means higher diffusivities for the ionic species, resulting in a smaller OH^- concentration gradient across the cell, thereby decreasing the mass-transport overpotential.

The improved transport properties at 350 K also lead to a lower OH^- concentration in the cCL, and a higher H_2 FE (**Figure 5.14a**). The observed changes in the FEs for CO_2R products are due to multiple factors: (1) CO_2 solubility in the ionomer decreases with increasing temperature, as does the concentration of CO_2 in the humidified cathode gas feed as noted above. (2) Products with a higher activation energy (i.e. C_2H_4, EtOH, PrOH) are more sensitive to the operating temperature. (3) Increasing membrane hydration with increasing temperature leads to changes in the cathode overpotential at the same cell potential; a higher cathode overpotential benefits products with a higher transfer coefficient, as discussed above. Overall, increasing the temperature enhances the selectivities to EtOH and PrOH because of their relatively lower reaction order with respect to CO_2, higher activation energy, and higher transfer coefficient compared to the other cathode products. On the other hand, the increase in the production rates of CO, $HCOO^-$, and C_2H_4 at 350 K is not as significant compared to EtOH and PrOH, so we observe a drop in their FEs.

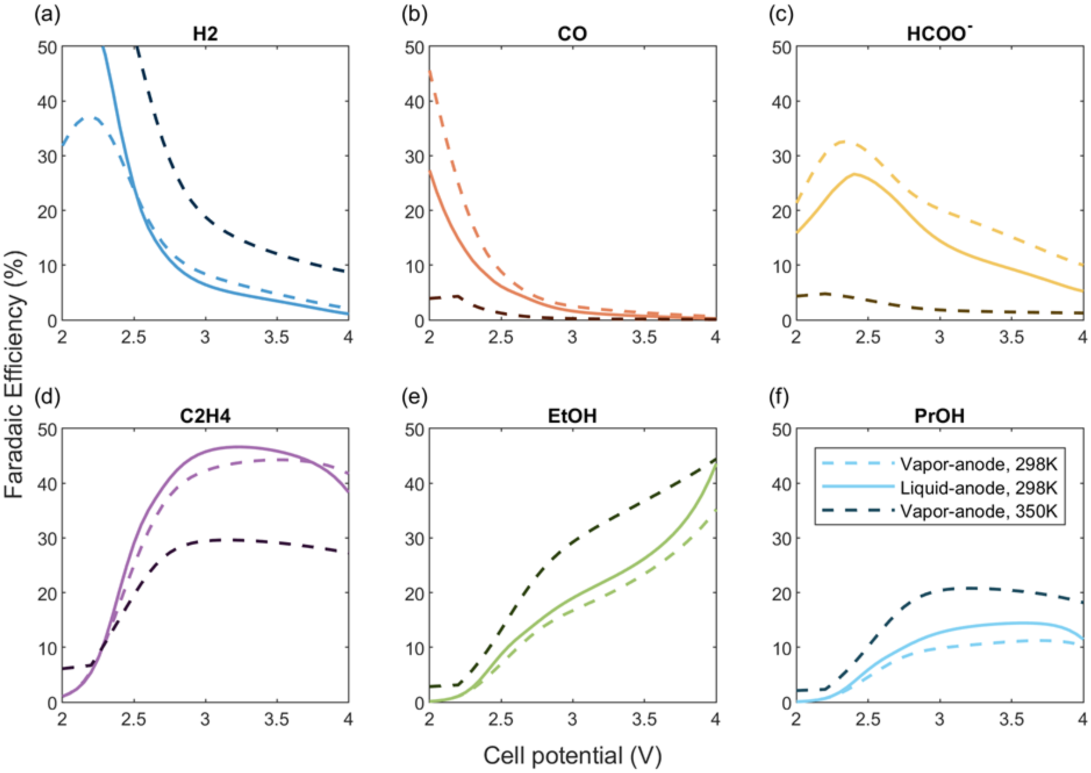

Figure 5.14 The faradaic efficiencies of the six cathode products for vapor-water anode feed (dashed) and liquid-water anode feed (solid) Cu-MEAs at 298 K (lighter shade) and 350 K (dark gray).

Generalizing the findings

As mentioned above, a single set of self-consistent kinetics derived from aqueous experiments was used in all the above simulations. To demonstrate that the findings are general, we performed simulations using a second set of experimentally derived kinetics, knowing that a complete set of kinetics in MEA environments with Cu nanoparticles remain elusive. Furthermore, to demonstrate the impact of moving from an aqueous system to an MEA architecture, the differences between the FEs obtained from simulation of the Cu-MEA and the aqueous analog for both sets of kinetics (a rough Cu surface operated in 0.1 M $CsHCO_3$ and a polished Cu surface operated in 0.1 M $KHCO_3$) are given in **Figure 5.15**. This comparison at different cathode potentials allows one to generalize the above findings and help deconvolute the specific kinetics with the influence of the MEA architecture. The cathode potential for the MEA system is chosen to be the potential at the membrane|cCL interface, where the catalyst is most active (**Figure 5.7**). It is important to note that the potential gradient in the cCL also affects the overall product distribution and contributes to the changes observed in **Figure 5.15**. We observe that the MEA architecture suppresses the formation of H_2 and CO and promotes the formation of C_{2+} products, irrespective of which set of kinetics is used. These trends are a consequence of the higher OH^- and CO_2 concentrations in the cCL and consistent for both sets of kinetic parameters. Interestingly, the second set of kinetics shows that the MEA promotes a greater shift towards EtOH with a stronger dependence on applied potential compared to first set, a result of the larger EtOH transfer coefficient obtained from kinetics II. The analysis emphasizes the need to characterize CO_2R catalysts under vapor-fed conditions and better understand the impacts of the different local environments created by the ionomer electrolyte.

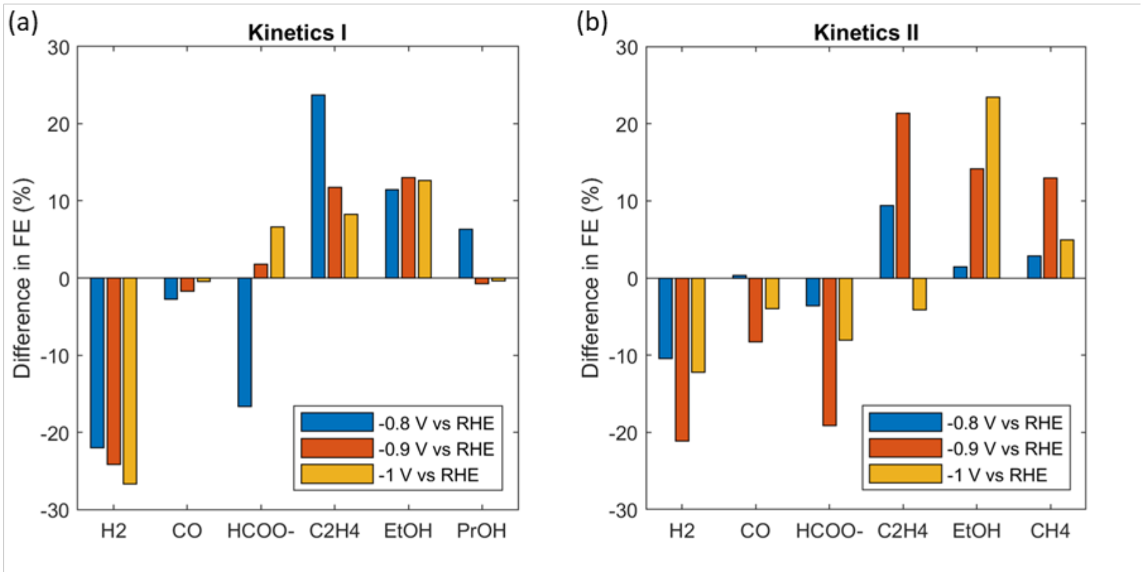

Figure 5.15 The percentage point difference in the FEs predicted for the vapor-fed Cu-MEA and the experimentally measured FEs. The Cu-MEA was simulated with rate parameters extracted from two sets of experimental results derived from (a) reference[66], and (b) reference[6]. The cathode potential for the MEA system is taken to be the potential at the membrane|cCL interface.

Summary

We have developed a multiphysics model to study the performance and limitations of CO_2R on Cu in an MEA configuration. The model demonstrates that the cCL thickness and specific surface area have a much smaller impact on the TCD than the product distribution at a given cell potential. Decreasing catalyst loading shifts the selectivity towards C_{2+} products, namely C_2H_4, EtOH, and PrOH. This effect is less pronounced at high cell potentials because of the sharp gradient in potential that develops in the cCL at high TCDs, an effect that limits catalyst utilization. Examination of the voltage losses due to mass-transport and membrane resistance reveals that

Cu-MEAs suffer from limitation in anion transport through the ionomer and membrane caused by inadequate hydration. These limitations can be overcome by feeding liquid water to the anode or increasing the operating temperature for a fully vapor system. Liquid water readily hydrates the membrane but can lead to flooding of the cCL at low current densities, thereby causing poor mass transport of CO_2 to the catalyst in the cCL. Increasing the operating temperature increases ionomer hydration as well as the rates of products with higher activation energies (e.g., C_2H_4, EtOH, PrOH). However, a higher temperature results in a lower CO_2 concentration in the ionomer (due to both the higher mole fraction of inlet H_2O vapor and a lower CO_2 solubility). These tradeoffs eventually lead to a lower FE for C_2H_4 but higher FEs for EtOH and PrOH at higher temperatures. Finally, we note that the kinetics used in our simulations are based on those observed for CO_2R in an aqueous solution of $CsHCO_3$, and hence, do not account for the specific microenvironment effects on the Cu kinetics related to the ionomer surrounding the Cu nanoparticles in the CL. Since we show that the intrinsic rate parameter for CO_2R are important for defining the product distribution, further work is needed to define the influence of the ionomer on these parameters and to measure them experimentally for an MEA CL. Notwithstanding this limitation, the present simulations are highly informative and demonstrate how the properties of a Cu-MEA and its mode of operation impact the utilization of the applied voltage for promoting CO_2R. This work also emphasizes the critical role of ionomer and membrane hydration on the distribution of products formed by CO_2R.

Chapter 6 Conclusion and Outlook

The performance of vapor-fed CO_2 electrolyzers was explored through multiphysics modeling in this dissertation. Emphasis was placed on quantifying changes between aqueous and vapor systems, and extrapolating learnings from aqueous cells to characterize and optimize vapor-fed device operation. The thin ionomer layer in GDEs were found to improve both the reaction rate and selectivity of CO_2R by decreasing the diffusion length of dissolved CO_2 and allowing CO_2R to occur in more alkaline environments than those allowed by aqueous systems. The higher OH^- and CO_2 concentrations near the GDE catalyst quantified through simulation are hypothesized to suppress the competing HER and promote C-C coupling on copper electrodes, as observed experimentally.[24, 39, 67]

Evident from both simulation results discussed herein and recent experimental observations,[49-51] MEAs are ideal for practical CO_2R operation as they enable the attainment of high current densities with good selectivity to value-added products at relatively low power inputs. Modeling results also reveal intrinsic limitations related to water management, salt precipitation (when operated with an exchange solution), and CO_2 utilization for AEM-based systems. Potential losses due to thermodynamics, kinetics, and mass transport were deconvoluted and quantified through an AVB and systematically studied.

Ohmic losses were found to be the dominate source of inefficiency for a fully-vapor MEA operated at ambient temperature due to limited supply of water. Water supply can be increased by feeding aqueous electrolyte to the anode; the aqueous electrolyte (or exchange solution) also serves to maintain ion concentration in the anode CL and minimizing anode Nernstian losses, but can lead to salt precipitation in the cathode CL at high current densities (the current density at which salt precipitates depends on the concentration of the exchange solution, membrane thickness, etc.). Feeding liquid water to the anode instead of an exchange solution overcomes the salt-precipitation issue but forgoes the ion-regulation effect. An aqueous anode feed can also result in flooding of the cathode CL, which partially blocks CO_2 access to active sites and leads to a higher H_2 FE. Water supply can also be increased by operating the fully-vapor system at an elevated temperature. Doing so will also affect the product distribution of Cu-MEAs, potentially favoring the selectivities of products with higher activation energies. Sensitivity analysis of the cathode GDE properties shows that cathode loading has little effect on the TCD above 100 mA/cm^2 due to low utilization. However, the product distribution is affected and a lower loading favors products with a larger transfer coefficient. The deconvolution of these intricate chemical and physical interrelations through modeling provides insights to the development and optimization of next-generation CO_2 electrolyzers.

While the current model encompasses many of the critical phenomena occurring in the electrochemical cell, further improvement of the model is necessary. In terms of the transport model, Nernst-Planck equation was used to describe species transport in the membrane, even though the system is not necessarily under dilute conditions. Commonly, concentrated-solution transport theory (e.g. Stefan-Maxwell) is used to capture interactions that become significant under non-dilute conditions. These interactions are expected to become critical, especially for exchange-MEAs operating near current densities at which salt-precipitation occurs.[103, 104] However, this approach introduces 28 additional degrees of freedom for this system (frictional interactions between six species, water, and membrane). These composition-dependent diffusion coefficients are currently limited, especially in an AEM environment. More work is needed to measure/predict these frictional forces such that concentration-solution theory can be used without considerably increasing the uncertainty and complexity of the current numerical model.

In terms of the kinetic model, rate parameters extracted from aqueous electrolyte solutions were used throughout, even though catalysts in GDEs are in direct contact with an anion-exchange ionomer. How the anion-exchange ionomer interacts with the CO_2R catalysts and affects CO_2R kinetics is currently not well understood; measurements of these parameters are crucial for predicting the product distribution accurately. Microkinetic models are well-suited for capturing the complex mechanism of CO_2R and how the dominate reaction pathway may change with the varying local CO_2 and OH^- concentrations, temperature, and microenvironment created by the electrolyte.[105-109] Incorporation of CO_2R microkinetics to the current model is worthy of further exploration, and may be used to study different designs and operating modes such as tandem-catalyst electrodes[110-113] and CO_2-CO cofeeds.[114]

Lastly, investigations into overcoming CO_2 pumping effects are warranted, as indicated from simulation results presented herein and recent experimental measurements.[92, 93, 115, 116] Novel membrane and cell designs are needed, such as ionomer membranes that suppresses CO_2/OH^- reaction or creates thermodynamically unfavorable environments for the formation of HCO_3^-.[74, 90] Bipolar membranes also hold promise for blocking $HCO_3^-/CO_3^=$ transport across the membrane to the anode CL by moving the acid|alkaline interface (where CO_2 is released) closer to the cathode CL (where CO_2 is consumed).[93] Both experimental and theoretical studies of these novel designs are vital in the progress towards practical CO_2 electrolyzers.

References

1. O. S. Bushuyev, P. De Luna, C. T. Dinh, L. Tao, G. Saur, J. van de Lagemaat, S. O. Kelley and E. H. Sargent, *Joule*, 2018, **2**, 825-832.
2. J. W. Ager and A. A. Lapkin, *Science*, 2018, **360**, 707-708.
3. P. De Luna, C. Hahn, D. Higgins, S. A. Jaffer, T. F. Jaramillo and E. H. Sargent, *Science*, 2019, **364**, 350.
4. Y. Y. Birdja, E. Perez-Gallent, M. C. Figueiredo, A. J. Gottle, F. Calle-Vallejo and M. T. M. Koper, *Nat Energy*, 2019, **4**, 732-745.
5. T. Hatsukade, K. P. Kuhl, E. R. Cave, D. N. Abram and T. F. Jaramillo, *Phys. Chem. Chem. Phys.*, 2014, **16**, 13814-13819.
6. K. P. Kuhl, E. R. Cave, D. N. Abram and T. F. Jaramillo, *Energy Environ. Sci.*, 2012, **5**, 7050-7059.
7. S. Zhu, B. Jiang, W. B. Cai and M. Shao, *J. Am. Chem. Soc.*, 2017, **139**, 15664-15667.
8. D. Hursan and C. Janaky, *ACS Energy Lett.*, 2018, **3**, 722-723.
9. S. Nitopi, E. Bertheussen, S. B. Scott, X. Y. Liu, A. K. Engstfeld, S. Horch, B. Seger, I. E. L. Stephens, K. Chan, C. Hahn, J. K. Norskov, T. F. Jaramillo and I. Chorkendorff, *Chem. Rev.*, 2019, **119**, 7610-7672.
10. N. Gupta, M. Gattrell and B. MacDougall, *J. Appl. Electrochem.*, 2006, **36**, 161-172.
11. M. R. Singh, E. L. Clark and A. T. Bell, *Phys. Chem. Chem. Phys.*, 2015, **17**, 18924-18936.
12. E. L. Clark, J. Resasco, A. Landers, J. Lin, L.-T. Chung, A. Walton, C. Hahn, T. F. Jaramillo and A. T. Bell, *ACS Catal.*, 2018, DOI: 10.1021/acscatal.8b01340, 6560-6570.
13. H. Hashiba, L. C. Weng, Y. K. Chen, H. K. Sato, S. Yotsuhashi, C. X. Xiang and A. Z. Weber, *J. Phys. Chem. C*, 2018, **122**, 3719-3726.
14. H. Hashiba, S. Yotsuhashi, M. Deguchi and Y. Yamada, *ACS Comb Sci*, 2016, **18**, 203-208.
15. Y. Hori, in *Modern Aspects of Electrochemistry*, eds. C. G. Vayenas, R. E. White and M. E. Gamboa-Aldeco, Springer New York, New York, NY, 2008, DOI: 10.1007/978-0-387-49489-0_3, pp. 89-189.
16. S. Verma, B. Kim, H. R. Jhong, S. Ma and P. J. Kenis, *ChemSusChem*, 2016, **9**, 1972-1979.
17. T. Burdyny and W. A. Smith, *Energy Environ. Sci.*, 2019, DOI: 10.1039/c8ee03134g.
18. M. Jouny, W. Luc and F. Jiao, *Ind Eng Chem Res*, 2018, **57**, 2165-2177.
19. K. Ogura, R. Oohara and Y. Kudo, *J. Electrochem. Soc.*, 2005, **152**, D213-D219.
20. D. T. Whipple, E. C. Finke and P. J. A. Kenis, *Electrochem. Solid-State Lett.*, 2010, **13**, D109-D111.
21. B. Kim, F. Hillman, M. Ariyoshi, S. Fujikawa and P. J. A. Kenis, *J. Power Sources*, 2016, **312**, 192-198.
22. B. Kim, S. Ma, H.-R. Molly Jhong and P. J. A. Kenis, *Electrochim. Acta*, 2015, **166**, 271-276.
23. S. Ma, R. Luo, S. Moniri, Y. C. Lan and P. J. A. Kenis, *J. Electrochem. Soc.*, 2014, **161**, F1124-F1131.
24. S. Verma, X. Lu, S. Ma, R. I. Masel and P. J. Kenis, *Phys. Chem. Chem. Phys.*, 2016, **18**, 7075-7084.
25. D. Higgins, C. Hahn, C. X. Xiang, T. F. Jaramillo and A. Z. Weber, *ACS Energy Lett.*, 2019, **4**, 317-324.
26. A. Z. Weber, *J. Power Sources*, 2010, **195**, 5292-5304.

27. R. L. Cook, R. C. Macduff and A. F. Sammells, *J. Electrochem. Soc.*, 1990, **137**, 607-608.
28. M. R. Singh, Y. Kwon, Y. Lum, J. W. Ager, 3rd and A. T. Bell, *J. Am. Chem. Soc.*, 2016, **138**, 13006-13012.
29. J. Resasco, L. D. Chen, E. Clark, C. Tsai, C. Hahn, T. F. Jaramillo, K. Chan and A. T. Bell, *J. Am. Chem. Soc.*, 2017, **139**, 11277-11287.
30. J. J. Wu, P. P. Sharma, B. H. Harris and X. D. Zhou, *J. Power Sources*, 2014, **258**, 189-194.
31. Q. N. Wang, H. Dong, H. Yu and H. B. Yu, *J. Power Sources*, 2015, **279**, 1-5.
32. B. Endrodi, G. Bencsik, F. Darvas, R. Jones, K. Rajeshwar and C. Janaky, *Prog. Energy Combust. Sci.*, 2017, **62**, 133-154.
33. L. C. Weng, A. T. Bell and A. Z. Weber, *Phys. Chem. Chem. Phys.*, 2018, **20**, 16973-16984.
34. C. C. McCrory, S. Jung, J. C. Peters and T. F. Jaramillo, *J. Am. Chem. Soc.*, 2013, **135**, 16977-16987.
35. B. Endrodi, G. Bencsik, F. Darvas, R. Jones, K. Rajeshwar and C. Janaky, *Progress in Energy and Combustion Science*, 2017, **62**, 133-154.
36. K. Hara and T. Sakata, *Bull. Chem. Soc. Jpn.*, 1997, **70**, 571-576.
37. K. Hara, N. Sonoyama and T. Sakata, *Stud. Surf. Sci. Catal.*, 1998, **114**, 577-580.
38. K. Ogura, H. Yano and F. Shirai, *J. Electrochem. Soc.*, 2003, **150**, D163-D168.
39. C. T. Dinh, T. Burdyny, M. G. Kibria, A. Seifitokaldani, C. M. Gabardo, F. P. G. de Arquer, A. Kiani, J. P. Edwards, P. De Luna, O. S. Bushuyev, C. Q. Zou, R. Quintero-Bermudez, Y. J. Pang, D. Sinton and E. H. Sargent, *Science*, 2018, **360**, 783-787.
40. N. R. d. Tacconi, W. Chanmanee, B. H. Dennis and K. Rajeshwar, *Journal of Material Research*, 2017, **32**, 1727-1734.
41. R. L. Cook, R. C. Macduff and A. F. Sammells, *J. Electrochem. Soc.*, 1988, **135**, 1470-1471.
42. Y. Hori, H. Ito, K. Okano, K. Nagasu and S. Sato, *Electrochim. Acta*, 2003, **48**, 2651-2657.
43. C. Delacourt, P. L. Ridgway, J. B. Kerr and J. Newman, *J. Electrochem. Soc.*, 2008, **155**, B42-B49.
44. D. A. Salvatore, D. M. Weekes, J. He, K. E. Dettelbach, Y. C. Li, T. E. Mallouk and C. P. Berlinguette, *ACS Energy Lett.*, 2017, **3**, 149-154.
45. S. R. Narayanan, B. Haines, J. Soler and T. I. Valdez, *J. Electrochem. Soc.*, 2011, **158**, A167-A173.
46. Y. C. Li, D. Zhou, Z. Yan, R. H. Gonçalves, D. A. Salvatore, C. P. Berlinguette and T. E. Mallouk, *ACS Energy Lett.*, 2016, **1**, 1149-1153.
47. S. M. A. Kriescher, K. Kugler, S. S. Hosseiny, Y. Gendel and M. Wessling, *Electrochem. Commun.*, 2015, **50**, 64-68.
48. G. Wang, J. Pan, S. P. Jiang and H. Yang, *J. CO2 Util.*, 2018, **23**, 152-158.
49. D. S. Ripatti, T. R. Veltman and M. W. Kanan, *Joule*, 2019, **3**, 240-256.
50. I. Sullivan, L. Han, S. H. Lee, M. Lin, D. M. Larson, W. S. Drisdell and C. Xiang, *ACS Sustainable Chemistry & Engineering*, 2019, **7**, 16964-16970.
51. C. M. Gabardo, C. P. O'Brien, J. P. Edwards, C. McCallum, Y. Xu, C. T. Dinh, J. Li, E. H. Sargent and D. Sinton, *Joule*, 2019, **3**, 2777-2791.
52. S. Haussener, C. Xiang, J. M. Spurgeon, S. Ardo, N. S. Lewis and A. Z. Weber, *Energy Environ. Sci.*, 2012, **5**.
53. Y. Chen, N. S. Lewis and C. Xiang, *ACS Energy Lett.*, 2016, **1**, 273-280.

54. A. Z. Weber, R. L. Borup, R. M. Darling, P. K. Das, T. J. Dursch, W. Gu, D. Harvey, A. Kusoglu, S. Litster, M. M. Mench, R. Mukundan, J. P. Owejan, J. G. Pharoah, M. Secanell and I. V. Zenyuk, *J. Electrochem. Soc.*, 2014, **161**, F1254-F1299.
55. C. Xiang, Y. Chen and N. S. Lewis, *Energy Environ. Sci.*, 2013, **6**.
56. C. Xiang, A. Z. Weber, S. Ardo, A. Berger, Y. Chen, R. Coridan, K. T. Fountaine, S. Haussener, S. Hu, R. Liu, N. S. Lewis, M. A. Modestino, M. M. Shaner, M. R. Singh, J. C. Stevens, K. Sun and K. Walczak, *Angew. Chem., Int. Ed.*, 2016, **55**, 12974-12988.
57. I. V. Zenyuk, P. K. Das and A. Z. Weber, *J. Electrochem. Soc.*, 2016, **163**, F691-F703.
58. I. V. Zenyuk, E. Medici, J. Allen and A. Z. Weber, *Int. J. Hydrogen Energy*, 2015, **40**, 16831-16845.
59. C. Delacourt and J. Newman, *J. Electrochem. Soc.*, 2010, **157**, B1911-B1926.
60. K. Wu, E. Birgersson, B. Kim, P. J. A. Kenis and I. A. Karimi, *J. Electrochem. Soc.*, 2014, **162**, F23-F32.
61. J. S. Newman and K. E. Thomas-Alyea, *Electrochemical systems*, J. Wiley, Hoboken, N.J., 3rd edn., 2004.
62. E. Nurlaela, T. Shinagawa, M. Qureshi, D. S. Dhawale and K. Takanabe, *ACS Catal.*, 2016, **6**, 1713-1722.
63. L. Giordano, B. Han, M. Risch, W. T. Hong, R. R. Rao, K. A. Stoerzinger and Y. Shao-Horn, *Catal. Today*, 2016, **262**, 2-10.
64. D. Y. Kuo, J. K. Kawasaki, J. N. Nelson, J. Kloppenburg, G. Hautier, K. M. Shen, D. G. Schlom and J. Suntivich, *J. Am. Chem. Soc.*, 2017, **139**, 3473-3479.
65. T. Schuler, T. Kimura, T. J. Schmidt and F. Buchi, *Submitted*, 2020.
66. M. Ebaid, K. Jiang, Z. Zhang, W. S. Drisdell, A. T. Bell and J. K. Cooper, *Chem. Mater.*, 2020, DOI: 10.1021/acs.chemmater.0c00761.
67. L. Wang, S. A. Nitopi, E. Bertheussen, M. Orazov, C. G. Morales-Guio, X. Liu, D. C. Higgins, K. Chan, J. K. Nørskov, C. Hahn and T. F. Jaramillo, *ACS Catal.*, 2018, **8**, 7445-7454.
68. M. Mukaddam, E. Litwiller and I. Pinnau, *Macromolecules*, 2016, **49**, 280-286.
69. V. A. Sethuraman, S. Khan, J. S. Jur, A. T. Haug and J. W. Weidner, *Electrochim. Acta*, 2009, **54**, 6850-6860.
70. E. Wilhelm, R. Battino and R. J. Wilcock, *Chem. Rev.*, 1977, **77**, 219-262.
71. M. Soniat and F. A. Houle, *J. Phys. Chem. B*, 2018, **122**, 8255-8268.
72. D. T. Hallinan and Y. A. Elabd, *J. Phys. Chem. B*, 2007, **111**, 13221-13230.
73. Q. Zhao, N. Carro, H. Y. Ryu and J. Benziger, *Polymer*, 2012, **53**, 1267-1276.
74. N. Ziv, W. E. Mustain and D. R. Dekel, *ChemSusChem*, 2018, **11**, 1136-1150.
75. A. R. Crothers, R. M. Darling, A. Kusoglu, C. J. Radke and A. Z. Weber, *J. Electrochem. Soc.*, 2020, **167**, 013547.
76. A. R. Crothers, R. M. Darling, A. Kusoglu, C. J. Radke and A. Z. Weber, *J. Electrochem. Soc.*, 2020, **167**, 013548.
77. Y. S. Li, T. S. Zhao and W. W. Yang, *Int. J. Hydrogen Energy*, 2010, **35**, 5656-5665.
78. M. R. Gerhardt, L. M. Pant and A. Z. Weber, *J. Electrochem. Soc.*, 2019, **166**, F3180-F3192.
79. E. N. Fuller, P. D. Schettle and J. C. Giddings, *Ind. Eng. Chem.*, 1966, **58**, 19-+.
80. *CRC handbook of chemistry and physics*, CRC Press, Cleveland, Ohio, 1977.
81. J. Peng, A. L. Roy, S. G. Greenbaum and T. A. Zawodzinski, *J. Power Sources*, 2018, **380**, 64-75.

82. A. Z. Weber and J. Newman, *J. Electrochem. Soc.*, 2004, **151**, A311-A325.
83. F. A. L. Dullien, *Porous media : fluid transport and pore structure*, Academic Press, San Diego, 1992.
84. F. C. Cetinbas, R. K. Ahluwalia, N. Kariuki, V. De Andrade, D. Fongalland, L. Smith, J. Sharman, P. Ferreira, S. Rasouli and D. J. Myers, *J. Power Sources*, 2017, **344**, 62-73.
85. A. Chowdhury, C. J. Radke and A. Z. Weber, *ECS Trans.*, 2017, **80**, 321-333.
86. A. Salehi-Khojin, H.-R. M. Jhong, B. A. Rosen, W. Zhu, S. Ma, P. J. A. Kenis and R. I. Masel, *J. Phys. Chem. C*, 2013, **117**, 1627-1632.
87. S. Thiele, R. Zengerle and C. Ziegler, *Nano Res.*, 2011, **4**, 849-860.
88. T. Soboleva, X. Zhao, K. Malek, Z. Xie, T. Navessin and S. Holdcroft, *ACS Appl. Mater. Interfaces*, 2010, **2**, 375-384.
89. H. Schulenburg, B. Schwanitz, N. Linse, G. n. G. Scherer, A. Wokaun, J. Krbanjevic, R. Grothausmann and I. Manke, *J. Phys. Chem. C*, 2011, **115**, 14236-14243.
90. H. Yanagi and K. Fukuta, *ECS Trans.*, 2008, **16**, 257-262.
91. A. G. Divekar, A. M. Park, Z. R. Owczarczyk, S. Seifert, B. S. Pivovar and A. M. Herring, *ECS Trans.*, 2017, **80**, 1005-1011.
92. Z. C. Liu, H. Z. Yang, R. Kutz and R. I. Masel, *J. Electrochem. Soc.*, 2018, **165**, J3371-J3377.
93. A. Patru, T. Binninger, B. Pribyl and T. J. Schmidt, *J. Electrochem. Soc.*, 2019, **166**, F34-F43.
94. H.-S. Shiau, I. V. Zenyuk and A. Z. Weber, *J Electrochem Soc*, 2017, **164**, E3583-E3591.
95. M. Jouny, W. Luc and F. Jiao, *Nature Catalysis*, 2018, **1**, 748-755.
96. L. C. Weng, A. T. Bell and A. Z. Weber, *Energy Environ. Sci.*, 2019, **12**, 1950-1968.
97. S. Ringe, E. L. Clark, J. Resasco, A. Walton, B. Seger, A. T. Bell and K. Chan, *Energy Environ. Sci.*, 2019, **12**, 3001-3014.
98. G. O. Larrazábal, P. Strøm-Hansen, J. P. Heli, K. Zeiter, K. T. Therkildsen, I. Chorkendorff and B. Seger, *ACS Appl. Mater. Interfaces*, 2019, **11**, 41281-41288.
99. N. Gupta, M. Gattrell and B. MacDougall, *J. Appl. Electrochem.*, 2006, **36**, 161-172.
100. E. L. Clark and A. T. Bell, *J. Am. Chem. Soc.*, 2018, **140**, 7012-7020.
101. J. C. Fornaciari, M. R. Gerhardt, J. Zhou, Y. Regmi, N. Danilovic, A. T. Bell and A. Z. Weber, *Submitted*, 2020.
102. X. M. Ren, T. D. Myles, K. N. Grew and W. K. S. Chiu, *J. Electrochem. Soc.*, 2015, **162**, F1221-F1230.
103. V. M. Ehlinger, A. R. Crothers, A. Kusoglu and A. Z. Weber, *Submitted*, 2020.
104. R. B. Bird, W. E. Stewart and E. N. Lightfoot, *Transport phenomena*, J. Wiley, New York, Rev. 2nd edn., 2007.
105. X. Y. Liu, P. Schlexer, J. P. Xiao, Y. F. Ji, L. Wang, R. B. Sandberg, M. Tang, K. S. Brown, H. J. Peng, S. Ringe, C. Hahn, T. F. Jaramillo, J. K. Norskov and K. R. Chan, *Nat. Commun.*, 2019, **10**.
106. M. R. Singh, J. D. Goodpaster, A. Z. Weber, M. Head-Gordon and A. T. Bell, *P Natl Acad Sci USA*, 2017, **114**, E8812-E8821.
107. A. J. Garza, A. T. Bell and M. Head-Gordon, *ACS Catal.*, 2018, **8**, 1490-1499.
108. T. Cheng, H. Xiao and W. A. Goddard, *P Natl Acad Sci USA*, 2017, **114**, 1795-1800.
109. J. D. Goodpaster, A. T. Bell and M. Head-Gordon, *J. Phys. Chem. Lett.*, 2016, **7**, 1471-1477.
110. Y. Lum and J. W. Ager, *Energy Environ. Sci.*, 2018, **11**, 2935-2944.

111. C. G. Morales-Guio, E. R. Cave, S. A. Nitopi, J. T. Feaster, L. Wang, K. P. Kuhl, A. Jackson, N. C. Johnson, D. N. Abram, T. Hatsukade, C. Hahn and T. F. Jaramillo, *Nature Catalysis*, 2018, **1**, 764-771.
112. Gurudayal, D. Perone, S. Malani, Y. Lum, S. Haussener and J. W. Ager, *Acs Appl Energ Mater*, 2019, **2**, 4551-4559.
113. X. She, T. Zhang, Z. Li, H. Li, H. Xu and J. Wu, *Cell Reports Physical Science*, 2020, **1**, 100051.
114. X. L. Wang, J. F. de Araujo, W. Ju, A. Bagger, H. Schmies, S. Kuhl, J. Rossmeisl and P. Strasser, *Nat Nanotechnol*, 2019, **14**, 1063-+.
115. M. Lin, L. H. Han, M. R. Singh and C. X. Xiang, *Acs Appl Energ Mater*, 2019, **2**, 5843-5850.
116. M. Ma, E. L. Clark, K. T. Therkildsen, S. Dalsgaard, I. Chorkendorff and B. Seger, *Energy Environ. Sci.*, 2020, **13**, 977-985.
117. A. Z. Weber, R. M. Darling and J. Newman, *J. Electrochem. Soc.*, 2004, **151**, A1715-A1727.
118. M. Adachi, T. Navessin, Z. Xie, F. H. Li, S. Tanaka and S. Holdcroft, *J. Membrane Sci.*, 2010, **364**, 183-193.
119. X. H. Wang, J. P. McClure and P. S. Fedkiw, *Electrochim. Acta*, 2012, **79**, 126-132.
120. N. Khajeh-Hosseini-Dalasm, M. J. Kermani, D. G. Moghaddam and J. M. Stockie, *Int. J. Hydrogen Energy*, 2010, **35**, 2417-2427.
121. C. Y. Du, P. F. Shi, X. Q. Cheng and G. P. Yin, *Electrochem. Commun.*, 2004, **6**, 435-440.
122. A. El-Kharouf, T. J. Mason, D. J. L. Brett and B. G. Pollet, *J. Power Sources*, 2012, **218**, 393-404.

Appendix A Boundary Layer Model

Kinetic parameters are extracted from experimental data reported by Ebaid *et al*, where they measured CO_2R on roughened Cu in $CsHCO_3$.[66] Mass transport effects are deconvoluted through simulation of the boundary layer, estimated to be 80 μm.[12] Species molar balance

$$\nabla \cdot \mathbf{N}_j = R_j \tag{A-1}$$

Nernst-Planck,

$$\mathbf{N}_j = -D_j^{\text{eff}} \nabla c_j + \frac{z_j F}{RT} D_j^{\text{eff}} c_j \nabla \phi_{\text{L}} \tag{A-2}$$

and electroneutrality,

$$\sum_i z_i c_i = 0 \tag{A-3}$$

are used to solve for the concentration and electrolyte potential profiles. The flux of each species at the electrode surface are converted from the measured partial current densities using Faraday's law,

$$\mathbf{N}_j = \sum_k -\frac{s_{j,k} i_k}{nF} \tag{A-4}$$

The concentration is set to the bulk concentration at the bulk electrolyte boundary. The exchange current densities were then obtained through fitting the concentration-dependent Tafel equation,

$$i_k = i_{o,k} \prod_j \left(\frac{c_j}{c_j^{\text{ref}}}\right)^{\gamma_{j,k}} \cdot \exp\left(-\frac{\alpha_{\text{c},k} F}{RT} \eta_k\right) \tag{A-5}$$

to the experimentally measured partial current densities. The reaction orders with respect to CO_2 concentration were approximated from data reported by Wang *et al*;[67] the reaction orders with respect to water activity were approximated by considering the number of elementary steps that involve water before obtaining an intermediate with the corresponding number of carbon atoms. This method makes the following assumptions: (1) the surface coverage of intermediates are low such that the fraction of empty sites can be approximated as one; (2) the elementary steps listed in **Table A.1** are at quasi-equilibrium.

To obtain the activation energy, we assume an Arrhenius dependence for the exchange current density,

$$i_{o,k} = n_k e A_0 \exp\left(-\frac{E_{a,k}}{RT}\right) \tag{A-6}$$

where n_k is number of electrons transferred in reaction k, e is the electron charge, and $E_{a,k}$ is the activation energy. We assume a constant preexponential factor, $A_0 = 10^{15}\ \mathrm{s}^{-1}$, for all cathodic reactions, and back calculate $E_{a,k}$ from the exchange current density. The activation energies are listed in **Table A.1**. **Figure A.1** shows how the simulated partial current densities for the aqueous system compare to experimental data.

Table A.1 Estimated activation energy, the Peltier coefficient, and reaction order with respect to water activity

Product	E_a (kJ/mol)	Π_k (mV)	Elementary steps involving water	γ_w
O_2	11 + 1 x pH	240	--	1.6[65]
H_2	9.6 + 1 x pH	13	$\mathrm{H_2O} \rightarrow * \mathrm{H} \xrightarrow{\mathrm{H_2O}} \mathrm{H_2}$	2
CO	20	38	$\mathrm{CO_2} \xrightarrow{\mathrm{H_2O}} * \mathrm{C_1}$	1
HCOO-	35	-104		
C2H4	58	-123	$2 \times \left(\mathrm{CO_2} \xrightarrow{\mathrm{H_2O}} * \mathrm{CO}\right)$ $* \mathrm{CO} \xrightarrow{\mathrm{H_2O}} * \mathrm{CHO}$ $* \mathrm{CHO} + * \mathrm{CO} \rightarrow * \mathrm{C_2}$	3
EtOH	63	-123		
PrOH	67	-135	$3 \times \left(\mathrm{CO_2} \xrightarrow{\mathrm{H_2O}} * \mathrm{CO}\right)$ $* \mathrm{CO} \xrightarrow{\mathrm{H_2O}} * \mathrm{CHO}$ $* \mathrm{CHO} + * \mathrm{CO} \rightarrow * \mathrm{OCCHO}$ $* \mathrm{OCCHO} + * \mathrm{CO} \rightarrow * \mathrm{C_3}$	4

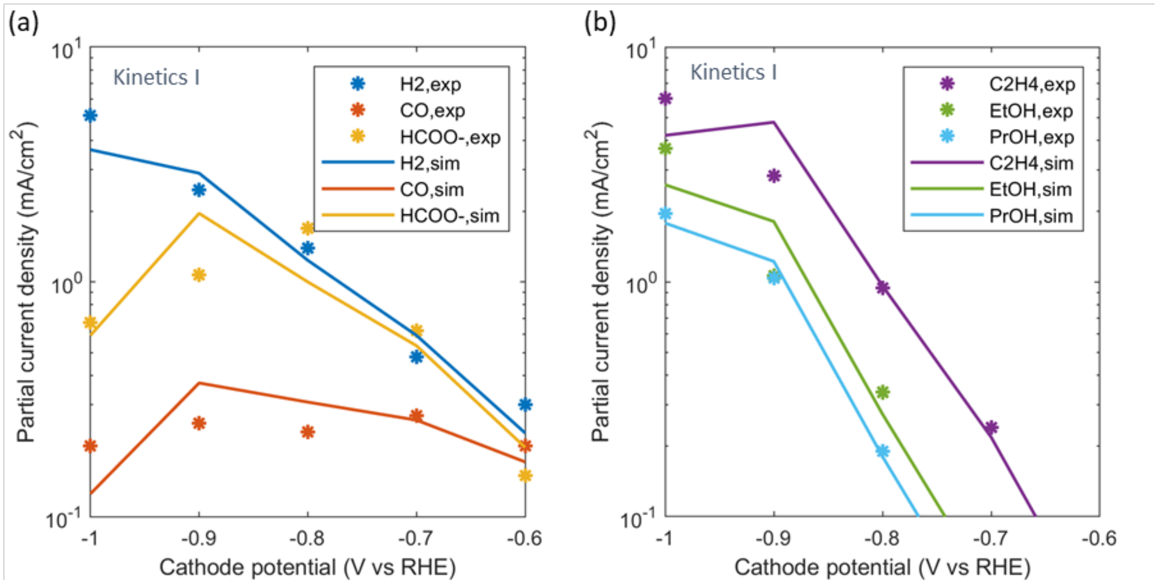

Figure A.1 Comparison between the experimental partial current densities[66] and the simulated partial current densities using the extracted kinetic parameters after correcting for concentration polarization effects assuming an 80-µm boundary-layer thickness.

A second set of self-consistent rate equations was used to assess the impacts of the MEA architecture in Chapter 5. The same process of fitting the equations was used as detailed above to obtain the rate parameters for a second set of self-consistent kinetics,[6, 67] summarized in **Table A.2**. We used two Tafel equations to better fit the H_2 partial current density empirically. The pH dependence for CH_4 was estimated based on the trend observed by Wang *et al*.[67] **Figure A.2** shows how the simulated partial current densities for the aqueous system compare to experimental data.

Table A.2 Rate parameters obtained from measurements by reference[5] (Kinetics II)

	U_k^o (V)	$i_{o,k}$ (mA cm^{-2})	$\alpha_{\mathrm{a/c},k}$	$\prod_j a_j^{\gamma_{j,k}}$	**Ref.**
HER & CO_2R on polished Cu foil					6, 67
H_2 ($\eta < -0.8$ V)	0	$2.2 \times 10^{-8} \exp\left(-\frac{0.01[\mathrm{eV}]\mathrm{pH}}{k_BT}\right)$	0.69	a_w^2	
H_2 ($\eta > -0.8$ V)		$1.7 \exp\left(-\frac{0.01[\mathrm{eV}]\mathrm{pH}}{k_BT}\right)$	0.12	a_w^2	
CO	-0.11	1.1×10^{-4}	0.10	$a_\mathrm{w}\left(\frac{[\mathrm{CO_2}]}{1\ \mathrm{M}}\right)^{1.50}$	
$HCOO^-$	-0.02	5.4×10^{-7}	0.24	$a_\mathrm{w}\left(\frac{[\mathrm{CO_2}]}{1\ \mathrm{M}}\right)^{2.00}$	
C_2H_4	0.07	3.4×10^{-13}	0.69	$a_\mathrm{w}^3\left(\frac{[\mathrm{CO_2}]}{1\ \mathrm{M}}\right)^{1.36}$	
C_2H_5OH	0.08	1.4×10^{-19}	1.10	$a_\mathrm{w}^3\left(\frac{[\mathrm{CO_2}]}{1\ \mathrm{M}}\right)^{0.96}$	
CH_4	0.17	$8.5 \times 10^{-18} \exp\left(-\frac{0.02[\mathrm{eV}]\mathrm{pH}}{k_BT}\right)$	1.13	$a_\mathrm{w}\left(\frac{[\mathrm{CO_2}]}{1\ \mathrm{M}}\right)^{0.84}$	

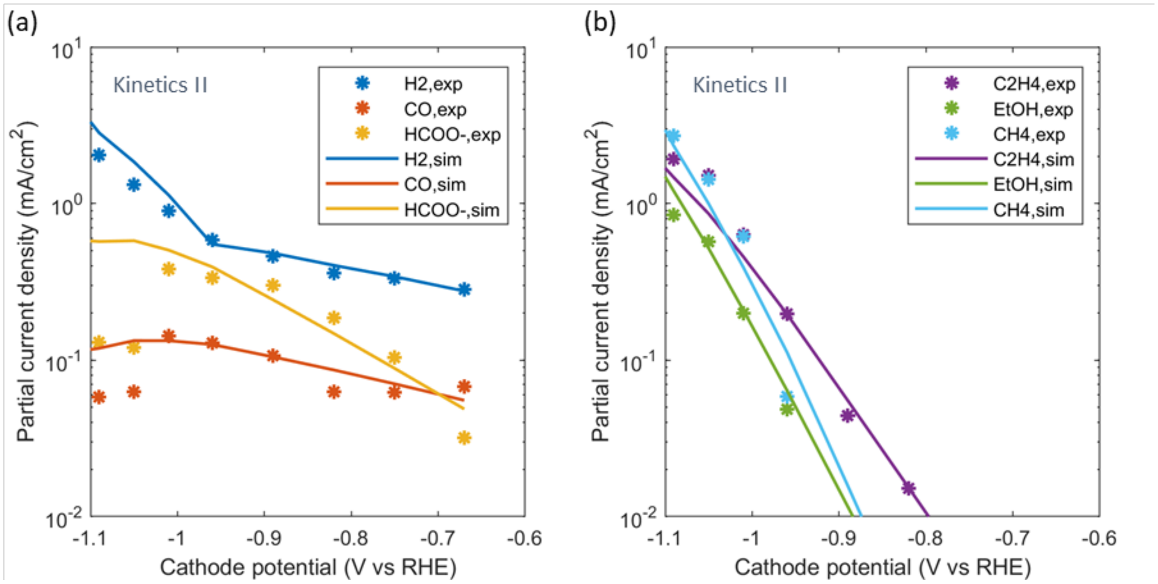

Figure A.2 Comparison between the experimental partial current densities[6] and the simulated partial current densities using the extracted kinetic parameters after correcting for concentration polarization effects assuming an 80-μm boundary-layer thickness.

Appendix B Additional Model Parameters

The saturation vs capillary-pressure relationships (saturation curve) measured for a fuel-cell CL and DM are used (shown in **Figure B.1a**) due to the expected similarities.[57] The saturation curve describing membrane hydration between its vapor- and liquid-equilibrated states derived for Nafion membranes is used and shown in **Figure B.1b**.

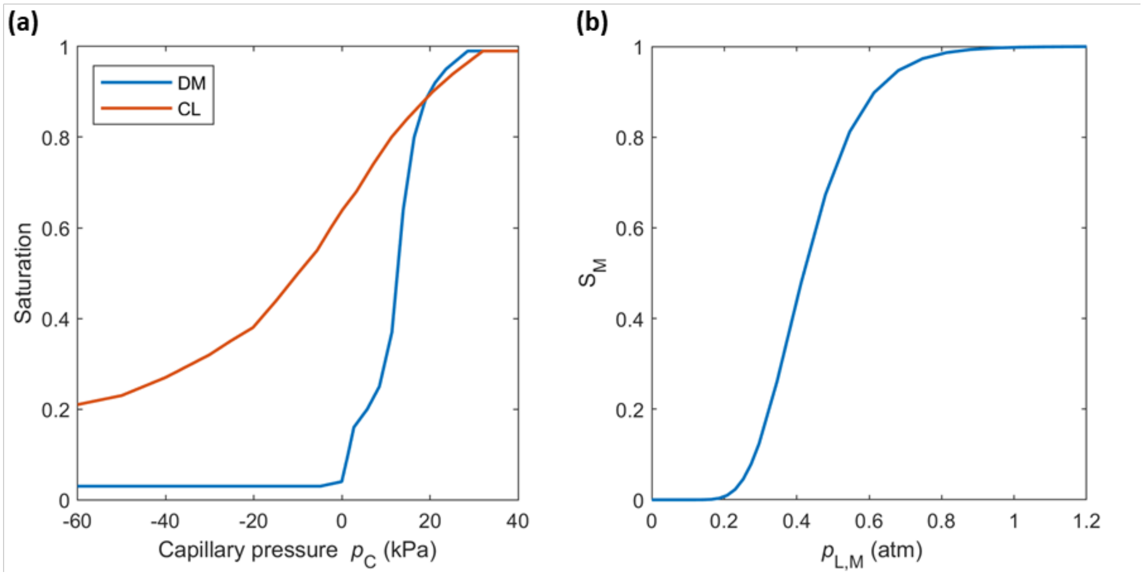

Figure B.1 (a) Saturation curve for the DM and CL.[57] (b) Saturation curve to describe membrane hydration between vapor-equilibrated and liquid-equilibrated states.[117]

The temperature-dependent transport and material properties of the membrane/ionomer are summarized in **Table B.1**. The liquid-equilibrated properties and the electro-osmotic coefficient are assumed to be independent of temperature. The temperature-dependent values of the vapor-equilibrated membrane properties were linearly interpolated/extrapolated from the values at 298 K and 350 K.

Table B.1 Membrane/ionomer properties[77, 81, 92, 118, 119]

Transport coefficient (mol^2/J·cm·s)	α_V @ 298 K	$8.0 \times 10^{-14} \exp(11.47 a_0)$
	α_V @ 350 K	$2.3 \times 10^{-13} \exp(11.47 a_0)$
	α_L	$100\alpha_\mathrm{V}^\mathrm{max}$
Water content	λ_V @ 298 K	$30.75a_0^3 - 41.19a_0^2 + 21.14a_0$
	λ_V @ 350 K	$21.90a_0^3 - 20.60a_0^2 + 8.35a_0$
	λ_L	17
Ion conductivity (S/m)	κ_V @ 298 K	$0.003 \exp(8.14 a_0)$
	κ_V @ 350 K	$0.006 \exp(6.21 a_0)$
	κ_L	$2\kappa_\mathrm{V}$
Electro-osmotic coefficient	ξ_V	0.61
	ξ_L	3
CO$_2$ diffusivity (m^2/s)	$D_{\mathrm{CO_2}}$	$2.17 \times 10^{-9} \exp(-2345\left(\frac{1}{T[\mathrm{K}]} - \frac{1}{303}\right))$
CO$_2$ solubility (mM/atm)	$H_{\mathrm{CO_2}}$	$34 \exp(-2400\left(\frac{1}{T[\mathrm{K}]} - \frac{1}{298}\right))$

Table B.2 DM and CL properties[58, 120-122]

Intrinsic porosity	ϵ_DM^o	0.526
	ϵ_CL^o	0.5
Ionomer volume fraction in pore space	$f_\mathrm{I,DM}$	0
	$f_\mathrm{I,CL}$	0.4
Electronic conductivity (S/m)	σ_DM	220
	σ_CL	100
Saturated Permeability (m^2)	ψ_DM	8.4×10^{-13}
	ψ_CL	8.0×10^{-16}

Appendix C Applied Voltage Breakdown

To quantify the inefficiencies of each physical process occurring in the electrolyzer, the applied potential is broken down into thermodynamic, kinetic, transport (and ohmic) components. Equations used to determine each of these components are listed in **Table C.1**. U^o is the standard electrode potential. Since multiple reactions occur at the cathode, the standard cathode potential depends on FE of each reaction k such that $U^o_{\text{cathode}} = \sum_k FE_k U^o_k$. $i_{\text{v},k}$ is the local current source in A/m^3, i_k in the local current density in A/m^2, $i_{o,k}$ is the exchange current density, $\alpha_{\text{a/c},k}$ is the anodic/cathodic transfer coefficient, and η_k is the overpotential for reaction k. i_{T} is the total current density of the cell, and $i_{\text{v,T}} = \sum_k i_{\text{v},k}$ is the total current source. κ^{eff} is the effective ionic conductivity of the ionomer in the CL and membrane.

Table C.1 Equations for applied voltage breakdown

Standard cell potential

$$U^o_{cell} = U^o_{\text{anode}} - U^o_{\text{cathode}} \tag{C-1}$$

Kinetic overpotential

$$\eta_{\text{kinetic}} = \sum_k \frac{RT}{i_{\text{T}}\alpha_{\text{a/c},k}F} \int_{\text{CL}} i_{\text{v},k} \ln\left(\frac{i_k}{i_{o,k}\prod_j a_{o,j}^{\gamma_j}}\right) \tag{C-2}$$

Mass transport overpotential

$$\eta_{\text{mass transport}} = \sum_k \frac{2.303RT}{i_{\text{T}}F} \int_{\text{CL}} i_{\text{v,T}}(pH_o - pH\ ) + \frac{1}{i_{\text{T}}} \int_{CL} i_{\text{v},k}\eta_k - \eta_{k,\text{kinetic}} \tag{C-3}$$

Ohmic overpotential

$$\eta_{\text{ohmic}} = \frac{1}{i_{\text{T}}} \int_{\text{CL+MEM}} \frac{i^2}{\kappa^{\text{eff}}} \tag{C-4}$$